

# The Potential of Multi-Colour Photometry for Pulsating Subdwarf B Stars<sup>1</sup>

S.K. Randall, G. Fontaine, P. Brassard, and P. Bergeron

*Département de Physique, Université de Montréal, C.P. 6128, Succ. Centre-Ville,  
Montréal, Québec, Canada H3C 3J7*

randall@astro.umontreal.ca, fontaine@astro.umontreal.ca,  
brassard@astro.umontreal.ca, bergeron@astro.umontreal.ca

## ABSTRACT

We investigate the potential of multi-colour photometry for partial mode identification in both long- and short-period variable subdwarf B stars. The technique presented is based on the fact that the frequency dependence of an oscillation's amplitude and phase bears the signature of the mode's degree index  $l$ , among other things. Unknown contributing factors can be eliminated through the evaluation of the amplitude ratios and phase differences arising from the brightness variation in different wavebands, theoretically enabling the inference of the degree index from observations in two or more bandpasses. Employing a designated model atmosphere code, we calculate the brightness variation expected across the visible disk during a pulsation cycle in terms of temperature, radius, and surface gravity perturbations to the emergent flux for representative EC 14026 and PG 1716 star models. Nonadiabatic effects are considered in detail and found to be significant from nonadiabatic pulsation calculations applied to our state-of-the-art models of subdwarf B stars. Our results indicate that the brightness variations observed in subdwarf B stars are caused primarily by changes in temperature and radius, with surface gravity perturbations playing a small role. For PG 1716 stars, temperature effects dominate in the limit of long periods with the result that the oscillatory amplitudes and phases lose their period dependence and nonadiabatic effects become unimportant. Outside this regime however, their values are strongly influenced by both factors. We find that the phase shifts between brightness variations in different wavebands are generally small, but may lie above the experimental detection threshold in certain cases. The prospect of mode discrimination seems much more promising

on the basis of the corresponding amplitude ratios. While in EC 14026 stars the amplitude ratios predicted are very similar for modes with  $l = 0, 1$  or  $2$ , they are well separated from those of modes with  $l = 3, l = 5$ , and  $l = 4$  or  $6$ , each of which form a distinct group. For the case of the PG 1716 stars it should be possible to discriminate between modes with  $l = 1, 2, 4$  or  $6$  and those of degree indices  $l = 3$  and  $l = 5$ . Identifying modes within a given group is challenging for both types of pulsator and requires multi-colour photometry of extremely high quality. Nevertheless, we demonstrate that it is feasible using the example of the largest amplitude peak detected for the fast pulsator KPD 2109+4401 by Jeffery et al. (2004).

*Subject headings:* stars: horizontal-branch — stars: interiors — stars: oscillations — subdwarfs

## 1. INTRODUCTION

Subdwarf B (sdB) stars are evolved extreme horizontal branch stars with effective temperatures in the range 20,000–42,000 K and low masses of around  $0.5 M_{\odot}$  (e.g., Saffer et al. 1994). They are believed to be composed of a helium-burning core surrounded by a hydrogen envelope too thin for them to ascend the asymptotic giant branch after core helium exhaustion (Heber 1986; Dorman 1995). Instead, they evolve off and along the horizontal branch and eventually end their lives as low-mass white dwarfs (Bergeron et al. 1994). The discovery of pulsators among subdwarf B stars (Kilkenny et al. 1997) has opened them up to asteroseismological probing, an important tool for understanding the internal structure of these interesting objects. Pulsating subdwarfs can be divided into two categories: the rapidly pulsating EC 14026 stars and the slowly oscillating long-period variable subdwarf B stars (or PG 1716 stars for short).

The first EC 14026 stars were discovered to be pulsating multi-periodically with typical periods in the range 100-200 s in 1997 (Kilkenny et al. 1997; Koen et al. 1997; Stobie et al. 1997; O’Donoghue et al. 1997). At about the same time and completely independently, Charpinet et al. (1996, 1997) predicted the existence of pressure mode ( $p$ -mode) instabilities in these stars caused by a classical kappa mechanism associated with the iron opacity peak in the subdwarfs’ envelopes. This opacity peak in turn is dependent on a local overabundance

---

<sup>1</sup>Predicted colour-amplitude ratios for a series of representative EC 14026 and PG 1716 stars are available upon request. Interested collaborators please contact S.K. Randall or G. Fontaine.

of iron, which is achieved by the competitive action of gravitational settling and radiative levitation. As the relative contributions of these two processes are determined by the surface gravity and the effective temperature of the star, all pulsating subdwarfs should lie in a designated instability strip on the  $\log g - T_{\text{eff}}$  diagram. To date, the number of known EC 14026 stars has risen to 33 (see Kilkeny 2002, Silvotti et al. 2002, Billères et al. 2002, and Fontaine et al. 2004 for a recent census), all of which fall into the theoretically predicted instability strip, clustering around  $\log g \sim 5.75$  and  $T_{\text{eff}} \sim 33,000$ . Since theoretical and observed pulsational properties are in good agreement, it is believed that a qualitative understanding of the pulsation mechanism has been reached. Beyond this, detailed quantitative interpretations of observed period spectra have been possible in a few instances (Brassard et al. 2001; Charpinet et al. 2003, 2005), allowing the identification of the modes excited through the so-called forward method. Being the ultimate goal in asteroseismology, this led to the determination of the stars’ fundamental parameters, including the mass fraction of the thin hydrogen shell which cannot be deduced otherwise. It goes without saying that independent observational tests of these mode identifications would be most welcome. In particular, the dense period spectra detected in certain EC 14026 pulsators force the controversial inclusion of modes with  $l = 3$  and 4 in the asteroseismological process, since there are not enough theoretical modes with  $l = 0, 1,$  and 2 to account for the mode density observed.

Long-period variables constitute a newer, less extensively studied class of subdwarf B pulsator. Their variability was first announced by Betsy Green at the “Asteroseismology across the H-R diagram” conference held in Porto in July 2002 (Green et al. 2003a; see also Green et al. 2003b). Slowly pulsating sdB stars are distinctly cooler than their short period counterparts and show multi-periodic, low-amplitude ( $\sim 1$  milli-magnitude) luminosity variations with typical periods between 0.8 and 1.6 hours. These are about a factor of 30 longer than those of the EC 14026 stars, and automatically imply high radial order gravity modes ( $g$ -modes). Early ideas on a possible excitation mechanism for this new class of star included tidal excitation in a close binary system (Fontaine et al. 2003a) and a mechanism involving a slow reviving of the hydrogen shell (Green et al. 2003a), but proved unfruitful. A much more promising mechanism capable of qualitatively explaining the observed periods was brought forward more recently (Fontaine et al. 2003b) and involves the same driving process that so successfully explains the instabilities in the EC 14026 stars. This is analogous to the case of the  $\beta$  Cep/slowly pulsating B stars on the main sequence (Dziembowski & Pamyatnykh 1993; Dziembowski, Moskalik, & Pamyatnykh 1993; Gautschy & Saio 1993).

In their paper describing the excitation mechanism in the slow pulsators, Fontaine et al. (2003b) built a series of representative models of subdwarf B stars along the extreme horizontal branch and computed their nonadiabatic pulsation properties in a wide range of periods for modes with  $l = 0$  to  $l = 8$ . This uncovered two distinct “islands” of instability in

the pulsational period vs  $T_{\text{eff}}$  diagram (as can be seen in their Figure 4). The first of these is clustered around  $T_{\text{eff}} \sim 31,000$  K and corresponds to the short period, low-order  $p$ -modes typical of the EC 14026 stars, where modes with degree values of  $l = 0$  and upward are driven. The second region of instability, attributed to the long period pulsators, lies at lower temperatures between 22,000 and 26,000 K and features  $g$ -modes with long periods similar to those observed in the slow oscillators. However, in the majority of models only modes with degree indices of  $l = 3$  and higher can currently be excited, which would imply that the long-period luminosity variations observed in the cooler subdwarfs correspond to modes with  $l = 3, 4,$  and  $5$ . This is in conflict with canonical wisdom, which suggests that modes with  $l \geq 3$  should generally not be observable due to cancellation effects when integrating over the visible disk of the star. While Fontaine et al. (2003b) argue that the low amplitudes of the variations observed point to modes of relatively high degree indices, they concede that the instability calculations are subject to a real blue-edge problem. In particular, we now know of long-period pulsators with effective temperatures as high as  $\sim 28,000$  K, which according to current theory should excite only modes with  $l \geq 8$ . As it does not seem feasible that these could be observed even in the best of circumstances, it is clear that we face major challenges as far as mode identification for the slow pulsators is concerned. However, there is scope for improvement on the theoretical side. Following a suggestion of Hideyuki Saio, we are currently developing more realistic subdwarf B star models that incorporate the presence of helium in the iron radiative levitation calculations, rather than adopting the pure hydrogen background assumed by Fontaine et al. (2003b). While this may well lead to a better description of the PG 1716 stars’ blue edge, we nevertheless feel it would be highly beneficial if the degree indices of the periods observed could be determined using a method completely independent of the instability calculations.

The best way of achieving this is to exploit the wavelength dependence of a mode’s pulsational amplitude, which depends on  $l$  as well as on other parameters such as the viewing angle and the intrinsic amplitude of the oscillation in question. By calculating the ratio of amplitudes in different wavebands, the latter unknown quantities can be eliminated, leaving (to a first approximation) a dependence only on  $l$  and the atmospheric parameters of the star. The theoretical colour-amplitude ratios can thus be computed for a given target and compared to pulsational amplitudes from multi-colour photometry in order to determine the modes’ degree indices. Likewise, phase shifts between oscillations in different wavebands may be exploited in certain cases. This method is by no means revolutionary and has been applied to many different types of pulsating star, such as  $\delta$  Scuti stars (Garrido, García-Lobo, & Rodríguez 1990),  $\beta$  Cepheids (Cugier, Dziembowski, & Pamyatnykh 1994), ZZ Ceti white dwarfs (Robinson et al. 1995; Fontaine et al. 1996), and  $\gamma$  Doradus stars (Breger et al. 1997), to name just a few. Attempts to understand the observed period spectrum on

the basis of multi-colour photometry have also been made for EC 14026 stars, first by Koen (1998) and more recently by Jeffery et al. (2004). The former study gives a qualitative interpretation of the periods observed for KPD 2109+4401 based on the theory of Watson (1988), while the latter asserts to have provisionally identified the modes detected for the fast oscillators KPD 2109+4401 and HS 0039+4302. In this case, the identification is based on amplitude ratios computed by Ramachandran, Jeffery, & Townsend (2004) as well as on comparisons with the pulsational properties of the evolutionary sequences published by Charpinet et al. (2002).

In the present study, we assess the potential of multi-colour photometry for pulsating sdB stars in some detail. Using a grid of specially designed model atmospheres, we are able to compute vital quantities such as the emergent specific intensities and their derivatives to high accuracies. Moreover, we carry out full nonadiabatic pulsation calculations in order to obtain eigenfunctions that are as realistic as possible, an aspect that was not studied by Ramachandran et al. (2004). In the next section, we briefly review the theory of colour-amplitude variations in pulsating stars. We then describe our computations for subdwarf B stars, and present results for a representative EC 14026 and PG 1716 model before examining the influence of the atmospheric parameters of the model in question. We end with a discussion of the practical applications of the tools developed.

## 2. BASIC THEORY

The theoretical foundations for the modelling of lightcurves of a star undergoing non-radial pulsations in the linear regime were laid by the pioneering calculations of Osaki (1971), Dziembowski (1977), Balona & Stobie (1979), and Buta & Smith (1979). Based on the Baade-Wesselink technique, their work exploited the wavelength dependence of a pulsational mode’s amplitude and phase and enabled the inference of its degree index  $l$  based on light and radial velocity observations. The equations were reformulated by Stamford & Watson (1981) and Watson (1988) for use with multi-colour photometric data alone. Their approach proved very convenient for practical purposes, and has been applied to many types of non-radially pulsating stars by a host of different authors. More recent versions, comparable in scope to the Watson method, have been presented by Cugier, Dziembowski, & Pamyatnykh (1994), Heynderickx, Waelkens, & Smeyers (1994), Balona & Evers (1999), Cugier & Daszyńska (2001), and Townsend (2002). The latest advancement was proposed by Dupret et al. (2003) and consists of including a detailed discussion of non-adiabatic effects in the optically-thin atmospheric layers. All of the above treatments model the lightcurves of non-radially pulsating stars in terms of perturbations to the photospheric pressure or surface

gravity, the effective temperature and the stellar radius. For cases where temperature effects completely dominate the brightness variations – in pulsating white dwarfs for instance – a simpler approach is possible, as was first discussed by Robinson, Kepler and Nather (1982) and later exploited for ZZ Ceti white dwarfs by Brassard, Fontaine, & Wesemael (1995, hereafter BFW95). For our application to pulsating sdB stars below, we mostly follow the presentations of Cugier and Daszyńska (2001) and Townsend (2002), but adopt a notation closer to that of BFW95.

The Lagrangian perturbations to the stellar radius  $R$ , the effective temperature  $T_{\text{eff}}$ , and surface gravity  $g_s$  caused by a single non-radial pulsation may be expressed as

$$\frac{\delta R}{R}(\theta, \phi, t) = \Re \left[ \frac{\delta r}{r^0} Y_l^m(\theta, \phi) e^{i\omega t} \right], \quad (1)$$

$$\frac{\delta T_{\text{eff}}}{T_{\text{eff}}}(\theta, \phi, t) = \Re \left[ \frac{\delta T}{T^0} Y_l^m(\theta, \phi) e^{i\omega t} \right], \quad (2)$$

$$\frac{\delta g_s}{g_s}(\theta, \phi, t) = \Re \left[ \frac{\delta g}{g^0} Y_l^m(\theta, \phi) e^{i\omega t} \right], \quad (3)$$

where  $\Re[\dots]$  denotes the real part of a complex quantity,  $\omega$  is the complex angular eigenfrequency of the mode (we define  $\omega_{nlm} \equiv \Re[\omega] = 2\pi/P_{nlm}$ , where  $P_{nlm}$  is the pulsation period of a mode of radial order  $n$ , harmonic degree  $l$  and azimuthal order  $m$ ),  $t$  is the time coordinate,  $Y_l^m(\theta, \phi)$  is the usual spherical harmonic function describing the angular dependence of the mode, and  $\frac{\delta r}{r^0}$ ,  $\frac{\delta T}{T^0}$  and  $\frac{\delta g}{g^0}$  are the radial components of the complex eigenfunctions. We define the spherical harmonics in terms of the polar angle  $\theta$  and the azimuthal angle  $\phi$  using the nomenclature of Jackson (1975) as

$$Y_l^m(\theta, \phi) = \sqrt{\frac{2l+1}{4\pi} \frac{(l-m)!}{(l+m)!}} P_l^m(\cos\theta) e^{im\phi}, \quad (4)$$

where the associated Legendre functions  $P_l^m$  can be generated by the equation

$$P_l^m(x) = \frac{(-1)^m}{2^l l!} (1-x^2)^{m/2} \frac{d^{l+m}}{dx^{l+m}} (x^2-1)^l. \quad (5)$$

With this definition, we may introduce the real quantity

$$\bar{Y}_l^m(\theta) \equiv Y_l^m(\theta, \phi) e^{-im\phi}, \quad (6)$$

which will be useful below and is described in more detail by BFW95. The radial components of the complex eigenfunctions may be written as

$$\frac{\delta r}{r^0} = \left| \frac{\delta r}{r^0} \right| e^{i\phi_r} \equiv \epsilon_r e^{i\phi_r}, \quad (7)$$

$$\frac{\delta T}{T^0} = \left| \frac{\delta T}{T^0} \right| e^{i\phi_T} \equiv \epsilon_T e^{i\phi_T}, \quad (8)$$

$$\frac{\delta g}{g^0} = \left| \frac{\delta g}{g^0} \right| e^{i\phi_g} \equiv \epsilon_g e^{i\phi_g}, \quad (9)$$

where we have introduced the dimensionless amplitudes (moduli)  $\epsilon_r$ ,  $\epsilon_T$  and  $\epsilon_g$  of the complex radial eigenfunctions, as well as their phases  $\phi_r$ ,  $\phi_T$  and  $\phi_g$  with respect to some arbitrary value, which by convention is set to  $\phi_r = 0$ . Note that the superscript “ 0 ” indicates the unperturbed value of the variable of interest in the atmospheric layers.

In the Watson approach, the brightness variation of a non-radially pulsating star is calculated by assuming a dependence of the local flux on the local instantaneous effective temperature and surface gravity, and then integrating over the observed disk taking into account the geometry of the mode and the radial distortions involved. As implemented by Townsend (2002), the first order perturbation to the emergent Eddington flux of a star undergoing a single non-radial pulsation can thus be written in terms of the radial components of the complex eigenfunctions detailed in equations 7–9 as

$$\begin{aligned} \frac{H_\nu^1}{H_\nu^0} = \Re \left[ \left( \left\{ (2+l)(1-l) \frac{\delta r}{r^0} \frac{I_{l\nu}^0}{I_{0\nu}^0} \right\} + \left\{ \frac{\delta T}{T^0} \frac{1}{I_{0\nu}^0} \frac{\partial I_{l\nu}^0}{\partial \ln T^0} \right\} + \right. \right. \\ \left. \left. + \left\{ \frac{\delta g}{g^0} \frac{1}{I_{0\nu}^0} \frac{\partial I_{l\nu}^0}{\partial \ln g^0} \right\} \right) Y_l^m(\theta_0, \phi_0) e^{i\omega t} \right]. \end{aligned} \quad (10)$$

Keeping with the notation of BFW95,  $H_\nu^0$  is the unperturbed emergent monochromatic Eddington flux,  $H_\nu^1$  is its first-order perturbation, and  $I_{l\nu}^0$  is the angle-integrated unperturbed emergent monochromatic specific intensity

$$I_{l\nu}^0 = \int_0^1 I_\nu^0(\mu) P_l(\mu) \mu d\mu, \quad (11)$$

with a weight function given by a Legendre polynomial  $P_l(\mu)$ . The angles  $(\theta_0, \phi_0)$  are the angular coordinates of the observer in the spherical coordinate system of the star. The quantity  $I_{0\nu}^0$  refers to the specific case of  $I_{l\nu}^0$  where the degree index  $l = 0$ . It is also understood that the derivative of  $I_{l\nu}^0$  with respect to the effective temperature  $T^0$  (surface gravity  $g^0$ ) is taken at constant surface gravity (effective temperature).

In order to simplify equation (10) and to enable the eventual elimination of the intrinsic amplitude of the oscillation by taking flux ratios obtained at different wavelengths, it is necessary to link the radial components of the three eigenfunctions. By convention, we express the surface gravity and temperature perturbations in terms of the radius eigenfunction. Regarding the former, Cugier and Daszyńska (2001; see also Dupret et al. 2003) have argued that one may approximate

$$\frac{\delta g}{g^0} \simeq -(2 + \sigma_{nlm}^2) \frac{\delta r}{r^0} \equiv -D_{nlm} \frac{\delta r}{r^0} \quad (12)$$

in the limit where the radial gradient of the amplitude of the pressure perturbation ( $|\delta P/P^0|$ ) is small. The real dimensionless quantity  $\sigma_{nlm}$  is given by

$$\sigma_{nlm} \equiv \omega_{nlm} \sqrt{\frac{R}{g_s}}, \quad (13)$$

where  $R$  is the stellar radius and  $g_s$  is the surface gravity. Given the definition of  $\delta r/r^0$  and  $\delta g/g^0$  in equations (7) and (9), the relationship implies that the radius and surface gravity variations occur in phase, i.e.,  $\phi_g = \phi_r$  ( $=0$ , by convention). It must be mentioned that equation (12) differs from the more standard expression employed in the Watson approach (see, e.g., equation (11) of Cugier et al. (1994)), which suggests

$$\frac{\delta g}{g^0} \simeq - \left( 4 + \sigma_{nlm}^2 - \frac{l(l+1)}{\sigma_{nlm}^2} \right) \frac{\delta r}{r^0} \equiv -C_{nlm} \frac{\delta r}{r^0}. \quad (14)$$

In the original theory outlined by Stamford and Watson (1981) and Watson (1988), the coefficient  $C_{nlm}$  is multiplied by an additional term of order unity denoted by  $P^*$  ( $\equiv \partial \log g^0 / \partial \log P^0|_{\tau=1}$ ) when used in the context of equation (14). There has been some debate as to the proper value to adopt for  $P^*$ , with some authors (e.g., Cugier et al. 1994, Balona & Evers 1999, Townsend 2002) arguing that it should be taken strictly at unity, while most others employ grids of model atmospheres to compute precise values. Regardless of whether or not the  $P^*$  quantity is included in equation (14), the expression remains considerably different from that recommended by Cugier and Daszyńska (2001; our equation (12)), particularly when considering long period modes. The latter is deemed more physical, as it is more consistent with the outer boundary conditions employed during pulsation calculations for a stellar model. We thus adopt the result of Cugier and Daszyńska (2001) after verifying that we do indeed find  $|\delta P/P^0|$  to be mostly flat in the atmospheric layers of our subdwarf B star models (as discussed below).

The radial component of the temperature eigenfunction for its part may be related to the radius perturbation by the expression

$$\frac{\delta T}{T^0} = \frac{\left| \frac{\delta T}{T^0} \right|}{\left| \frac{\delta r}{r^0} \right|} e^{i(\phi_T - \phi_r)} \frac{\delta r}{r^0} \equiv \frac{\epsilon_T}{\epsilon_r} e^{i\psi_T} \frac{\delta r}{r^0}, \quad (15)$$

where we have introduced  $\psi_T$  as the phase lag between the temperature and the radius perturbation. In the adiabatic approximation, we set  $\psi_T = \pi$ , since maximum temperature occurs at minimum radius for  $p$ -modes. In the non-adiabatic case, the phase lag can be evaluated using

$$\psi_T = \tan^{-1} \left( \frac{\Im \left[ \frac{\delta T}{T^0} \right]}{\Re \left[ \frac{\delta T}{T^0} \right]} \right) - \tan^{-1} \left( \frac{\Im \left[ \frac{\delta r}{r^0} \right]}{\Re \left[ \frac{\delta r}{r^0} \right]} \right), \quad (16)$$



where  $\Im[\dots]$  indicates the imaginary part, and  $\Re[\dots]$  denotes the real part of a complex quantity. We will apply this relation to detailed non-adiabatic calculations with the aim of modelling  $\psi_T$  as a function of depth, period, and degree index  $l$  below.

In the standard Watson approach, it is customary to introduce a second dimensionless real parameter  $R$ , which measures the departure from adiabaticity of the amplitude factor in equation (15), and can hence be defined as

$$R \equiv \frac{\epsilon_T/\epsilon_r}{\left| \left( \frac{\delta T}{T^0} \right)_{ad} \right| / \left| \left( \frac{\delta r}{r^0} \right)_{ad} \right|}. \quad (17)$$

It is obvious that, in the adiabatic limit,  $R=1$ . As for the non-adiabatic case, many authors seem to believe that physically acceptable values of  $R$  are confined to the range  $0 \leq R \leq 1$ . We beg to differ, since we see no physical reason for  $R$  not to exceed 1 and, indeed, find no justification for the constraint in the literature. As far as we can see, it arose primarily from the fact that observations of certain types of pulsating stars (such as the  $\beta$  Cephei,  $\delta$  Scuti and short-period Cepheids mentioned by Stamford & Watson 1981) indicated  $0.25 \leq R \leq 1$ . While similar values have been recovered computationally for other classes of pulsator (see, e.g., Townsend 2002 describing slowly pulsating B stars), predictions for white dwarfs have yielded  $R$  values greater than 1 in some cases (Robinson, Kepler, & Nather, 1982). This is also what our pulsation calculations indicate for the slowly pulsating subdwarf B stars, as will be described in the next section.

The quantities appearing in the denominator of equation (17) can be described by recalling a well-known expression relating the moduli of the temperature perturbation and the radius perturbation under the assumption of adiabaticity and the Cowling approximation, namely

$$\left| \left( \frac{\delta T}{T^0} \right)_{ad} \right| = -\nabla_{ad} C_{nlm} \left| \left( \frac{\delta r}{r^0} \right)_{ad} \right|, \quad (18)$$

where  $\nabla_{ad}(= 1 - \Gamma_2^{-1})$  is the usual adiabatic temperature gradient and  $C_{nlm}$  is the same coefficient as introduced in equation (14). Here the eigenfunctions  $(\delta T/T^0)_{ad}$  and  $(\delta r/r^0)_{ad}$  are real quantities, and the minus sign corresponds to a phase shift of  $\psi_T = \pi$ . Using this relation together with the definition of  $R$ , we can reformulate equation (15) to yield

$$\frac{\delta T}{T^0} = R \nabla_{ad} C_{nlm} e^{i\psi_T} \frac{\delta r}{r^0}. \quad (19)$$

Note that, in practice, the most direct way of computing the relationship between  $\delta T/T^0$  and  $\delta r/r^0$  is to use equation (15), calculating their relative phase  $\psi_T$  from equation (16),

and evaluating their amplitude ratio using

$$\frac{\epsilon_T}{\epsilon_r} = \frac{\left\{ \left( \Re \left[ \frac{\delta T}{T^0} \right] \right)^2 + \left( \Im \left[ \frac{\delta T}{T^0} \right] \right)^2 \right\}^{1/2}}{\left\{ \left( \Re \left[ \frac{\delta r}{r^0} \right] \right)^2 + \left( \Im \left[ \frac{\delta r}{r^0} \right] \right)^2 \right\}^{1/2}}. \quad (20)$$

In addition, we then explicitly evaluate the adiabacity parameter  $R$  using equation (19). This will prove useful in numerical experiments aimed at assessing the impact of non-adiabatic effects on the predicted pulsational amplitudes and phases in different filters, as  $\psi_T$  and  $R$  can be input directly and set to the adiabatic values for instance.

Returning to equation (10), the expression describing the perturbation to the emergent Eddington flux, we now seek to reformulate the intensity terms and link them to both the BFW95 and the standard Watson (1988) notation. It can be shown that the specific intensity term appearing in the temperature perturbation can be related to the monochromatic quantity  $A_{l\nu}$  defined by BFW95 by the expression

$$\frac{1}{I_{0\nu}^0} \frac{\partial I_{l\nu}^0}{\partial \ln T^0} = \frac{T^0 A_{l\nu}}{H_\nu^0}, \quad (21)$$

where, according to equation (17) of BFW95,

$$A_{l\nu} = \frac{1}{2} \int_0^1 \frac{\partial I_\nu^0}{\partial T^0} P_l(\mu) \mu d\mu. \quad (22)$$

By following the steps described in Appendix B of BFW95, we can re-write equation (21) using the notion of the limb-darkening law  $h_\nu(\mu)$  as

$$\frac{1}{I_{0\nu}^0} \frac{\partial I_{l\nu}^0}{\partial \ln T^0} = \alpha_{T\nu} b_{l\nu} + \frac{\partial b_{l\nu}}{\partial \ln T^0}, \quad (23)$$

where

$$\alpha_{T\nu} \equiv \frac{\partial \ln H_\nu^0}{\partial \ln T^0}, \quad (24)$$

and

$$b_{l\nu} \equiv \frac{\int_0^1 h_\nu(\mu) P_l(\mu) \mu d\mu}{\int_0^1 h_\nu(\mu) \mu d\mu}. \quad (25)$$

The two last quantities, the logarithmic derivative of the emergent flux with respect to the effective temperature, and the weighted monochromatic limb darkening integral, are familiar notions in the Watson model. It can be seen that, when expressing the intensity term of the temperature perturbation, one has the choice of using a single expression such as the left-hand side of equation (23) employed by BFW95 or Townsend (2002), or the splitted terms

on the right hand side of the equation favoured in the more traditional implementations of the Watson model. We choose to adopt the latter here in order to facilitate comparisons with the Watson approach.

Clearly, the specific intensity component of the gravity perturbation in equation (10) can be expressed in an equivalent way, yielding

$$\frac{1}{I_{0\nu}^0} \frac{\partial I_{l\nu}^0}{\partial \ln g^0} = \alpha_{g\nu} b_{l\nu} + \frac{\partial b_{l\nu}}{\partial \ln g^0}, \quad (26)$$

with

$$\alpha_{g\nu} \equiv \frac{\partial \ln H_\nu^0}{\partial \ln g^0}. \quad (27)$$

Finally, we use the fact that

$$I_\nu^0(\mu) = I_\nu^0(0) h_\nu(\mu) \quad (28)$$

together with the definition of  $I_{l\nu}^0$  (equation (11)) and equation (25) to reformulate the specific intensity coefficient in the radius term of equation (10) as

$$\frac{I_{l\nu}^0}{I_{0\nu}^0} = b_{l\nu}. \quad (29)$$

We can now re-write the perturbation to the relative instantaneous emergent monochromatic Eddington flux of equation (10), using equations (12), (19), (23), (26) and (29), as

$$\begin{aligned} \frac{H_\nu^1}{H_\nu^0} = \epsilon_r \bar{Y}_l^m(i) & \left[ \left\{ (2+l)(1-l)b_{l\nu} - D_{nlm} b_{l\nu} \alpha_{g\nu} - D_{nlm} \frac{\partial b_{l\nu}}{\partial \ln g^0} \right\} \right. \\ & \times \cos(m\phi_0 + \omega_{nlm}t) + \\ & \left. + \left\{ R\nabla_{ad} C_{nlm} b_{l\nu} \alpha_{T\nu} + R\nabla_{ad} C_{nlm} \frac{\partial b_{l\nu}}{\partial \ln T^0} \right\} \right. \\ & \left. \times \cos(m\phi_0 + \omega_{nlm}t + \psi_T) \right], \quad (30) \end{aligned}$$

where we used the fact that  $\theta_0 = i$ , the inclination angle, in  $\bar{Y}_l^m(i)$ , the real function giving the viewing aspect (see BFW95 for details).

In practice, the last equation will be applied to broadband, rather than monochromatic photometry, so it is necessary to express it in terms of frequency-integrated quantities. We thus introduce

$$b_{lx} \equiv \frac{\int_0^\infty W_\nu^x b_{l\nu} d\nu}{\int_0^\infty W_\nu^x d\nu}, \quad (31)$$

$$\alpha_{Tx} \equiv \frac{\int_0^\infty W_\nu^x \alpha_{T\nu} d\nu}{\int_0^\infty W_\nu^x d\nu}, \quad (32)$$

$$\alpha_{gx} \equiv \frac{\int_0^\infty W_\nu^x \alpha_{g\nu} d\nu}{\int_0^\infty W_\nu^x d\nu}, \quad (33)$$

where  $W_\nu^x$  represents the transmission function for filter  $x$ , convolved, in principle, with the response of the telescope/detector combination and the atmospheric extinction curve at a given site.

We can now regroup the various components of equation (30) into five terms analogous to those employed in the traditional Watson model. We thus introduce the following shorthand notation:

$$T_1 \equiv R\nabla_{ad} C_{nlm} b_{lx} \alpha_{Tx}, \quad (34)$$

$$T_2 \equiv R\nabla_{ad} C_{nlm} \frac{\partial b_{lx}}{\partial \ln T^0}, \quad (35)$$

$$T_3 \equiv (2+l)(1-l)b_{lx}, \quad (36)$$

$$T_4 \equiv -D_{nlm} b_{lx} \alpha_{gx}, \quad (37)$$

$$T_5 \equiv -D_{nlm} \frac{\partial b_{lx}}{\partial \ln g^0}. \quad (38)$$

We finally follow Koen (1998) and define

$$\gamma_1 \equiv T_1 + T_2, \quad (39)$$

$$\gamma_2 \equiv T_3 + T_4 + T_5, \quad (40)$$

which represent the effects on the brightness variation during a pulsation cycle due to effective temperature ( $\gamma_1$ ) and radius/gravity perturbations ( $\gamma_2$ ) respectively. Using a trigonometric identity we may then obtain our final expression for the relative flux in a photometric bandpass  $x$  arising from the excitation of a single pulsation mode

$$\frac{H_x^1}{H_x^0} = \epsilon_r \bar{Y}_l^m(i) A_{nlm}^x \cos(m\phi_0 + \omega_{nlm}t + \phi_{nlm}^x), \quad (41)$$

with the wavelength-dependent amplitude given by

$$A_{nlm}^x = (\gamma_1^2 + \gamma_2^2 + 2\gamma_1\gamma_2 \cos \psi_T)^{1/2}, \quad (42)$$

and the wavelength-dependent phase given by

$$\phi_{nlm}^x = \tan^{-1} \left( \frac{\gamma_1 \sin \psi_T}{\gamma_1 \cos \psi_T + \gamma_2} \right). \quad (43)$$

Strictly speaking, this expression is valid only for non-rotating stars where the amplitude and phase depend on the radial order  $n$  and the degree index  $l$ , but not the azimuthal order

$m$ . However, Cugier & Daszyńska (2001) have argued that it may also be applied to slowly rotating stars, loosely defined as those with a spin parameter  $S = 2\Omega/\omega_{nlm} < 0.5$  (where  $\Omega$  is the rotation frequency). In this case, the  $\omega_{nlm}t$  term in the cosine function of equation (41) is replaced by  $(\omega_{nlm} - m\Omega)t$ . The amplitude and phase also become sensitive to the azimuthal index  $m$ , but only through the period dependence of an  $m$  component in a rotationally split  $(2l+1)$  multiplet. For fast rotators with higher values of  $S$ , things become more complicated and a rigorous treatment such as the one developed by Townsend (2003) becomes necessary.

In practice, equation (41) is not used directly since it depends on the unknown factor  $\epsilon_r \bar{Y}_l^m(i)$ . Instead, we take advantage of the wavelength independence of the latter and eliminate it by calculating the amplitude ratios  $A_{nlm}^x/A_{nlm}^y$  and phase differences  $\phi_{nlm}^x - \phi_{nlm}^y$  arising from the lightcurves for two different bandpasses  $x$  and  $y$ . Mode discrimination can then proceed by exploiting the fact that the wavelength dependence of an oscillation's amplitude and phase may depend strongly on its degree index  $l$ , and that observational amplitude ratios and phase differences are readily obtainable from multi-colour photometry.

We note that if non-adiabatic effects are neglected in the calculations of the theoretical quantities, then  $\psi_T = \pi$ , the phase  $\phi_{nlm}$  calculated from equation (43) will always be zero, and no phase shifts will be predicted between different bandpasses. However, a small or negligible observed phase shift does not necessarily imply the absence of non-adiabatic effects, and one may well encounter situations where the expected phase shifts remain quite small despite important deviations of the adiabacity parameter  $R$  from its adiabatic value of  $R = 1$ . This is the case for our model of a typical EC 14026 star discussed below. On the other hand, the observed phase shifts will be expected to be negligible if effective temperature perturbations completely dominate the brightness variation and radius/surface gravity effects can safely be ignored ( $\gamma_2 = 0$  in the limiting case). In that instance, equation (43) immediately infers  $\phi_{nlm}^x = \psi_T$  irrespective of the bandpass in question. Moreover, the period dependence of the  $T_1$  and  $T_2$  terms through their common factor  $RC_{nlm}$  cancels out in the calculation of the amplitude ratios, with the result that the latter bear the signature only of the degree index  $l$  and not the period dependent radial order  $n$ . By the same logic, the amplitude ratios are no longer affected by non-adiabatic effects, a point on which we concur with Ramachandran et al. (2004). In retrospect, this alleviates the worry expressed by Robinson et al. (1982) about the legitimacy of using the adiabatic relationship between  $\delta T/T^0$  and  $\delta r/r^0$  in their discussion of colour variations in pulsating white dwarfs (see also BFW95). When considering the pulsations of white dwarfs in the linear regime, the brightness variations are completely dominated by temperature effects, which implies an absence of phase shifts between the light curves of different colours, as well as amplitude ratios insensitive to non-adiabatic effects and the period of the mode in question. The latter then depend only on the degree index  $l$ , a situation also encountered for high-order  $g$ -modes in our typical PG 1716 star

model discussed below.

### 3. MODEL ATMOSPHERES AND MONOCHROMATIC QUANTITIES

The quantities required in the theoretical framework discussed above can broadly be divided into three groups: those that can be inferred observationally, those that must be computed on the basis of full stellar models, and finally those that are derived from model atmospheres. In this section we focus on the latter group, which includes the monochromatic quantities  $\alpha_{T\nu}$ ,  $\alpha_{g\nu}$ ,  $b_{l\nu}$ ,  $b_{l\nu,T} \equiv \partial b_{l\nu} / \partial \ln T^0$ , and  $b_{l\nu,g} \equiv \partial b_{l\nu} / \partial \ln g^0$ . Since their computation involves not only the standard specific intensities, but also the corresponding derivatives with respect to effective temperature and surface gravity across the visible disk, we needed to modify our model atmosphere code for subdwarf B stars in order to carry out the task efficiently and accurately. We constructed a grid of model atmospheres defined at 9 gravity points ( $\log g = 4.8$  to  $6.4$  in steps of  $0.2$  dex) and 11 temperature points ( $T_{\text{eff}} = 20,000$  to  $40,000$  K in steps of  $2000$  K) representative of the distribution of sdB stars in the  $\log g - T_{\text{eff}}$  plane. Detailed interpolation within this grid enables the calculation of the desired quantities for any given  $\log g - T_{\text{eff}}$  combination. The model atmospheres are computed under the assumption of LTE and uniform composition specified by  $\log N(\text{He})/N(\text{H}) = -2.0$ , a typical value for sdB's. Metals were not included, since subdwarf B stars are known to be chemically peculiar, and metal abundances vary from one target to the next. While it could prove interesting to incorporate representative metal abundances and thus assess the importance of metals in this kind of calculation in the future, our H/He LTE model grid is quite sufficient for the purposes of this study.

As mentioned above, the colour-amplitude technique is usually applied to broadband photometry, but we find it instructive to first examine the behavior of the key monochromatic quantities. We begin with the unperturbed emergent Eddington flux, which is shown in the top panel of Figure 1 in the optical domain for a model with  $T_{\text{eff}} = 33,000$  K and  $\log g = 5.75$ . These are also the atmospheric parameters we adopt for our representative EC 14026 star model in the next section, where more details are provided. As is typical for the observed optical spectra of sdB stars, the Eddington flux is characterized by the presence of broad hydrogen Balmer lines and several weak and narrow helium lines. For comparison, the middle panel illustrates the predicted first-order perturbation to the emergent Eddington flux assuming a nonradial pulsation with a period of  $150$  s (a typical low-order  $p$ -mode in an EC 14026 star) and six values of the degree index from  $l = 0$  (top curve) to  $l = 5$  (bottom curve). Note that here,  $H_\nu^1$  is divided by the unknown factor  $\epsilon_r \bar{Y}_l^m(i)$ . It is evident that the pulsational amplitude rapidly decreases with increasing  $l$ , which is a direct manifestation of

the well-known geometric cancellation effects associated with an increasing number of nodal lines crisscrossing the visible disk. For values of  $l > 2$ , the decrease of the amplitude with increasing  $l$  at a given frequency is no longer monotonic, but also depends on the limb-darkening law of the model atmosphere in question in quite a complex way. The amplitude of the  $l = 4$  curve for instance is higher than that of the  $l = 3$  curve in the optical domain shown, and the latter dips below the  $l = 5$  curve above  $\sim 4000 \text{ \AA}$ . By dividing the curves by the unperturbed flux  $H_\nu^0$ , one obtains the *relative* monochromatic amplitude of the assumed mode (again to within the unknown parameter  $\epsilon_r \bar{Y}_l^m(i)$ ), as indicated in the bottom panel of the figure. It is the latter quantity that forms the basis of the colour-amplitude technique, which relies on comparing the relative amplitude at two wavelengths in order to eliminate the unknown factor.

The result of such an operation is illustrated in Figure 2, where we have divided the relative monochromatic amplitude curves for each  $l$  by the corresponding relative amplitude at an (arbitrary) frequency point in the continuum with  $\lambda = 3650 \text{ \AA}$ . In this particular example, there is little difference between curves with  $l = 0, 1$ , and  $2$ , however those with  $l = 3, 4$ , and  $5$  bear a stronger and more distinct signature of their degree index. Along with the amplitude ratios, the phase differences between the brightness variations at different wavelengths may also be used to infer the degree  $l$  of a pulsation mode. This is shown in Figure 3, where we plot the monochromatic phase difference with respect to the spectral point at  $3650 \text{ \AA}$  for the same assumed pulsation mode with a period of  $150 \text{ s}$  and  $l$  values from  $0$  to  $5$  as indicated. In our example, the phase shifts remain relatively small (less than a few degrees) over the optical domain. This implies that, in practice, mode discrimination will be difficult to achieve on the basis of phase differences alone.

The amplitude ratios and phase shifts discussed in the following sections are simply frequency-integrated counterparts to the monochromatic curves pictured in the last two figures. In this context it should be noted that the spikes associated with the central cores of the absorption lines, and in particular those related to the narrow helium lines, do not significantly contribute to the bandpass integrated quantities. We would like also to recall that the behaviour of the amplitude ratios and phase shifts with wavelength depends not only on the degree index  $l$ , but also on the period of the mode and, of course, on the atmospheric parameters of the model in question.

#### 4. NONADIABATIC EFFECTS IN REPRESENTATIVE MODELS OF PULSATING SDB STARS

We now evaluate the quantities  $R$  and  $\psi_T$  through the use of full nonadiabatic pulsation calculations. To do this, we use the same numerical tools employed earlier by Charpinet et al. (1997; see also Fontaine et al. 1998, Charpinet et al. 2001, and Fontaine et al. 2003b) to construct their second-generation stellar models. These are characterized by four free parameters, the effective temperature  $T_{\text{eff}}$ , the surface gravity  $\log g$ , the fractional mass contained in the H-rich envelope  $M(H)/M_*$ , and the total mass  $M_*$ . The models feature an opacity profile that largely depends on the nonuniform distribution of iron as a function of depth. This distribution results from the competition between gravitational settling and radiative levitation and has been shown to be responsible for the excitation of low-order  $p$ -modes in models of EC 14026 stars as well as high-order  $g$ -modes in models of PG 1716 stars (Fontaine et al. 2003b) through the  $\kappa$ -mechanism. Note that, according to the same authors, standard models of sdB stars with uniform metallicity are unable to excite pulsation modes.

In this section we will focus on a representative model of an EC 14016 star and a PG 1716 pulsator respectively. According to Figure 1 of Fontaine et al. (2004), which summarizes the location of subdwarf B stars on the H-R diagram, a typical EC 14026 star has  $\log g \simeq 5.75$  and  $T_{\text{eff}} \simeq 33,000$  K, which implies that it is significantly denser and hotter than its typical PG 1716 counterpart at  $\log g \simeq 5.40$  and  $T_{\text{eff}} \simeq 27,000$  K. We adopt these values, and list some of the models’ other characteristics, including the two defining variables  $M(H)/M_*$  and  $M_*$  in Table 1. We explicitly give the value of the total radius as well as that of the adiabatic temperature gradient averaged over the atmospheric layers (see below), as both of these quantities enter into our equations. For completeness, we also provide the value of the quantity  $P^*$  evaluated from our model atmosphere grid at the appropriate values of  $(T_{\text{eff}}, \log g)$ , despite the fact that we do not use that variable in our calculations, since we choose to relate the surface gravity and radius perturbation via the expression developed by Cugier & Daszyńska (2001).

Taking into account the range of periods observed in typical EC 14026 stars, we compute all modes with periods in the range 80–300 s and with values of  $l$  from 0 to 5 for our representative short-period pulsator model. For the case of our PG 1716 star model, we calculate modes with periods in the range 2000–6000 s and with values of  $l = 1, 2,$  and  $3$ . The first results are illustrated in Figures 4 and 5, where we show the modulus of the radial component of each mode’s nonadiabatic pressure eigenfunction as a function of depth in the outermost layers for the EC 14026 and PG 1716 model respectively. We define the “atmospheric layers of interest” as those lying between the optical depths  $\tau = 0.1$  and  $\tau$



= 10.0. It can be seen that about half of the modes considered in the EC 14026 model show small gradients across these layers as is required in the Cugier & Daszyńska (2001) expression connecting the surface gravity perturbation to the total radius perturbation. The other modes, which systematically correspond to those with shorter periods, do not strictly pass this test but, lacking a more generally applicable relation, there is little we can do to remedy this shortcoming. The situation is better for the PG 1716 model, where the vast majority of the modes considered show very small  $|\delta P/P|$  gradients across the atmospheric layers, with the exception of the few modes with the longest periods. As it turns out, we will find out below that surface gravity perturbations contribute very little to the brightness variations in pulsating sdB stars, which is lucky in the context of our present “problems”, as any inaccuracies in the surface gravity perturbations will have little impact on the final results.

Figures 6a and 6b show the behaviour of the adiabaticity parameter  $R$  in the atmospheric layers of our EC 14026 model for all modes of interest. Figures 7a and 7b illustrate similar results for the phase lag  $\psi_T$ . The figures give the distinct impression that both  $R$  and  $\psi_T$  depend primarily on the period and very little on the degree index  $l$ . This can, in fact, be confirmed quantitatively by computing an “average” atmospheric value of both quantities for each mode, and plotting them as functions of the mode’s period as shown in Figure 8. The averaging process used is a simple unweighted integration over all atmospheric layers between  $\tau = 0.1$  and  $\tau = 10.0$ . We believe that this approach is slightly more rigorous than simply taking the local values at the photosphere itself ( $\tau = 2/3$ ). Figure 8 highlights the almost perfect one-to-one relationship that exists between the value of  $\langle R \rangle$  and the period of the mode for the range of interest. A similar situation is encountered for the averaged quantity  $\langle \psi_T \rangle$ . In both cases there is very little, if any, dependence on the degree index  $l$ , allowing us to model  $\langle R \rangle$  and  $\langle \psi_T \rangle$  as functions of the period  $P$  in a simple and accurate way (we drop the subscript “ $nlm$ ” in what follows for a more concise notation). While this is not necessary when examining a specific equilibrium model for which individual values can be obtained for each mode (e.g., the small circles in Figure 8), the procedure will prove useful in our applications below, where we want to treat the pulsation period as a free continuous variable rather than a discrete eigenvalue. Values of  $R$  and  $\psi_T$  sufficiently accurate for our needs were obtained by  $\chi^2$ -fitting the data points in Figure 8 to cubic curves as illustrated. The cubic solutions are given by

$$\langle R \rangle = 0.3459 - 3.031 \times 10^{-4}P + 1.784 \times 10^{-5}P^2 - 3.040 \times 10^{-8}P^3, \quad (44)$$

and

$$\langle \psi_T \rangle = \pi + 1.1010 - 1.415 \times 10^{-2}P + 3.702 \times 10^{-5}P^2 - 2.122 \times 10^{-8}P^3, \quad (45)$$

which are formally valid in the period range 80–300 s and for values of the degree index

in the range  $l = 0-5$ . Figure 8 reaffirms the well-known fact that non-adiabatic effects are never negligible in stellar atmospheres, but it is the particular dependence of  $\langle R \rangle$  (and  $\langle \psi_T \rangle$ ) on the period that is of central interest here and that cannot be ignored in the computations. In future studies, the accuracy of the estimates for  $R$  and  $\psi_T$  could be further improved by examining the nonadiabatic pulsation equations in the presence of optically thin layers more closely, for example by following the theory of Dupret (2001) and Dupret et al. (2003).

The situation is slightly more complicated for the high-order  $g$ -modes in our representative PG 1716 model, where  $R$  and  $\psi_T$  depend on both the period  $P$  and the index  $l$  as is illustrated in Figures 9 and 10. The presence of a few trapped modes (trapped above the H-rich envelope/He core interface) renders things somewhat more challenging in terms of defining an “average” behavior for a pulsation mode. Furthermore, while  $\langle \psi_T \rangle$  depends monotonically on the period for a given  $l$  (at least in the period range of interest), this is not the case for  $\langle R \rangle$ , making it ever more tedious to acceptably fit the data points. As illustrated in Figure 11, we were finally able to find fits to  $\langle R \rangle$  and  $\langle \psi_T \rangle$  sufficiently accurate for our present needs by using the following analytic relationships

$$\langle R \rangle l^{0.13} = 0.5817 + 6.399 \times 10^{-4}(Pl^{0.38}) - 1.164 \times 10^{-7}(Pl^{0.38})^2 + 6.082 \times 10^{-12}(Pl^{0.38})^3, \quad (46)$$

and

$$\langle \psi_T \rangle = \pi - 2.30e^{(Pl^{0.38}/1800)}. \quad (47)$$

Figure 11 clearly indicates that nonadiabatic effects are important in the atmospheres of PG 1716 stars, and should not be neglected in the computations. As mentioned in the theory section, the adiabaticity parameter  $\langle R \rangle$  may become larger than 1 for the long period  $g$ -modes characteristic of these objects. However, as we will see below, temperature variations increasingly dominate the brightness variations in the limit of long periods, causing the *observable* effects of a departure from adiabaticity to disappear.

## 5. APPLICATION TO UBVRI PHOTOMETRY

As a representative application, we consider multi-colour photometry in the standard Johnson-Cousins system  $UBVRI$ . For each reference model (specified by a value of  $T_{\text{eff}}$  and a value of  $\log g$  for the model atmosphere calculations), we computed the frequency-integrated quantities  $\alpha_{Tx}$ ,  $\alpha_{gx}$ ,  $b_{lx}$ ,  $b_{lx,T} \equiv \partial b_{lx} / \partial \ln T^0$ , and  $b_{lx,g} \equiv \partial b_{lx} / \partial \ln g^0$ , where the subscript “ $x$ ” denotes one of the wavebands. In our modelling of the effective response curves  $W_\nu^x$ , we convolved the standard transmission functions of the  $UBVRI$  filters with the

extinction curve of Kitt Peak National Observatory (representative of sites with 2000–2500 m altitudes). We also assumed a grey response for the instrument/telescope combination. Our values for the frequency-integrated quantities are given in Table 2 (Table 3) for our reference EC 14026 (PG 1716) star model. For the former model, we list the values for modes with degree indices in the range  $l = 0–5$ , while for the latter they are provided for modes with  $l$  between 1 and 6 since the case  $l = 0$  is of no interest for the long-period variables (as a rule, the  $p$ -branch period spectra of sdB stars do not reach into the range of the long periods observed in PG 1716 stars).

We draw attention to the fact that in both Table 2 and Table 3  $\alpha_{gx} \ll \alpha_{Tx}$  and  $b_{lx,g} \ll b_{lx,T}$  with only very few exceptions. This means that the  $T_4$  and  $T_5$  terms will generally be very small compared to the  $T_1$  and  $T_2$  terms in the equations discussed in Section 2, implying that in sdB stars the contributions to the brightness variations due to surface gravity perturbations are small compared to the effects of effective temperature perturbations ( $T_1$  and  $T_2$ ) and radius changes ( $T_3$ ). Thus, the exact expression used to relate the surface gravity perturbation to the radius perturbation (see our discussion of the Cugier & Daszyńska 2001 method versus the more traditional one in Section 2) is of minor importance for sdB stars.

Employing the data listed in Tables 1, 2, and 3 as well as our polynomial models for  $R$  and  $\psi_T$  given by equations (44) through (47), we computed amplitudes and phases for a number of modes according to our equations (42) and (43). The period was treated as a free parameter, which enabled a detailed examination of its influence on the final results. Keeping with tradition, the amplitudes ratios and phases shifts were calculated with respect to the bluest filter, in this case the  $U$  bandpass. The results for our representative EC 14026 star model and those for our PG 1716 model are discussed separately in the following subsections.

### 5.1. Results for our representative EC 14026 star model

We first show, in Figure 12, the ratio  $|\gamma_1/\gamma_2|$  as a function of effective wavelength in the five filters considered for three representative periods spanning the range of those observed in a typical EC 14026 pulsator. All the modes illustrated are associated with degree indices  $l = 0–5$  and correspond to low-order  $p$ -modes. Excepting the modes with  $l = 1$ , for which  $T_3$  is always equal to 0 (see our equation (36)), as well as the  $l = 3$  modes in the  $I$  bandpass, for which the contributions of the effective temperature perturbations are particularly small, the figure infers that both effects (i.e., temperature and radius changes) contribute to the brightness variations in a non-negligible way. Unlike for white dwarfs, it is

thus not appropriate to assume that temperature effects completely dominate in EC 14026 stars. While we already mentioned that the  $T_4$  and  $T_5$  terms usually remain quite small, it is the  $T_3$  term, whose numerical value dominates  $\gamma_2$ , that becomes appreciable compared to  $\gamma_1$  ( $= T_1 + T_2$ ).

In order to assess the importance of non-adiabatic effects, we repeated the calculation of  $|\gamma_1/\gamma_2|$ , this time imposing the adiabatic values  $R = 1$  and  $\psi_T = \pi$  for all modes considered. The results are represented by the dotted lines in Figure 12. Keeping in mind the logarithmic scale of the ordinate axis, it is obvious that non-adiabatic effects are significant in the composition of brightness variations in EC 14026 pulsators.

Figure 13 shows the expected phase shifts for the same set of modes. It can be seen that, in the optical domain, the phase shifts depend on the period quite sensitively, while remaining relatively small and reaching a maximum of a few degrees at the most in the period range of interest. In the adiabatic approximation we expect no phase shifts at all. This means that, in practice, it will be very difficult to exploit the (weak)  $l$  dependence of such phase shifts. The situation seems more promising for the amplitude ratios illustrated in Figure 14. However, while the modes with  $l = 3, 4,$  and  $5$  bear distinct signatures of their degree index, the capacity to discriminate between modes with  $l = 0, 1,$  and  $2$  on the basis of optical photometry appears much more limited. Observational amplitude measurements for such modes will have to be unusually precise if they are to be used as mode discriminators in EC 14026 stars. We would like to point out that non-adiabatic effects on the amplitude ratios are generally non-negligible, as can be deduced by comparing the continuous lines (non-adiabatic results) to the dotted lines (adiabatic values) in Figure 14. It may also be worth mentioning that the results depicted in the middle panels of Figures 13 and 14 (the case with  $P = 150$  s) are consistent with the monochromatic results illustrated in Figures 2 and 3, as is to be expected.

In Figures 15a and 15b (separated for visualization purposes), we plot the expected amplitude ratios for modes with  $P = 100$  s (dotted lines),  $150$  s (dashed lines), and  $200$  s (long-dashed lines), with the aim of emphasizing their strong period dependence. In order to compare the results to corresponding period-independent values, we also include amplitude ratios (solid lines) obtained by postulating that effective temperature perturbations completely dominate the brightness variations (i.e. by setting  $\gamma_2 = 0$  in the calculations). As suggested above, it becomes evident that this not a good working assumption for the EC 14026 stars.

Finally, in Figure 16, we show the results of a numerical experiment in which we explicitly adopt  $T_3 = 0$  in order to assess the relative impact of the  $T_4$  and  $T_5$  terms on the amplitude ratios. The resulting period-dependent ratios are indicated by the dotted lines

and contrast with the continuous lines corresponding to the period-independent limiting case in which  $\gamma_2 = 0$ . While we previously argued that the contributions of the  $T_4$  and  $T_5$  terms are generally be quite small in pulsating sdB stars, the figure reveals that non-negligible effects remain for certain cases, especially in the  $B$  band. We thus recommend that these terms be kept by in the calculations, particularly since they are readily computable.

## 5.2. Results for our representative PG 1716 star model

The computations for our reference PG 1716 model uncover two distinct regimes as far as the relative importance of the temperature perturbation is concerned. At the lower end of the period range of interest, contributions from both the  $\gamma_1$  and  $\gamma_2$  terms are significant, whereas the brightness variations are dominated by temperature changes for the longer periods involved. This can be seen from Figures 17a and 17b, where we show the ratio  $|\gamma_1/\gamma_2|$  as a function of effective wavelength in a format similar to that of Figure 12. In these and the following figures, we illustrate our results for six different periods between  $P=2400$  s and  $P=6000$  s. Comparing Figures 17a and 17b clearly reveals that the ratio  $|\gamma_1/\gamma_2|$  monotonically increases with period for all filters and degree indices  $l$ . This is a direct consequence of the the  $\gamma_1$  term increasing in absolute value with period via the period-dependent coefficient  $C_{nlm}$  for the long periods considered, while  $T_3$  remains constant for a given filter and degree index. We recall that modes with  $l=1$  represent a special case, since  $T_3=0$  in that instance.

This transition from one regime to the other strongly influences the phase shifts and amplitude ratios calculated. The former are depicted in Figures 18a and 18b for the same set of modes as considered above. For the shorter periods we predict significant phases shifts, which reach more than 10 degrees for the 2400 s period. Unlike the much smaller phase shifts expected for the EC 14026 stars, this is well within achievable measurement accuracy. At the same time, we find the magnitude of the expected phase shifts to drop very rapidly with increasing period in PG 1716 stars (note, in particular, the change of the ordinate scale between Fig. 18a and Fig. 18b), to the point where they would not be detected with any confidence for the longer period modes.

The expected amplitude ratios are shown in Figures 19a and 19b. Once again, the transition from the period-dependent regime, where  $\gamma_1$  and  $\gamma_2$  are of similar importance, to the period-independent case dominated by effective temperature perturbations is striking. The plots also emphasize the diminishing importance of nonadiabatic effects with increasing period, as can be seen from the convergence of the dotted (adiabatic) and continuous (non-adiabatic) lines. Thus, in our PG 1716 model nonadiabatic effects range from extremely

significant for  $P = 2400$  s to practically negligible for  $P = 6000$  s.

In Figures 20a and 20b (separated for visualization purposes), we compare the expected amplitude ratios for modes with  $P = 3000$  s (dotted lines), 4000 s (dashed lines), 5000 s (long-dashed lines), 6000 s (dot-dashed lines), 7000 s (dot-long-dashed lines), and 8000 s (dashed-long-dashed lines), again with the aim of highlighting the period dependence of the results. The convergence of the ratios to the period-independent values (solid lines) in the limiting case of long periods is recovered nicely. As before, the period-independent ratios are obtained by assuming that effective temperature perturbations completely dominate the brightness variations (i.e., by setting  $\gamma_2 = 0$  in the calculations).

Analogously to the case presented in Figure 16 for our EC 14026 model, we carry out supplementary calculations where we explicitly set  $T_3 = 0$  in order to assess the relative impact of the  $T_4$  and  $T_5$  terms on the amplitude ratios. The results of this numerical experiment are shown in Figure 21. As in Figure 16, the resulting period-dependent ratios are indicated by dotted lines and are compared to the solid lines representing the period-independent limiting case for which  $\gamma_2 = 0$ . In contrast to the previous plot, the contributions of the  $T_4$  and  $T_5$  terms are essentially negligible in PG 1716 stars, apart for in the very shortest periods. For the three longest periods (not illustrated) the two curves are not distinguishable.

Having discussed the signature of the period and the degree index, as well as that of the different terms contributing to the brightness variations on bandpass-integrated wavelength, we now focus specifically on results expected from the  $U - I$  filter combination (which corresponds to the longest wavelength base in the system used here). Figure 22 shows the  $I$  to  $U$  amplitude ratio as a function of the degree index  $l$  on the basis of calculations extending to  $l = 8$ . From bottom to top, the various curves correspond to periods with  $P = 2400, 3000, 4000, 5000, 6000, 7000$  and  $8000$  s respectively. The top curve represents an infinite period, to which the finite period curves converge in the limiting case. While evident from previous figures, the peculiar behaviour of the  $l=3$  and  $5$  modes is particularly striking here. In practice, these are the modes most likely to be identified from multi-colour photometry, since the amplitude ratios of the remaining modes may not differ enough to the extent where they can be resolved observationally.

Finally, Figure 23 and 24 respectively show the  $I/U$  amplitude ratio and the  $I - U$  phase shift expected for our PG 1716 model as a function of period for modes with  $l=1$  (black), 2 (grey), 3 (blue), 4 (cyan), 5 (green) and 6 (red). Note that here, the periods illustrated were not considered as free parameters, but are the solution of the eigenvalue problem. Once again, the convergence of values to the period-independent value in the limiting case of long periods is evident. Interestingly, in Figure 23 the results for the very shortest periods break with the systematic decrease in amplitude ratio with period, and slightly increase instead.

These same periods are associated with particularly large (potentially detectable) phase shifts in Figure 24, however it should be noted that these are shorter than the periods so far observed in PG 1716 stars and of primarily theoretical interest.

### 5.3. Results for other models: Dependence on $T_{\text{eff}}$ and $\log g$

In this section, we go beyond the two representative subdwarf B star models explored above and discuss the dependence of amplitude ratios and phase differences on the atmospheric parameters  $\log g$  and  $T_{\text{eff}}$ . To this end, we constructed a sequence of subdwarf B star models parallel to the zero-age extreme horizontal branch, the vital parameters of which are detailed in Table 4. Note that the surface gravity increases with effective temperature, while the thickness of the hydrogen-rich outer layer decreases. The division between the PG 1716 and EC 14026 regime is based on spectroscopically determined values of  $\log g$  and  $T_{\text{eff}}$  for the two types of pulsator, such as those illustrated in Figure 1 of Fontaine et al. (2004). In addition to the fundamental parameters, Table 4 also gives the approximate period range in which modes are believed to be excited for each model. For the EC 14026 stars, these correspond to modes that are found to be unstable from our non-adiabatic pulsation calculations, since the latter have been shown to predict the observed period ranges very accurately. Note that we have uniformly decreased the iron abundance in our models by a factor of 3 compared to the original “second-generation” models, as suggested by Fontaine et al. (2003b). In the case of the PG 1716 stars the situation is more complicated due to the discrepancies that still exist between modelled and observed instability regions (see our discussion in the Introduction). We can however constrain the unstable period ranges for the PG 1716 models in our sequence on the basis of the frequencies extracted from long-period variable subdwarfs observed. To date, a quantitative analysis of the period spectrum has been possible for three targets spanning the range of PG 1716 stars in effective temperature: PG 1627+017 at  $T_{\text{eff}} \sim 23,000$  K (Randall et al. 2004a), PG 1338+481 at  $T_{\text{eff}} \sim 26,000$  K (Randall et al. 2004b) and PG 0101+039 at  $T_{\text{eff}} \sim 28,000$  K (Randall et al. 2005). The study of these objects revealed that the width and mode density of the excited period range, as well as the numerical values of the periods themselves, decrease systematically with increasing temperature, enabling us to infer approximate instability bands for all models in our sequence by interpolation of the observed values. It is these estimated period ranges, rather than precisely modelled quantities, that are given in Table 4.

For each model in the sequence, we computed the necessary model atmosphere parameters in the same bandpasses as used for the representative models for modes with  $l = 0 - 6$  according to their specific  $\log g - T_{\text{eff}}$  combination. The stellar radius was likewise deter-

mined for every model on the basis of its mass and surface gravity, and its characteristic periods were evaluated from pulsation theory in the range of interest. On the other hand, the remaining three quantities derived from the full stellar models and non-adiabatic pulsation calculations were approximated to the values determined for the appropriate representative model. Thus the values of  $\langle \nabla_{ad} \rangle$  were taken from Table 1, while  $\langle R \rangle$  and  $\langle \psi_T \rangle$  were computed using equations (44) and (45) or expressions (46) and (47) for the EC 14026 and PG 1716 models respectively. The resulting accuracy of  $\langle R \rangle$  and  $\langle \psi_T \rangle$  is deemed sufficient for the illustrative purposes sought here, however it is understood that for quantitative analyses of observed multi-colour photometry the fitting process outlined in section 4 will have to be repeated for the designated object.

Figures 25 and 26 respectively show the phase shifts and amplitude ratios predicted for our sequence of subdwarf B star models from the  $I - U$  bandpass combination. They are illustrated for modes with  $l = 0$  (yellow, EC 14026 stars only),  $l = 1$  (black),  $l = 2$  (grey),  $l = 3$  (blue),  $l = 4$  (cyan),  $l = 5$  (green) and  $l = 6$  (red). Points of different colour are shifted slightly in effective temperature for a given model in order to facilitate viewing and the PG 1716 and EC 14026 domains are separated by the vertical dotted line. From Figure 25 we find that the phase shifts predicted are small (less than 5 degrees) for the majority of modes in both EC 14026 and PG 1716 stars, and would most likely lie below the detection threshold of multi-colour observations. Larger phase shifts of up to  $\sim 10$  degrees are expected for the very shortest periods in the hotter PG 1716 variables, as well as for the  $l = 3$  modes at the higher end of the period range excited in the hotter EC 14026 stars. While it seems plausible that the latter could be detected observationally, the potential for mode discrimination in subdwarf B stars clearly lies with the amplitude ratios depicted in Figure 26. In the case of the PG 1716 stars, the values for modes with  $l = 1, 2, 4$  or  $6$  are very similar, but can easily be distinguished from those of  $l = 3$  or  $l = 5$  modes. Even though the three regimes slowly approach each other with increasing temperature, they remain well separated irrespective of the model in question. In the case of the EC 14026 stars, we identify four distinct groups of modes with  $l = 0, 1$  or  $2$ ,  $l = 3$ ,  $l = 5$  and  $l = 4$  or  $6$ . Again, the influence of the model parameters is relatively small compared to the separation between the domains and becomes vital only when attempting to discriminate between the modes of a given group.

It should be kept in mind that the results depicted in Figures 25 and 26 depend not only on the atmospheric parameters of the models in question, but also on the period range excited in each case. As such, they represent the phase shifts and amplitude ratios predicted in real subdwarf B stars and give a good indication of what would be expected from multi-colour photometry. However, in terms of a purely theoretical exploration we find it instructive to examine the impact of both the surface gravity and the effective temperature on the amplitude ratios individually. To this end, we repeated the computation process detailed



above for both EC 14026 and PG 1716 stars, keeping the effective temperature (surface gravity) constant at the representative value from Table 1, and varying the surface gravity (effective temperature) within the ranges found in the sequences of Table 4. We imposed a representative period of  $P = 150$  s for the EC 14026 star domain and  $P = 4500$  s for the PG 1716 star regime. The variation of the amplitude ratio with effective temperature is illustrated in Figures 27a and 27b for short- and long-period variable subdwarf B stars respectively (see the figure captions for more detail). For both types of oscillator, the curves are reminiscent of the amplitude ratios found for our sequence of subdwarf B stars presented in Figure 26, and change gradually and monotonically with temperature. The situation is more interesting for the variation with surface gravity, depicted in Figure 28a (28b) for EC 14026 (PG 1716) models. In the case of the fast oscillators, the amplitude ratios for most of the modes move in the opposite direction compared to Figure 26, and the closely spaced  $l = 0, 1, 2$  graphs seem to diverge from the (constant)  $l = 1$  value as the surface gravity increases. For the PG 1716 models, curves representing modes of different degree indices overlap in several instances, giving rise to a behaviour similar to that encountered as a function of period (see Figure 23).

## 6. FEASIBILITY OF APPLICATION TO MULTI-COLOUR DATA

In this section we demonstrate the potential of the method developed by applying it to published multi-colour photometry. To date, the only sets of multi-colour observations that exist for pulsating subdwarf B stars are those of Koen (1998), Falter et al. (2003), Jeffery et al. (2004), and Oreiro et al. (2005). Among these, the Jeffery et al. (2004) data for the fast pulsator KPD 2109+4401 yielded the most accurate amplitude estimates. Based on three nights of Sloan filter u’g’r’ photometry with ULTRACAM (Dhillon et al., in preparation) mounted on the 4.2-m William Herschel Telescope, the authors were able to extract seven periodicities in the 180–200 s range. For the purposes of our brief feasibility study, we attempt to determine the degree index of the highest amplitude mode at 182.4 s only.

The first step towards finding the theoretical amplitudes in different wavebands is the calculation of the monochromatic model atmosphere quantities  $\alpha_{T\nu}$ ,  $\alpha_{g\nu}$ ,  $b_{l\nu}$ ,  $b_{l\nu,T}$  and  $b_{l\nu,g}$  described in Section 3. Since these depend quite sensitively on the atmospheric parameters of the target, they need to be computed for KPD 2109+4401 specifically. We adopt  $T_{\text{eff}}=31,380$  K and  $\log g=5.65$  as derived from our model atmosphere fit to the hydrogen Balmer and helium lines present in the time-averaged high-resolution MMT spectrum obtained by Betsy Green (private communication). These values are part of an ongoing program designed to provide homogeneous estimates of the atmospheric parameters of a large sample of subdwarf

B stars, and we refer the interested reader to the forthcoming Paper by Green, Fontaine, & Chayer (in preparation) for more information. The monochromatic quantities are then integrated over the effective u’g’r’ wavebands, computed by convolving the Sloan bandpasses with the quantum efficiency curves of the ULTRACAM CCD chips (Vik Dhillon, private communication) and the atmospheric transparency curve of a representative observing site at 2000–3000 m altitude (in this case Kitt Peak National Observatory). Next, we derive the adiabacity parameters  $R$  and  $\Psi_T$  (Section 4) for a period of 182.4 s from the non-adiabatic eigenfunctions of an envelope model characterised by the atmospheric parameters given above as well as representative values of  $M_*=0.48 M_\odot$  and  $\log q(H)=-4.0$ . We finally calculate the pulsational amplitudes expected from the u’, g’, and r’ photometry for degree indices from  $l=0$  to  $l=5$  using the equations given in Section 2.

The predicted multi-colour amplitudes are fit to those observed using a  $\chi^2$  minimisation routine following Fontaine et al. (1986). Compared to the standard normalisation of all amplitudes to one particular waveband this is a more objective way of determining the quality of a match, since the data from all bandpasses are weighted evenly. For every degree index  $l$  the theoretical amplitudes  $a_{theo}$  in each of the three bandpasses  $i$  are multiplied by a scale factor  $f_l$ , chosen in such a way as to minimise

$$\chi^2 = \sum_{i=1}^3 \left( \frac{f_l a_{theo}^i - a_{obs}^i}{\sigma^i} \right)^2, \quad (48)$$

where  $a_{obs}^i$  is the amplitude observed in a given waveband and  $\sigma^i$  is the error on the measurement. The results of this operation for the 182.4-s mode of KPD 2109+4401 detected by Jeffery et al. (2004) are illustrated in Figure 29, and the corresponding  $\chi^2$  and quality-of-fit (Q) values are listed in Table 5. It is immediately obvious that the data are matched well by the predictions for an  $l=0$  mode, the theoretical values falling within the (very small) error bars in all bandpasses. The next best fit is that of the  $l=1$  mode, however the associated  $\chi^2$  residuals are a factor of 30 larger than those for  $l=0$ . In fact, if we adopt the canonical notion that a fit cannot be considered convincing unless the quality-of-fit  $Q > 0.001$  (see, e.g., Press et al. 1986), the theoretical  $l=0$  mode is the *only* one that can reproduce the observed amplitudes in a satisfactory manner. While this implies an unambiguous identification of the mode’s degree index, it should be kept in mind that the estimated  $\chi^2$  and  $Q$  values are sensitive to the formal uncertainties on the observed amplitudes, which may well have been underestimated. Assuming, in an extreme case scenario, that the true errors are twice as large as those calculated by Jeffery et al. (2004), both  $l=0$  and  $l=1$  would provide acceptable fits. Nevertheless, the match for  $l=0$  remains far superior, and we believe that our identification of the degree index is sound.

We would like to point out that this is the first partial mode identification in a subdwarf

B star on the basis of its amplitude-wavelength dependence alone. While the net result – the mode has a degree index of  $l=0$  – is the same as that of Jeffery et al. (2004), we were not forced to invoke additional constraints to distinguish modes with  $l=0, 1$ , and  $2$ . The greater accuracy achieved is undoubtedly due to the fact that we were able to compute a detailed model atmosphere characteristic of KPD 2109+4401 specifically, and could incorporate non-adiabatic effects from realistic envelope models.

## 7. CONCLUSION

We have modelled the brightness variations expected across the visible disk during a pulsation cycle for both short- and long-period variable subdwarf B stars taking into account the effects of temperature, radius, and surface gravity perturbations. The quantities related to the emergent intensity and its derivatives with respect to effective temperature and surface gravity were computed with the aid of a full model atmosphere code specifically modified for this purpose. Employing full model atmospheres has led to a degree of self-consistency not often achieved in this kind of calculation for other types of pulsating stars. For instance, in the case of pulsators near the main sequence most researchers use the Kurucz (1993) model atmospheres (or their equivalent) to compute  $\alpha_{Tx}$  and  $\alpha_{gx}$ . However, since these data do not treat limb darkening, the same authors are forced to turn elsewhere, in particular to the popular tables of Wade & Rucinski (1985), for limb darkening coefficients that allow them to approximately estimate the quantities  $b_{lx}$ ,  $b_{lx,T}$ , and  $b_{lx,g}$ . Notwithstanding the fact that sdB stars are not main sequence stars, our approach alleviates the uncertainties associated with this mixed procedure.

In contrast to previous studies concerning the potential of multi-colour photometry for mode identification in sdB stars, we were able to model non-adiabatic effects in some detail. Applying full non-adiabatic pulsation calculations to representative EC 14026 and PG 1716 star models showed that these are by no means negligible. In EC 14026 stars, the two parameters measuring the departure from adiabaticity of the eigenfunctions in the atmospheric layers of interest ( $\langle R \rangle$  and  $\langle \psi_T \rangle$ ) vary systematically with period, but are independent of the degree index  $l$ . This is fortunate as it implies that  $\langle R \rangle$  and  $\langle \psi_T \rangle$  can be accurately computed for observed periodicities without assuming any prior knowledge of  $l$ . We should mention here that, while we use the fits to  $\langle R \rangle$  and  $\langle \psi_T \rangle$  obtained from our representative model throughout this explorative study, the latter are sensitive to the atmospheric parameters of the model in question. As such, they must be computed individually according to the specifications of each target if a quantitative interpretation of the observational data is to be achieved. For the PG 1716 stars, the

situation is more complicated as the departure from adiabaticity depends on  $l$  as well as on the period. The values of  $\langle R \rangle$  and  $\langle \psi_T \rangle$  attributed to oscillations observed will therefore constitute only rough estimates, introducing inaccuracies into the amplitude ratios and phase shifts computed. Fortunately, measurements of the longer periods excited in these stars are insensitive to non-adiabatic effects since they are dominated by temperature perturbations and  $\langle R \rangle, \langle \psi_T \rangle$  cancel out in the amplitude ratios and phase shifts. It is of interest to note that our computations return  $R > 1$  for the majority of modes believed to be excited in long-period variable subdwarf B stars. Although this is in conflict with the prevailing sentiment that  $R$  must lie in the range  $0 < R < 1$ , we find no physical justification for this and believe our results to be accurate.

According to our computations, the brightness variations observed in subdwarf B stars are caused primarily by temperature and radius perturbations, the contribution of surface gravity changes being small in EC 14026 stars and negligible in PG 1716 stars. For the latter, temperature effects alone dominate the flux changes in the limit of long periods. In this regime, non-adiabatic effects lose their influence on the amplitude ratios and phase shifts, and the period of the mode is no longer an issue. The adiabatic approximation is thus valid in this particular case, which immediately implies that oscillations should occur in phase at all wavelengths. Note however that conversely a lack of observed phase shifts does not automatically justify use of the adiabatic approximation. Even outside the temperature dominated regime, phase shifts are generally predicted to be small, although they may reach up to  $\sim 10$  degrees for the shortest periods in PG 1716 stars and certain  $l=3$  modes in EC 14026 stars. Whereas this may be large enough for an observational detection, it is clear that mode discrimination will occur primarily on the basis of the amplitude ratios. We note that for main sequence  $g$ -mode oscillators (e.g., Aerts et al. 2004 or De Cat et al. 2005) as well as for white dwarfs (e.g., Robinson et al. 1982) the measured phase shifts are negligible.

In the case of the EC 14026 stars, it should be relatively straightforward to distinguish modes with  $l = 0, 1$ , or  $2$  from those with  $l = 3, l = 4$  or  $6$  and  $l = 5$ . This could well prove invaluable as a consistency check for the “forward approach” in asteroseismology, which has been used to claim mode identification in a number of short period variables through the inference of modes with  $l = 0, 1, 2$  and  $3/4$  (e.g., Charpinet et al. 2005). It is interesting to note, in this connection, that the visibility of the  $l = 3$  modes in the optical domain is less than that of the  $l = 4$  modes (see Fig. 1), very much like the situation in main sequence  $p$ -mode pulsators (e.g., Heyndericks et al. 1994), and this should be taken into account in future asteroseismological exercises of the sort. Discrimination between modes with  $l = 0, 1$ , or  $2$  is much more challenging and requires multi-colour photometry of unprecedented quality as well as accurate spectroscopic estimates of the atmospheric parameters for the target observed. Nevertheless, we have demonstrated that it is feasible using the highest

amplitude mode detected for KPD 2109+4401 (Jeffery et al. 2004) as an example. It is not yet clear whether similar results can be achieved on the basis of other published datasets, or even for the lower-amplitude modes detected in KPD 2109+4401. This can only be answered through detailed quantitative analyses, which we plan to carry out in the near future. It will be particularly interesting to see whether we can confirm the tentative mode identifications reported by Jeffery et al. (2004) for the remaining modes detected for KPD 2109+4401 and HS 0039+4302. Regardless of the outcome of this project, we feel confident that colour-amplitude ratios and phase shifts could be measured to sufficient accuracy from future observations provided that the targets are bright enough and light curves with well resolved frequency peaks in the Fourier domain are obtained. Several consecutive nights on a 4 m-class telescope, or even a single night on an 8 m telescope for a well-chosen “simple” pulsator such as PG 1219+534 (see Charpinet et al. 2005) would likely be adequate. Alternatively, simultaneous ground- and space-based observations would be useful insofar as the frequency baseline could be extended to the UV, where the signature of the degree index on the pulsational amplitude is greater than in the visible domain. Given the observing time on the appropriate instrument, it would be interesting to monitor a target for which an asteroseismological analysis has already been completed, and compare the degree indices inferred from the two independent methods.

For the PG 1716 stars, discrimination on the basis of colour-amplitude ratios seems feasible between modes with degree indices  $l = 1, 2, 4, 6$  and those with  $l = 3$  and  $l = 5$ . To date, the only substantial set of multi-colour photometry for a long-period variable subdwarf consists of the  $\sim 250$  hours of simultaneous (Johnson-Cousins) U/R data obtained for PG 1338+481. While detailed results will be presented elsewhere, a preliminary analysis of the photometry indicates amplitude ratios consistent with those predicted for  $l = 1, 2, 4$  or  $6$  rather than  $l = 3$  or  $l = 5$ .<sup>2</sup> Compared to the study of EC 14026 stars, that of the PG 1716 stars is still in its infancy, which is partly due to deficiencies in the models, and partly a result of the considerable observational challenges presented by the low amplitudes and long periods of the pulsations. Unambiguous mode identification in these objects will likely be possible only by using a combination of the “forward approach” employed for the EC 14026 stars, and inference of the degree index from multi-colour photometry, which we have developed the tools for. In the immediate future we hope that restricting, if not identifying, the degree index will clarify the current discrepancies between predicted and observed instabilities and pave the way for a more mature understanding of these exciting objects.

---

<sup>2</sup>We point out in this context that main sequence  $g$ -mode pulsators with good empirical mode identification all have  $l = 1$ .

This work was supported in part by the Natural Sciences and Engineering Research Council of Canada and by the Fonds de recherche sur la nature et les technologies (Québec). G.F. also acknowledges the contribution of the Canada Research Chair Program.

Table 1. Basic Properties of our Representative sdB Models

	EC 14026	PG 1716
$T_{\text{eff}}$ (K)	33,000	27,000
$\log g$	5.75	5.40
$M_*/M_{\odot}$	0.48	0.48
$\log M(H)/M_*$	−4.0	−2.5
$R_*/R_{\odot}$	0.1528	0.2286
$\langle \nabla_{ad} \rangle$	0.345	0.350
$(P^*)$	(1.86)	(1.90)

Table 2. Model atmosphere parameters for our reference EC14026 star model

Filter	$\alpha_{Tx}$	$\alpha_{gx}$	$b_{lx}$	$b_{lx,T}$	$b_{lx,g}$
<i>l=0</i>					
U	2.92408e+00	-8.79918e-03	1.00000e+00	0.00000e+00	0.00000e+00
B	2.39047e+00	-1.03963e-02	1.00000e+00	0.00000e+00	0.00000e+00
V	2.22439e+00	-3.58973e-03	1.00000e+00	0.00000e+00	0.00000e+00
R	2.20732e+00	-4.44731e-03	1.00000e+00	0.00000e+00	0.00000e+00
I	2.16038e+00	-4.66709e-03	1.00000e+00	0.00000e+00	0.00000e+00
<i>l=1</i>					
U	2.92408e+00	-8.79918e-03	6.82603e-01	-8.27838e-02	1.50712e-04
B	2.39047e+00	-1.03963e-02	6.80962e-01	-7.07727e-02	-4.30909e-04
V	2.22439e+00	-3.58973e-03	6.79500e-01	-6.48752e-02	4.72654e-05
R	2.20732e+00	-4.44731e-03	6.77752e-01	-5.72272e-02	3.63862e-05
I	2.16038e+00	-4.66709e-03	6.75976e-01	-4.98751e-02	1.40290e-04
<i>l=2</i>					
U	2.92408e+00	-8.79918e-03	2.77831e-01	-1.45151e-01	2.72343e-04
B	2.39047e+00	-1.03963e-02	2.74875e-01	-1.23325e-01	-7.48759e-04
V	2.22439e+00	-3.58973e-03	2.72346e-01	-1.12924e-01	7.83689e-05
R	2.20732e+00	-4.44731e-03	2.69307e-01	-9.93220e-02	5.76610e-05
I	2.16038e+00	-4.66709e-03	2.66224e-01	-8.62079e-02	2.41525e-04
<i>l=3</i>					
U	2.92408e+00	-8.79918e-03	2.21585e-02	-1.13544e-01	2.28955e-04
B	2.39047e+00	-1.03963e-02	1.96901e-02	-9.49294e-02	-5.71154e-04
V	2.22439e+00	-3.58973e-03	1.77843e-02	-8.66973e-02	5.26364e-05
R	2.20732e+00	-4.44731e-03	1.54585e-02	-7.57038e-02	3.31297e-05
I	2.16038e+00	-4.66709e-03	1.31074e-02	-6.50246e-02	1.79893e-04
<i>l=4</i>					
U	2.92408e+00	-8.79918e-03	-3.37428e-02	-2.92580e-02	8.03034e-05
B	2.39047e+00	-1.03963e-02	-3.45850e-02	-2.23291e-02	-1.25024e-04
V	2.22439e+00	-3.58973e-03	-3.49776e-02	-2.01295e-02	2.41962e-06
R	2.20732e+00	-4.44731e-03	-3.55043e-02	-1.68782e-02	-7.22134e-06
I	2.16038e+00	-4.66709e-03	-3.60262e-02	-1.36059e-02	3.36702e-05
<i>l=5</i>					



Table 2—Continued

Filter	$\alpha_{Tx}$	$\alpha_{gx}$	$b_{lx}$	$b_{lx,T}$	$b_{lx,g}$
U	2.92408e+00	-8.79918e-03	2.94649e-03	1.84351e-02	-1.87196e-05
B	2.39047e+00	-1.03963e-02	3.17349e-03	1.73638e-02	1.16289e-04
V	2.22439e+00	-3.58973e-03	3.57060e-03	1.60135e-02	-1.73842e-05
R	2.20732e+00	-4.44731e-03	4.01634e-03	1.44965e-02	-1.84547e-05
I	2.16038e+00	-4.66709e-03	4.47573e-03	1.31376e-02	-4.11307e-05

Table 3. Model atmosphere parameters for our reference PG1716 star model

Filter	$\alpha_{Tx}$	$\alpha_{gx}$	$b_{lx}$	$b_{lx,T}$	$b_{lx,g}$
<i>l=1</i>					
U	2.55827e+00	-9.44029e-03	6.86440e-01	-1.35877e-02	-2.13902e-04
B	2.02976e+00	-9.88741e-03	6.84945e-01	-1.93784e-02	-9.19858e-04
V	1.81454e+00	-4.38065e-04	6.82739e-01	-1.60495e-02	-1.91847e-04
R	1.71773e+00	-1.30255e-03	6.80274e-01	-9.93252e-03	-1.67575e-04
I	1.59319e+00	-2.00633e-03	6.77747e-01	-3.46771e-03	-3.34334e-05
<i>l=2</i>					
U	2.55827e+00	-9.44029e-03	2.84671e-01	-2.52137e-02	-3.57770e-04
B	2.02976e+00	-9.88741e-03	2.81883e-01	-3.41905e-02	-1.61503e-03
V	1.81454e+00	-4.38065e-04	2.78062e-01	-2.86214e-02	-3.41634e-04
R	1.71773e+00	-1.30255e-03	2.73758e-01	-1.81031e-02	-2.98321e-04
I	1.59319e+00	-2.00633e-03	2.69344e-01	-6.92282e-03	-5.62310e-05
<i>l=3</i>					
U	2.55827e+00	-9.44029e-03	2.77314e-02	-2.24244e-02	-2.45991e-04
B	2.02976e+00	-9.88741e-03	2.52149e-02	-2.70928e-02	-1.26624e-03
V	1.81454e+00	-4.38065e-04	2.23207e-02	-2.32581e-02	-2.77800e-04
R	1.71773e+00	-1.30255e-03	1.89973e-02	-1.54544e-02	-2.42536e-04
I	1.59319e+00	-2.00633e-03	1.55810e-02	-7.03719e-03	-3.96414e-05
<i>l=4</i>					
U	2.55827e+00	-9.44029e-03	-3.20092e-02	-9.31317e-03	-1.84146e-05
B	2.02976e+00	-9.88741e-03	-3.31155e-02	-7.28935e-03	-3.27026e-04
V	1.81454e+00	-4.38065e-04	-3.37299e-02	-6.98455e-03	-8.61390e-05
R	1.71773e+00	-1.30255e-03	-3.45198e-02	-5.57709e-03	-7.54679e-05
I	1.59319e+00	-2.00633e-03	-3.53407e-02	-3.89855e-03	-5.21899e-06
<i>l=5</i>					
U	2.55827e+00	-9.44029e-03	2.29813e-03	7.35094e-04	7.80329e-05
B	2.02976e+00	-9.88741e-03	2.29739e-03	4.39081e-03	2.10197e-04
V	1.81454e+00	-4.38065e-04	2.88750e-03	3.20848e-03	3.19444e-05
R	1.71773e+00	-1.30255e-03	3.49885e-03	1.36516e-03	2.70668e-05
I	1.59319e+00	-2.00633e-03	4.12129e-03	-5.06197e-04	9.33007e-06
<i>l=6</i>					

Table 3—Continued

Filter	$\alpha_{Tx}$	$\alpha_{gx}$	$b_{lx}$	$b_{lx,T}$	$b_{lx,g}$
U	2.55827e+00	-9.44029e-03	2.84314e-02	1.14630e-03	7.21713e-06
B	2.02976e+00	-9.88741e-03	2.85101e-02	1.43976e-03	5.62154e-05
V	1.81454e+00	-4.38065e-04	2.86265e-02	1.36594e-03	9.79649e-06
R	1.71773e+00	-1.30255e-03	2.87730e-02	9.96041e-04	7.43661e-06
I	1.59319e+00	-2.00633e-03	2.89270e-02	5.57062e-04	-1.04396e-06

Table 4. Equilibrium Models for a sequence of subdwarf B stars with  $M_*/M_\odot=0.48$

No.	$T_{\text{eff}}(\text{K})$	$\log g$	$\log q(H)$	$\Delta P$ (s)
PG 1716 stars				
1	22,000	5.13	-1.64	4500–9500
2	23,000	5.19	-1.81	4000–8000
3	24,000	5.25	-1.97	3500–6500
4	25,000	5.31	-2.13	3000–5700
5	26,000	5.37	-2.30	2500–5000
6	27,000	5.44	-2.46	2300–4000
7	28,000	5.50	-2.62	2000–3500
EC 14026 stars				
8	29,000	5.56	-2.79	220–450
9	30,000	5.62	-2.95	190–450
10	31,000	5.68	-3.12	170–360
11	32,000	5.75	-3.28	150–260
12	33,000	5.81	-3.44	110–200
13	34,000	5.87	-3.61	100–150
14	35,000	5.93	-3.77	95–110

Table 5. Fit of predicted u'g'r' amplitudes to those observed for the 182.4-s mode of KPD 2109+4401 by Jeffery et al. (2004)

Degree index $l$	$\chi^2$	Q
0	0.736	0.692
1	22.6	$1.24 \times 10^{-5}$
2	96.0	$1.43 \times 10^{-24}$
3	1470	0.00
4	1150	0.00
5	4860	0.00

## REFERENCES

- Aerts, C., Cuypers, J., De Cat, P., Dupret, M.-A., de Ridder, J., Eyer, L., Scuflaire, R., & Waelkens, C. 2004, *A&A*, 432, 1013
- Balona, L.A., & Evers, E.A. 1999, *MNRAS*, 302, 349
- Balona, L.A., & Stobie, R.S. 1979, *MNRAS*, 187, 217
- Bergeron, P., Wesemael, F., Beauchamp, A., Wood, M.A., Lamontagne, R., Fontaine, G., & Liebert, J. 1994, *ApJ*, 432, 305
- Billères, M., Fontaine, G., Brassard, P., & Liebert, J. 2002, *ApJ*, 578, 515
- Brassard, P., Fontaine, G., Billères, M., Charpinet, S., Liebert, J., & Saffer, R.A. 2001, *ApJ*, 563, 1013
- Brassard, P., Fontaine, G., & Wesemael, F. 1995, *ApJS*, 96, 545
- Buta, R.J., & Smith, M.A. 1979, *ApJ*, 232, 213
- Breger, M., Handler, G., Garrido, R., Audard, N., Beichbuchner, F., Zima, W., Paparo, M., Zhi-Ping, L., Shi-Yang, J., Zong-li, L., Ai-ying, Z., Pikall, H., Stankov, A., Guzik, J.A., Sperl, M., Krzesinski, J., Ogloza, W., Pajdosz, G., Zola, S., Serkowitsch, E., Reegen, P., Rumpf, T., & Schmalwieser, A. 1997, *A&A*, 324, 566
- Charpinet, S., Fontaine, G., Brassard, P., Green, E.M., and Chayer, P. 2005, *A&A*, in press
- Charpinet, S., Fontaine, G., & Brassard, P. 2003, in *NATO ASIB Proc. 105: White Dwarfs*, 69
- Charpinet, S., Fontaine, G., Brassard, P., & Dorman, B. 2002, *ApJS*, 140, 469
- Charpinet, S., Fontaine, G., & Brassard, P. 2001, *PASP*, 113, 785
- Charpinet, S., Fontaine, G., Brassard, P., Chayer, P., Rogers, F.J., Iglesias, C.A., & Dorman, B. 1997, *ApJ*, 483, L123
- Charpinet, S., Fontaine, G., Brassard, P., & Dorman, B. 1996, *ApJ*, 471, L103
- Cugier, H., & Daszyńska, J. 2001, *A&A*, 377, 113
- Cugier, H., Dziembowski, W., & Pamyatnykh, A.A. 1994, *A&A*, 291, 143
- De Cat, P., Briquet, M., Daszyńska-Daskiewicz, J., Dupret, M.-A., de Ridder, J., Scuflaire, R., & Aerts, C. 2005, *A&A*, 432, 1013
- Dorman, B. 1995, in *Proc. 32d Liège Astrophys. Colloq., Stellar Evolution: What Should be Done?*, ed. A. Noels, D. Fraipont-Caro, M. Gabriel, N. Grevesse, & P. Demarque (Liège: Institut d'Astrophysique), 291

- Dupret, M.-A. 2001, *A&A*, 366, 166
- Dupret, M.-A., De Ridder, J., De Cat, P., Aerts, C., Scufflaire, R., Noels, A., & Thoul, A. 2003, *A&A*, 398, 677
- Dziembowski, W., 1977, *Acta Astron.* 27, 203
- Dziembowski, W., & Pamyatnykh, A.A. 1993, *MNRAS*, 262, 204
- Dziembowski, W., Moskalik, P., & Pamyatnykh, A.A. 1993, *MNRAS*, 265, 588
- Falter, S., Heber, U., Dreizler, S., Schuch, S.L., Cordes, O., & Edelman, H. 2003, *A&A*, 401, 289
- Fontaine, G., Green, E.M., Brassard, P., Charpinet, S., Chayer, P., Billères, M., Randall, S.K., & Dorman, B. 2004, *Ap&SS*, 291, 379
- Fontaine, G., Brassard, P., Charpinet, S., Green, E.M. and Willems, B., 2003a, *Asteroseismology Across the HR Diagram*. Proceedings of the Asteroseismology Workshop, Porto, Portugal, 1-5 July, 2002. Ed. M.J. Thompson, M.S. Cunha, M.J.P.F.G. Monteiro. Reprinted from *Astrophysics & Space Science*, Volume 284, No. 1, 2003. Kluwer Academic Publishers, Dordrecht., 517
- Fontaine, G., Brassard, P., Charpinet, S., Green, E.M., Chayer, P., Billères, M., & Randall, S.K. 2003b, *ApJ*, 597, 518
- Fontaine, G., Charpinet, S., Brassard, P., Chayer, P., Rogers, F.J., Iglesias, C.A., & Dorman, B. 1998, in *IAU Symposium No. 185, New Eyes to See Inside the Sun and Stars*, ed. F.-L. Deubner, J. Christensen-Dalsgaard and D. Kurtz, Kyoto, Japan, 18-22 August 1997, 367
- Fontaine, G., Brassard, P., Bergeron, P., & Wesemael, F. 1996, *ApJ*, 469, 320
- Gautschy, A., & Saio, H. 1993, *MNRAS*, 262, 213
- Garrido, R., García-Lobo, E., & Rodríguez, E. 1990, *A&A*, 234, 262
- Green, E.M., Callera, K., Seitzzahl, I.R., White, B.A., Hyde, E.A., Giovanni, M., Reed, M., Fontaine, G., & Ostensen, R. 2003a, *Ap&SS*, 284, 65
- Green, E.M., Fontaine, G., Reed, M.D., Callera, K., Seitzzahl, I.R., White, B.A., Hyde, E.A., Ostensen, R., Cordes, O., Brassard, P., Falter, S., Jeffery, E.J., Dreizler, S., Schuh, S.L., Giovanni, M., Edelman, H., J. Rigby, & Bronowska, A. 2003b, *ApJ*, 583, L31
- Heber, U. 1986, *A&A*, 155, 33
- Heynderickx, D., Waelkens, C., & Smeyers, P. 1994, *A&A*, 105, 447
- Jackson, J.D. 1975, *Classical Electrodynamics*, 2nd ed. (New York: Wiley & Sons)

- Jeffery, C.S., Dhillon, V., Marsh, T., & Ramachandran, B. 2004, MNRAS, 352, 699
- Kilkenny, D., Billères, M., Stobie, R.S., Fontaine, G., Shobbrook, R.R., O’Donoghue, D., Brassard, P., Sullivan, D.J., Burleigh, M.R., & Barstow, M.A. 2002, MNRAS, 331, 399
- Kilkenny, D., Koen, C., O’Donoghue, D., & Stobie, R.S. 1997, MNRAS, 285, 640
- Koen, C., 1998 MNRAS, 300, 567
- Koen, C., Kilkenny, D., O’Donoghue, D., Van Wyk, F., & Stobie, R.S. 1997, MNRAS, 285, 645
- Kurucz, R.L. 1993, Atlas9 Stellar Atmosphere Programs, Kurucz CDROM No. 13
- O’Donoghue, D., Lynas-Gray, A.E., Kilkenny, D., Stobie, R.S., & Koen, C. 1997, MNRAS, 285, 657
- Osaki, Y., 1971, PASJ, 23, 485
- Oreiro, R., Pérez Hernández, F., Ulla, A., Garrido, R., Ostensen, R., & MacDonald, J. 2005, preprint
- Press, W.H., Flannery, B.P., Teukolsky, S.A., & Vetterling, W.T. 1986, Numerical Recipes (Cambridge: Cambridge University Press)
- Ramachandran, B., Jeffery, C.S., & Townsend, R.H.D. 2004, A&A, 428, 209
- Randall, S., Fontaine, G., Green, E., Kilkenny, D., Crause, L., Cordes, O., O’Toole, S., Kiss, L., For, B.-Q., & Quirion, P.-O. 2004a, Ap&SS, 291, 465
- Randall, S.K., Fontaine, G., Green, E.M., Brassard, P., & Terndrup, D.M. 2004b, Proceedings of the SOHO 14/GONG 2004 Workshop (ESA SP-559). “Helio- and Asteroseismology: Towards a Golden Future”. 12-16 July 2004, New Haven, Connecticut, USA. Ed. D. Danesy, 119
- Randall, S.K., Matthews, J.M., Fontaine, G., Rowe, J., Kuschnig, R., Green, E.M., Brassard, P., Chayer, P., Guenther, D.B., Moffat, A.F.J., Rucinski, S., Sasselov, D., Walker, G.A.H., & Weiss, W.W. 2005, ApJ, submitted
- Robinson, E.L., Kepler, S.O., & Nather, R.E. 1982, ApJ, 259, 219
- Saffer, R., Bergeron, P., Koester, D., & Liebert, J. 1994, ApJ, 432, 351
- Silvotti, R., Ostensen, R., Heber, U., Solheim, J.-E., Dreizler, S., & Altmann, M. 2002, A&A, 383, 239
- Stamford, P.A., & Watson, R.D. 1981, Ap&SS, 77, 131
- Stobie, R.S., Kawaler, S.D., Kilkenny, D., O’Donoghue, D., & Koen, C. 1997, MNRAS, 285, 651



Townsend, R.H.D. 2002, MNRAS, 330, 855

Townsend, R.H.D. 2003, MNRAS, 343, 125

Watson, R.D. 1988, Ap&SS, 140, 255

Wade, R.A., & Rucinski, S.M. 1985, A&AS, 60, 471

### FIGURE CAPTIONS

Fig. 1 — Behavior of some key monochromatic quantities for our representative EC 14026 star model. The latter has  $\log g = 5.75$  and  $T_{\text{eff}} = 33,000$  K. Top panel: Unperturbed emergent Eddington flux in the optical domain. Middle panel: First order perturbation to the flux caused by a nonradial pulsation with a period of 150 s ( $p$ -mode); at 3500 Å, from top to bottom, each curve is characterized by a value of the degree index  $l = 0, 1, 2, 4, 3,$  and 5. Bottom panel: Similar to the middle panel, but, this time, illustrating the *relative* amplitude of the perturbation.

Fig. 2 — Logarithm of monochromatic amplitude ratios with respect to an arbitrary spectral point at 3650 Å. This again refers to our representative EC 14026 star model and for a mode with a period of 150 s and degree index  $l = 0$  (cyan), 1 (red), 2 (blue), 3 (green), 4 (magenta), and 5 (black).

Fig. 3 — Similar to Figure 2, but for monochromatic phase differences.

Fig. 4 — Behaviour of the radial component of the pressure eigenfunction in the atmospheric layers of interest for our representative EC 14026 star model on the basis of modes with degree indices from  $l = 0$  to 5 for all periods in the range 80–300 s. The vertical dotted lines correspond, from right to left, to Rosseland optical depths of  $\tau = 0.1, 1.0,$  and 10.0, respectively.

Fig. 5 — Similar to Figure 4, but for our representative PG 1716 model and considering modes with  $l = 1, 2$  and 3 in the period range 2000–6000 s.

Fig. 6 —  $R$  values for our representative EC 14026 model in the atmospheric layers of interest for periods in the range 80–300 s. The curves for different degree indices are illustrated separately as indicated.

Fig. 7 — Similar to Figure 6, but for the quantity  $\psi_T - \pi$ .

Fig. 8 — Cubic fit to computed  $\langle R \rangle$  (continuous line) and  $\langle \psi_T \rangle$  (dashed line) values as a function of period for our representative EC 14026 star model.

Fig. 9 —  $R$  values for our representative PG 1716 model in the atmospheric layers of interest for periods in the range 2000–6000 s. The curves for different degree indices are illustrated separately as indicated.

Fig. 10 — Similar to Figure 9, but for the quantity  $\psi_T - \pi$ .

Fig. 11 — Cubic fit to computed  $\langle R \rangle$  (continuous line) and  $\langle \psi_T \rangle$  (dashed line) values as a function of period and of degree index  $l$  for our representative PG 1716 star model.

Fig. 12 — Relative importance of the temperature terms ( $\gamma_1$ ) compared to the radius and surface gravity terms ( $\gamma_2$ ) for our representative EC 14026 star model in the *UBVRI* bandpasses. Continuous lines indicate the results obtained by fitting  $\langle R \rangle$  and  $\langle \psi_T \rangle$  according to equations (44) and (45) while dotted curves represent results obtained by setting the two parameters to their adiabatic values of  $\langle R \rangle = 1$  and  $\langle \psi_T \rangle = \pi$ . Three typical periods (low-order  $p$ -modes) of 100, 150, and 200 s, as well as six values of the degree index,  $l = 0-5$ , are considered. The effective wavelengths of the various bandpasses are 3650 Å(*U*), 4400 Å(*B*), 5500 Å(*V*), 6500 Å(*R*), and 8000 Å(*I*).

Fig. 13 — Phase shifts relative to the *U* filter calculated for our EC 14026 star model for the *UBVRI* bandpasses. Continuous lines represent full non-adiabatic results while the dashed curve indicates the adiabatic values (which are always equal to zero).

Fig. 14 — Amplitude ratios relative to the *U* filter calculated for our EC 14026 star model for the *UBVRI* bandpasses. Continuous lines represent full non-adiabatic results while the dashed curves indicates the adiabatic values obtained by forcing  $\langle R \rangle = 1$  and  $\langle \psi_T \rangle = \pi$ .

Fig. 15 — Amplitude ratios relative to the *U* filter calculated for our EC 14026 star model for the *UBVRI* bandpasses. The  $l$  indices of the modes are indicated. Dotted, dashed and long-dashed lines refer to periods with 100, 150 and 200 s respectively. They are compared to the amplitude ratios obtained in the limit where  $\gamma_2 = 0$  (continuous curves).

Fig. 16 — Results of a numerical experiment in which the amplitude ratios relative to the *U* band were obtained by adopting  $T_3 = 0$  (dotted lines) and by setting  $\gamma_2 = 0$  (continuous lines).

Fig. 17 — Similar to Figure 12, but referring to our representative PG 1716 model. Six periods from 2400 s to 6000 s as well as six values of  $l$  from 1 to 6 are considered. For the continuous lines,  $\langle R \rangle$  and  $\langle \psi_T \rangle$  were derived from equations (46) and (47) while adiabatic values were imposed for the dotted lines.

Fig. 18 — Similar to Figure 13, but referring to our representative PG 1716 model. Note the change of ordinate scale between panel a) and panel b).

Fig. 19 — Similar to Figure 14, but referring to our representative PG 1716 model.

Fig. 20 — Similar to Figure 15, but referring to our representative PG 1716 model. Amplitude ratios are illustrated for representative periods of  $P = 3000$  s (dotted lines), 4000 s (dashed lines), 5000 s (long-dashed lines), 6000 s (dot-dashed lines), 7000 s (dot-long-dashed lines) and 8000 s (dashed-long-dashed lines). The continuous line refers to the case of  $\gamma_2 = 0$ .

Fig. 21 — Similar to Figure 16, but referring to our representative PG 1716 model.

Fig. 22 —  $I$  to  $U$  amplitude ratio as a function of degree index  $l$  on the basis of modes extending up to  $l = 8$ . From bottom to top, the various curves correspond to periods with  $P = 2400, 3000, 4000, 5000, 6000, 7000, 8000$  and an infinite period respectively.

Fig. 23 — Variation of the  $I/U$  amplitude ratio with period for our representative PG 1716 model. The values for different modes are indicated by points in black ( $l = 1$ ), grey ( $l = 2$ ), blue ( $l = 3$ ), cyan ( $l = 4$ ), green ( $l = 5$ ) and red ( $l = 6$ ).

Fig. 24 — Similar to Figure 23, but for phase differences between oscillations in the  $I$  and  $U$  bandpasses.

Fig. 25 — Phase differences between oscillations in the  $I$  and  $U$  bandpasses for the sequence of subdwarf B star models listed in Table 4. The dotted vertical line divides the PG 1716 star models on the left from the EC 14026 models on the right. We illustrate modes with  $l = 0$  (yellow, EC 14026 models only),  $l = 1$  (black),  $l = 2$  (grey),  $l = 3$  (blue),  $l = 4$  (cyan),  $l = 5$  (green) and  $l = 6$  (red).

Fig. 26 — Similar to Figure 25, but for  $I/U$  amplitude ratios.

Fig. 27 — Behaviour of the  $I/U$  amplitude ratio with effective temperature of a model. (a) EC 14026 regime: the surface gravity was kept constant at  $\log g = 5.75$ , while  $T_{\text{eff}}$  was varied from 29,000 K – 35,000 K in increments of 1000 K. From top to bottom, the curves refer to modes with degree indices  $l = 5, 6, 4, 2, 1, 0$  and 3. (b) PG 1716 regime: we adopted the representative value of  $\log g = 5.40$  and varied the effective temperature from 22,000 K – 28,000 K, again in steps of 1000 K. From top to bottom, the modes in question correspond to  $l = 5, 4, 1, 6, 2$  and 3.

Fig. 28 — Behaviour of the  $I/U$  amplitude ratio with surface gravity. (a) EC 14026 regime: the effective temperature was kept constant at  $T_{\text{eff}} = 33,000$  K, while  $\log g$  was varied from 5.5 – 5.9 in increments of 0.1 dex. From top to bottom on the right hand side, the curves refer to modes with degree indices  $l = 5, 6, 4, 2, 1, 0$  and 3. (b) PG 1716 regime: we adopted the representative value of  $T_{\text{eff}} = 27,000$  K and varied the surface gravity from 5.1 to 5.5, again in steps of 0.1 dex. From top to bottom on the right hand side, the modes in question correspond to  $l = 5, 4, 1, 6, 2$  and 3.

Fig. 29 — Fit to the  $u'$ ,  $g'$  and  $r'$  pulsational amplitudes observed for the 182.4 s mode of KPD 2109+4401 by Jeffery et al. (2004). The predicted amplitude-wavelength behaviours of modes with  $l=0$  to  $l=5$  have been fit to the observed values using a least-squares procedure. Only the  $l=0$  curve provides an acceptable fit.

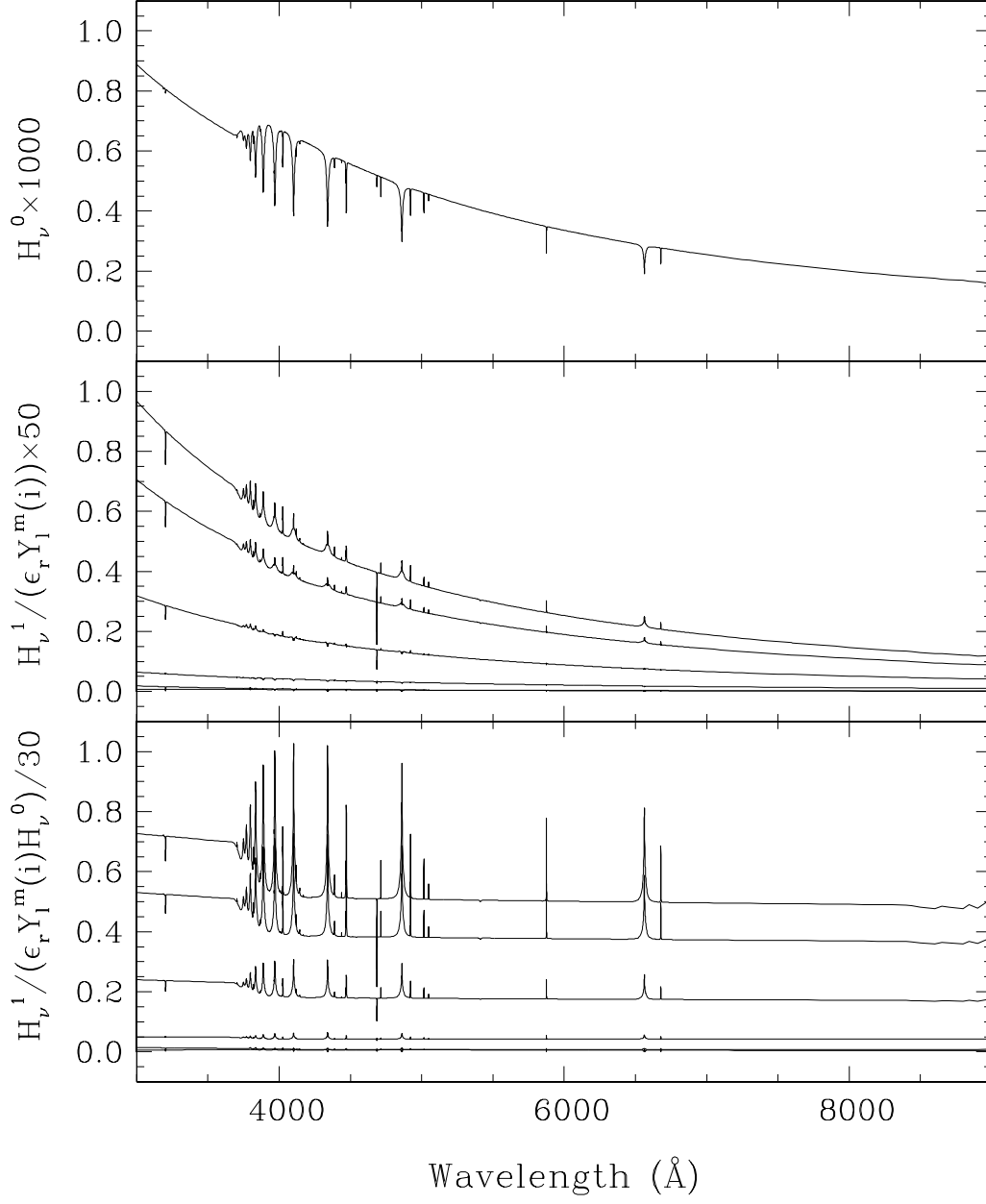


Figure 1

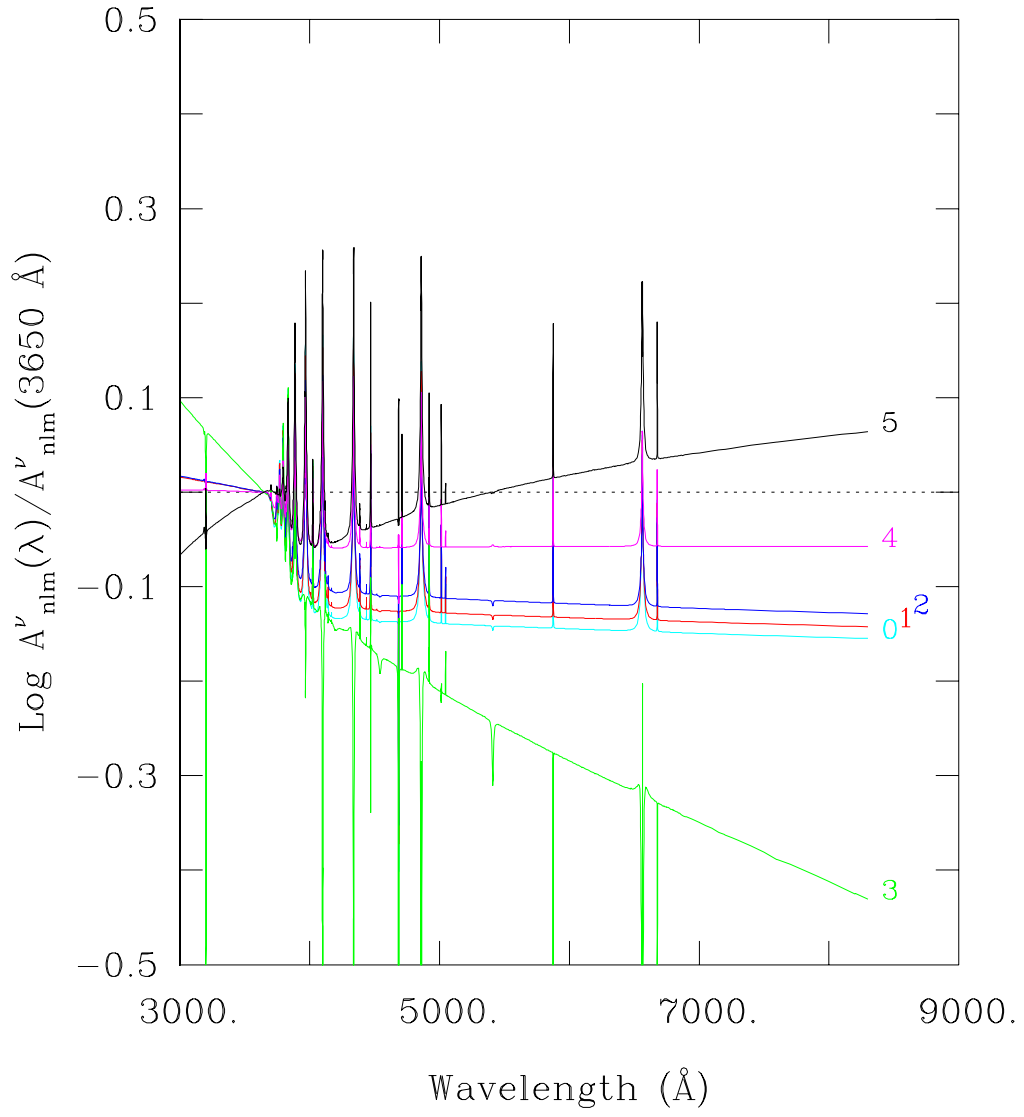


Figure 2

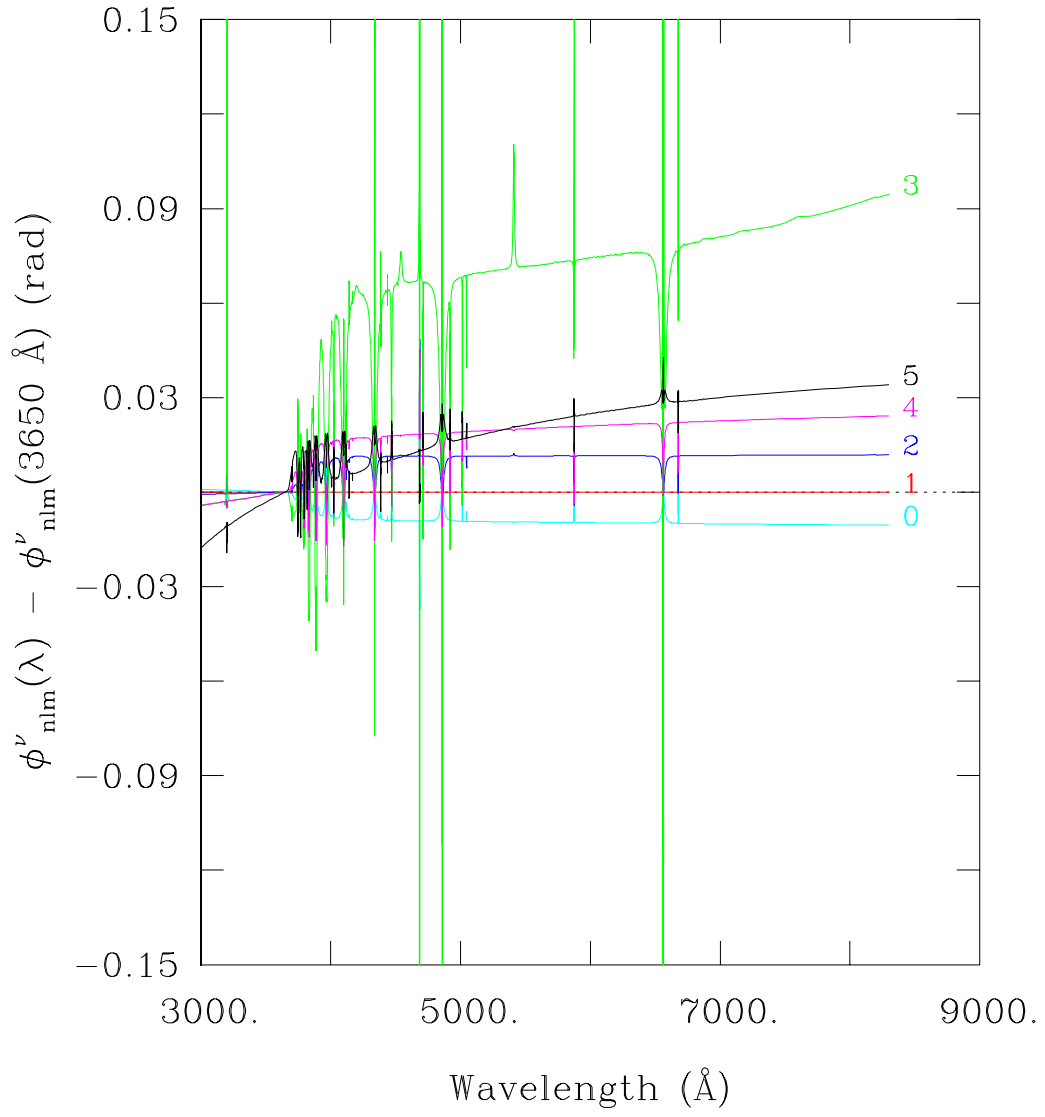


Figure 3

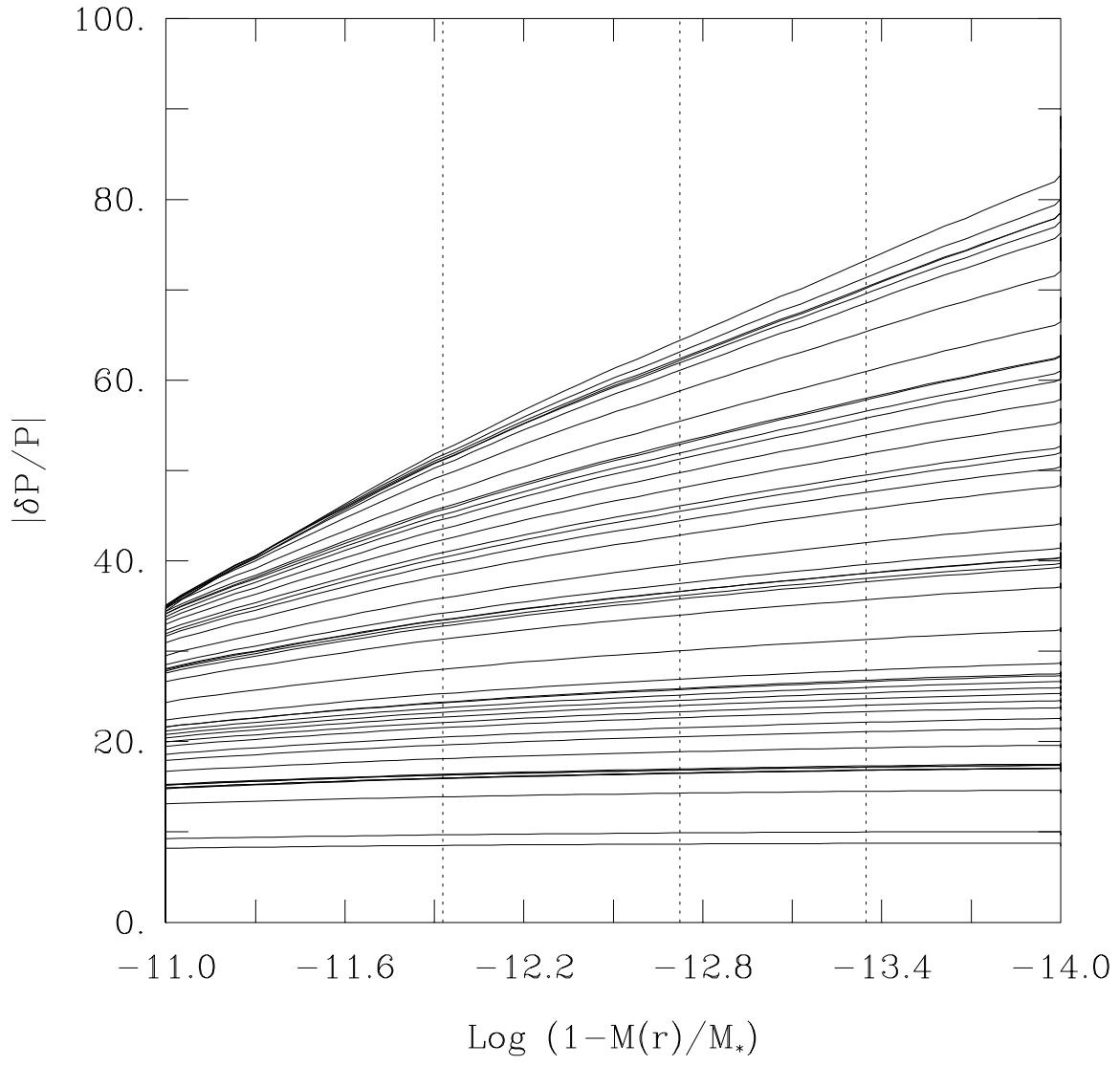


Figure 4



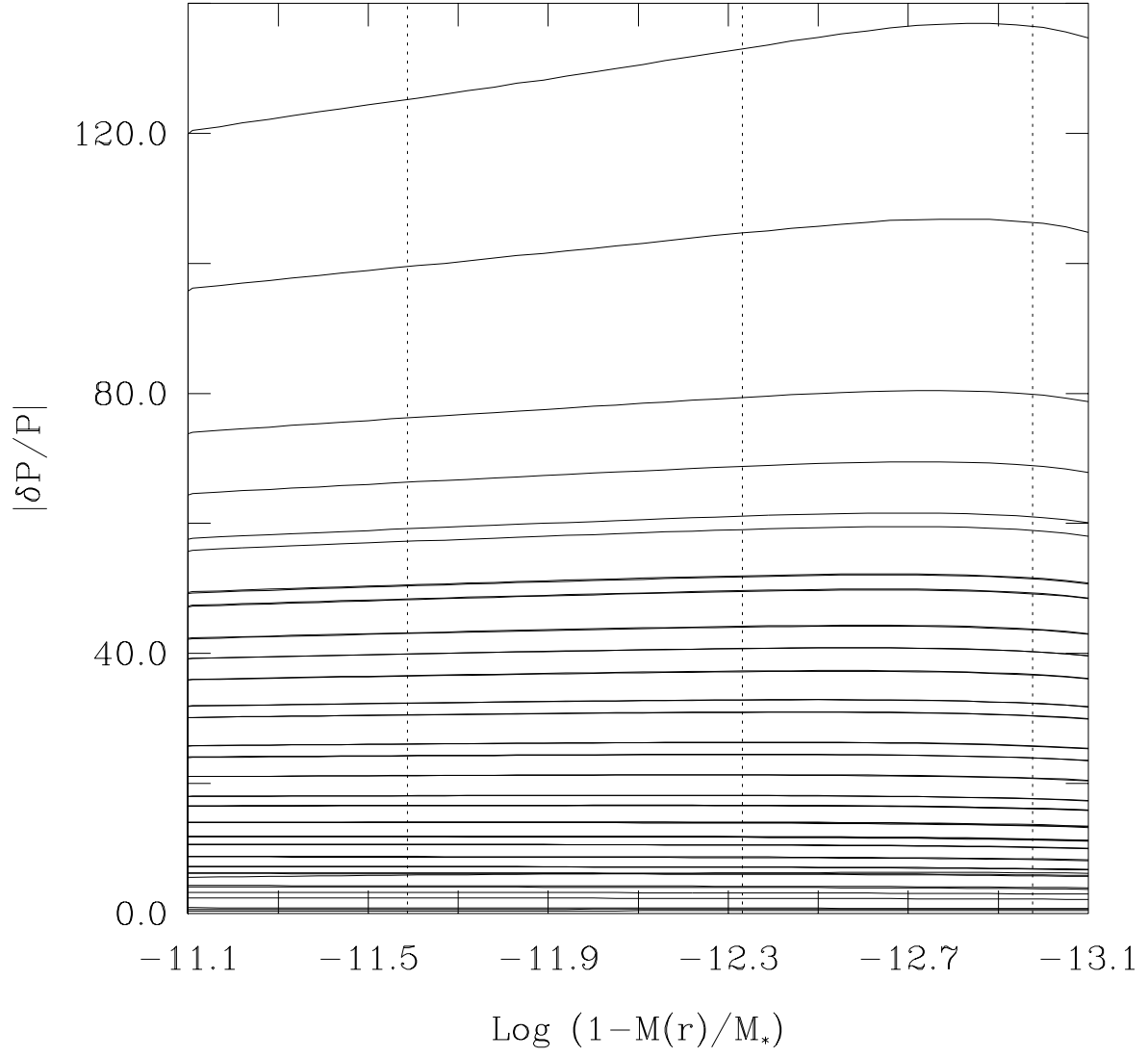


Figure 5

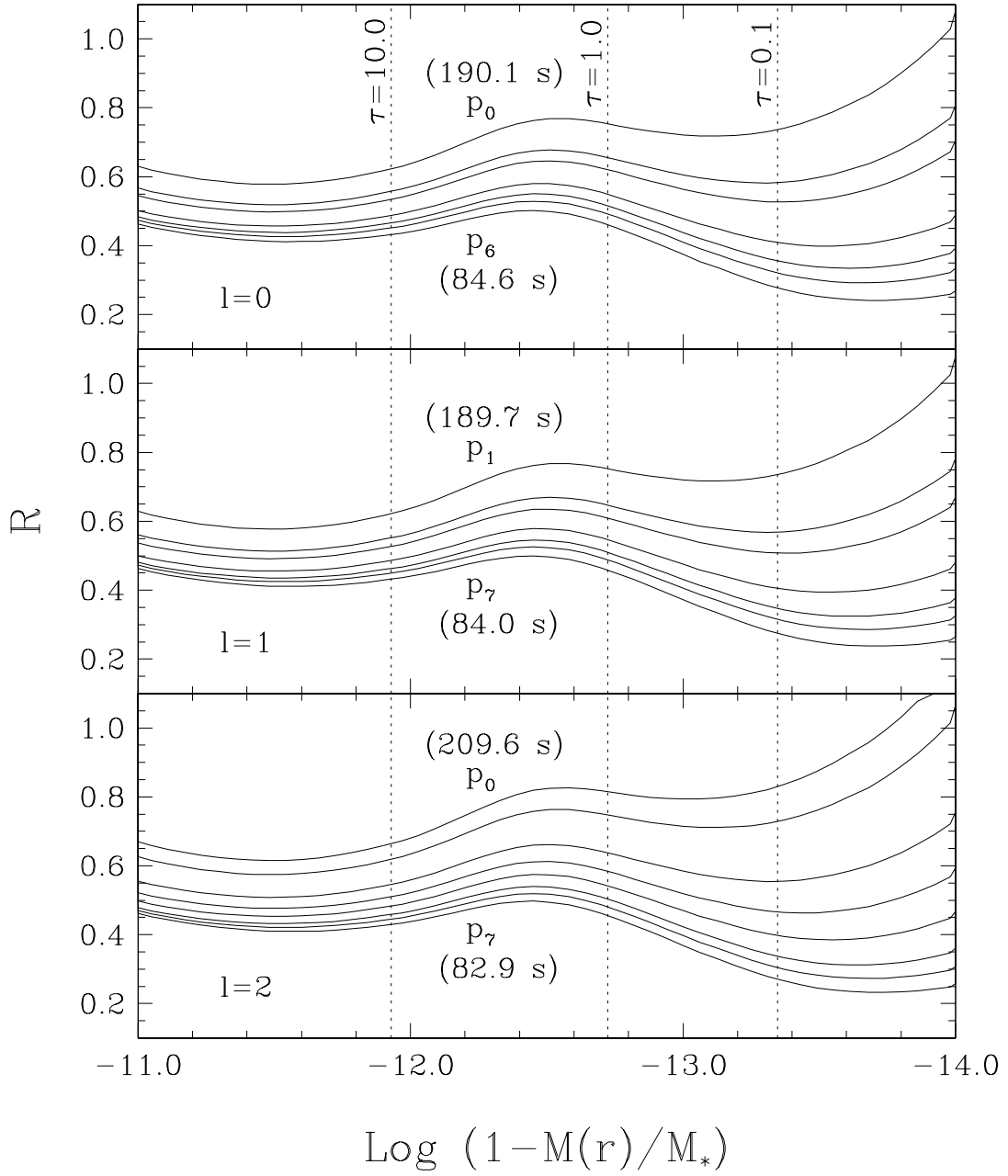


Figure 6a

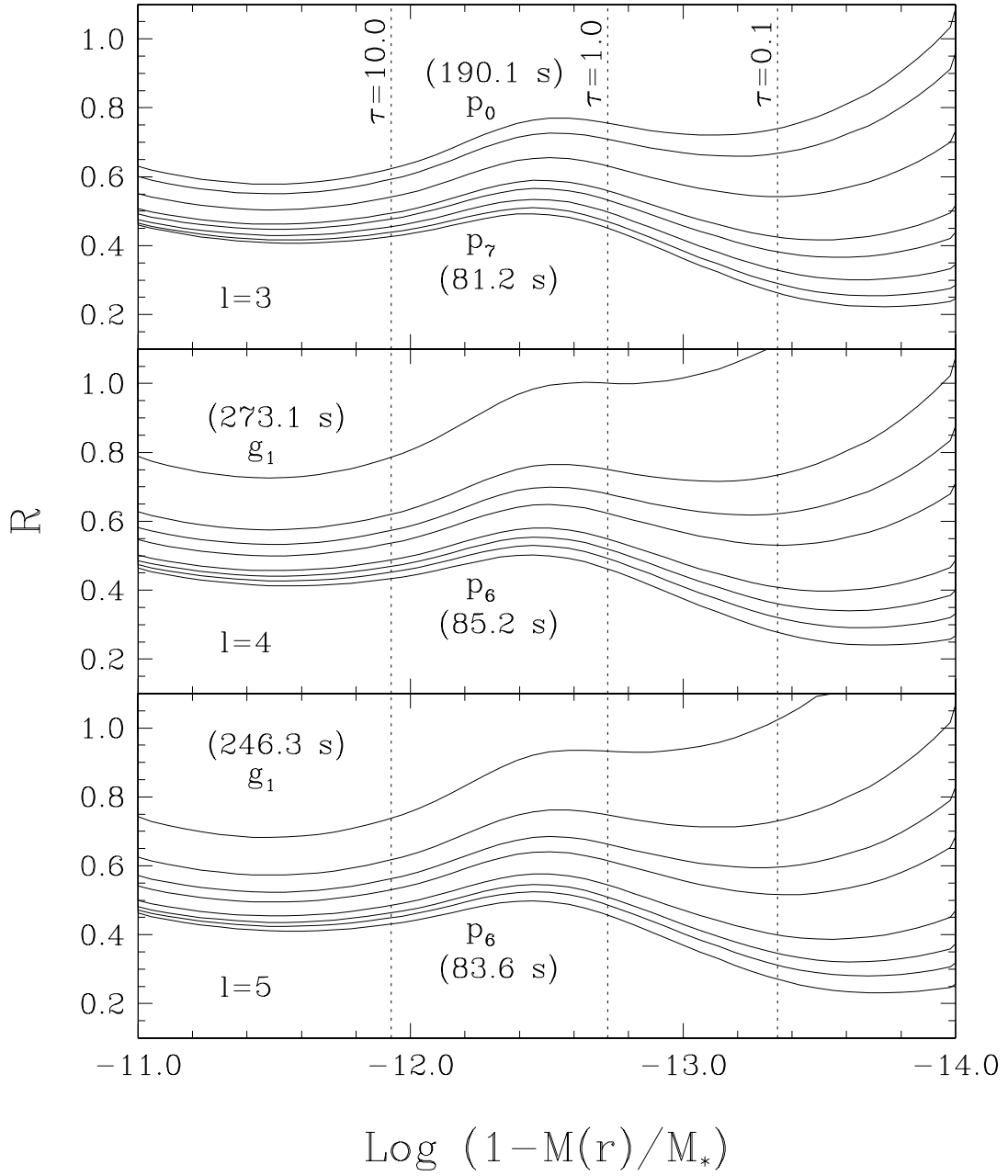


Figure 6b

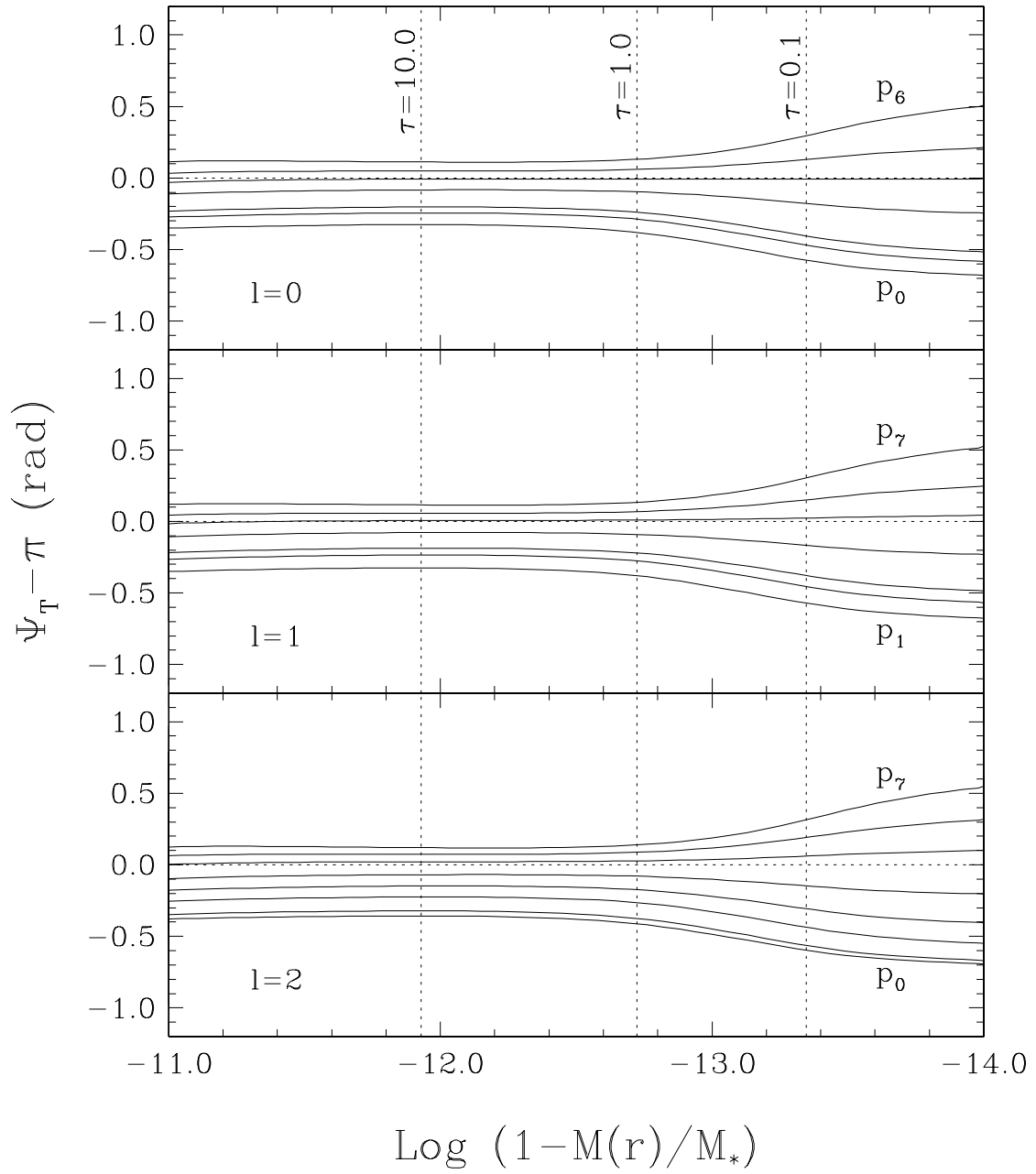


Figure 7a

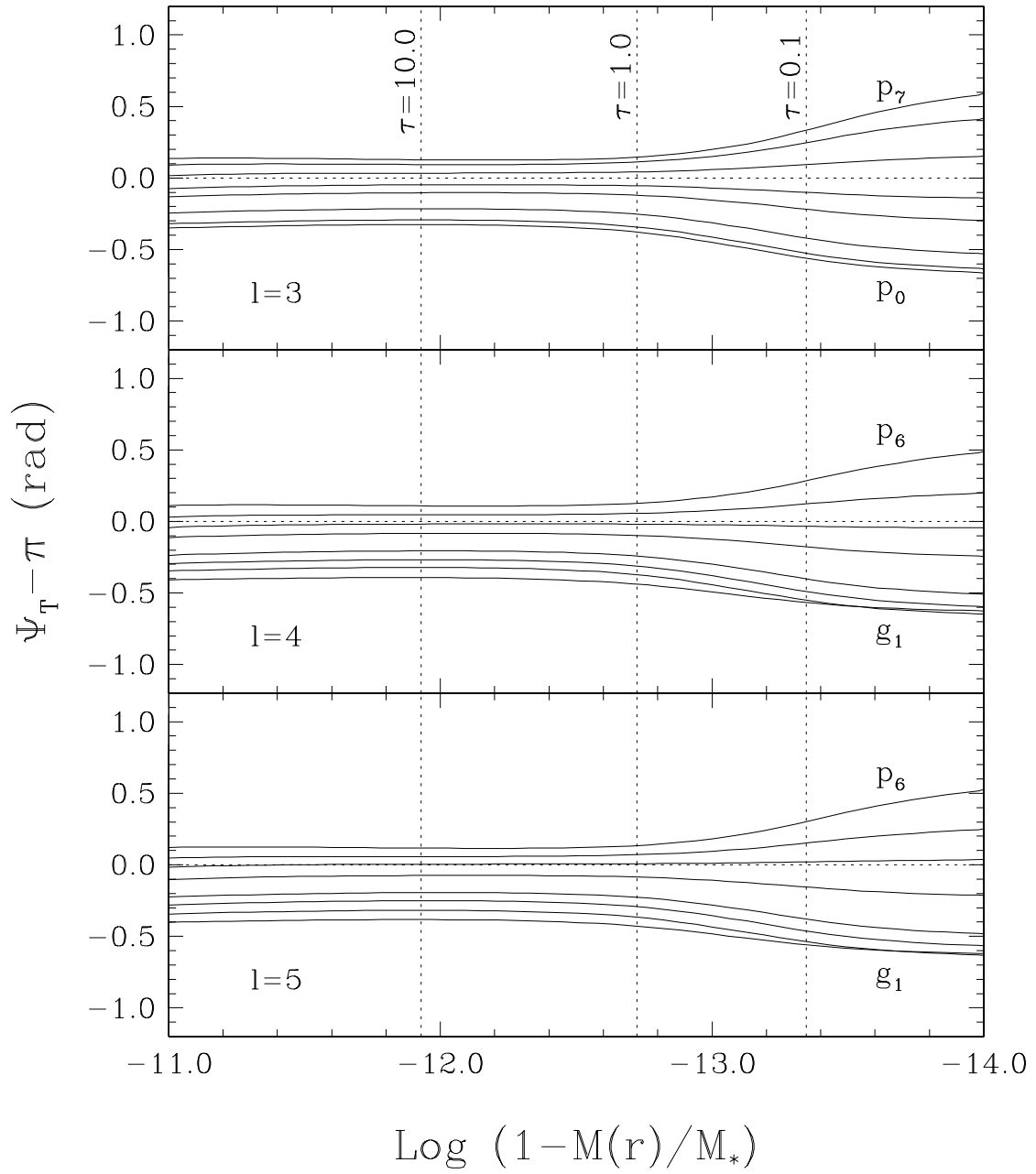


Figure 7b

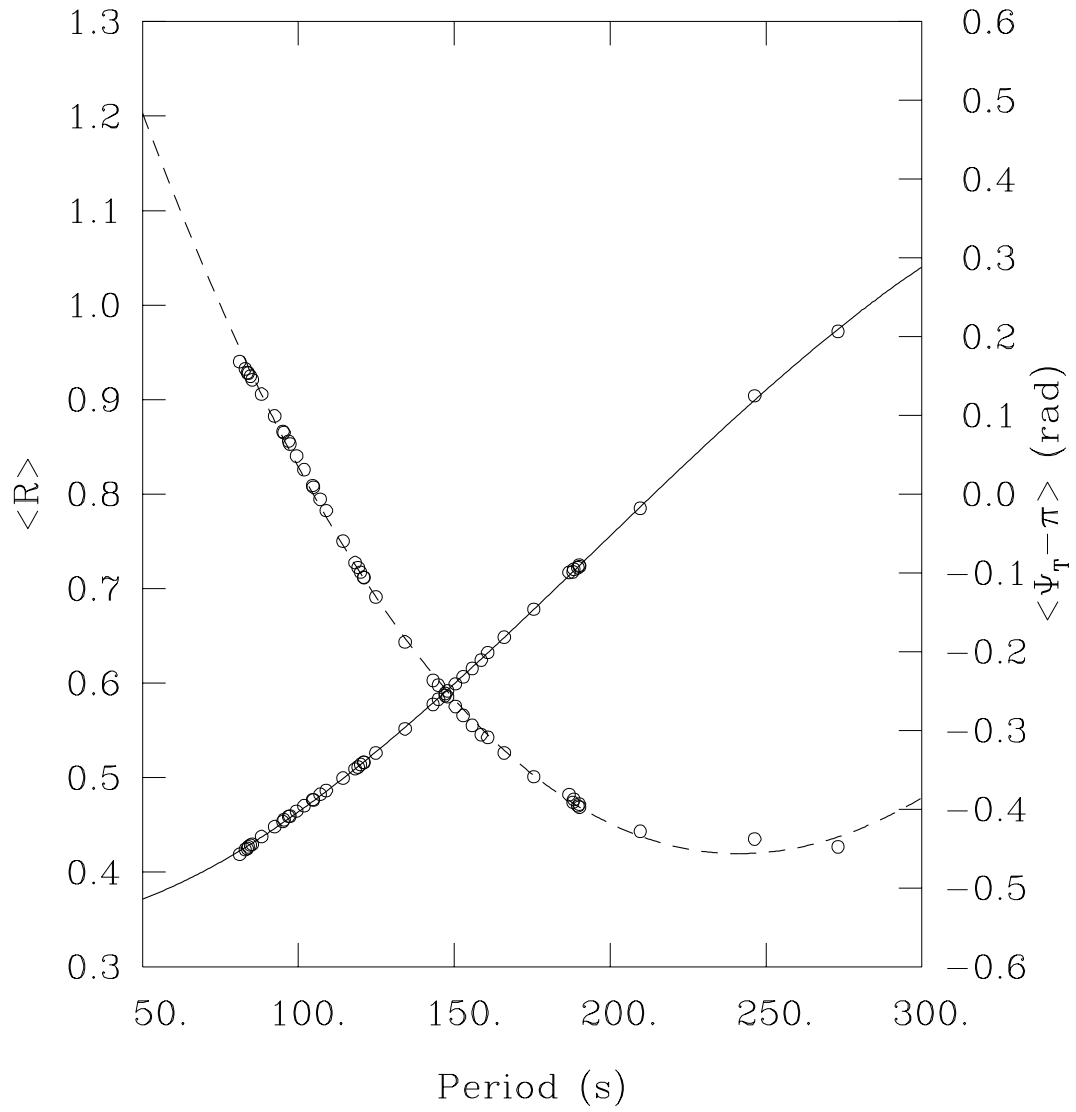


Figure 8

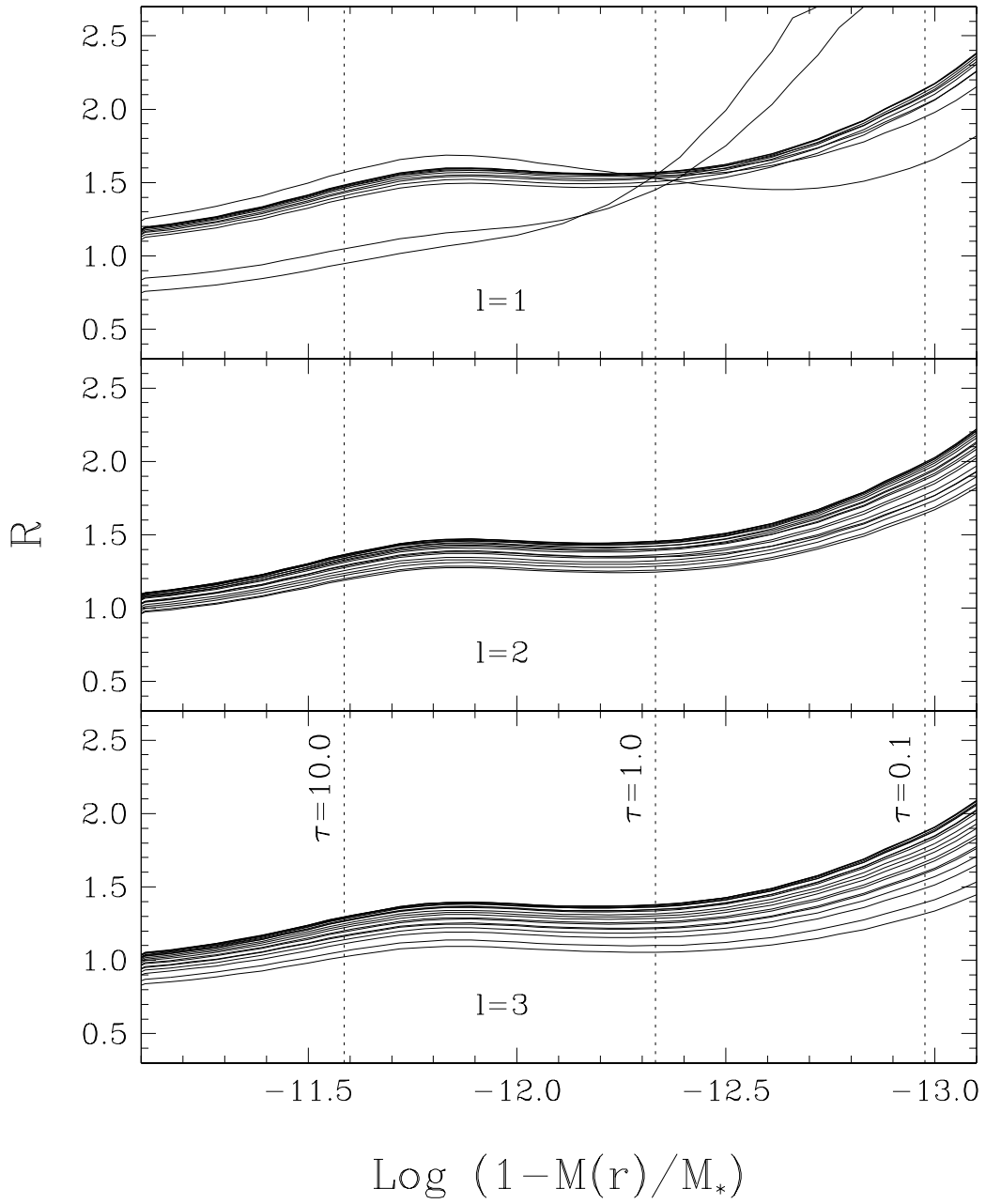


Figure 9

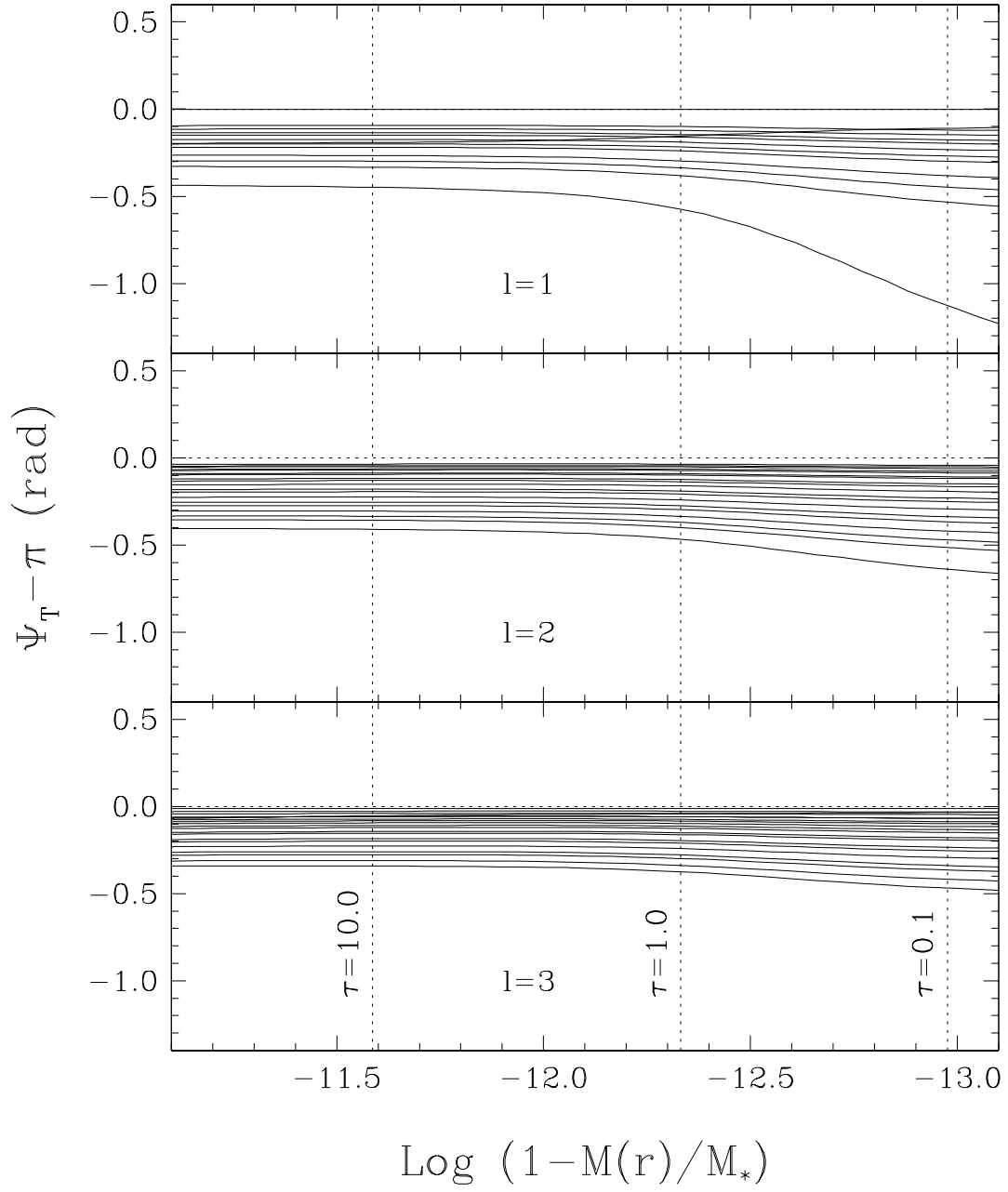


Figure 10



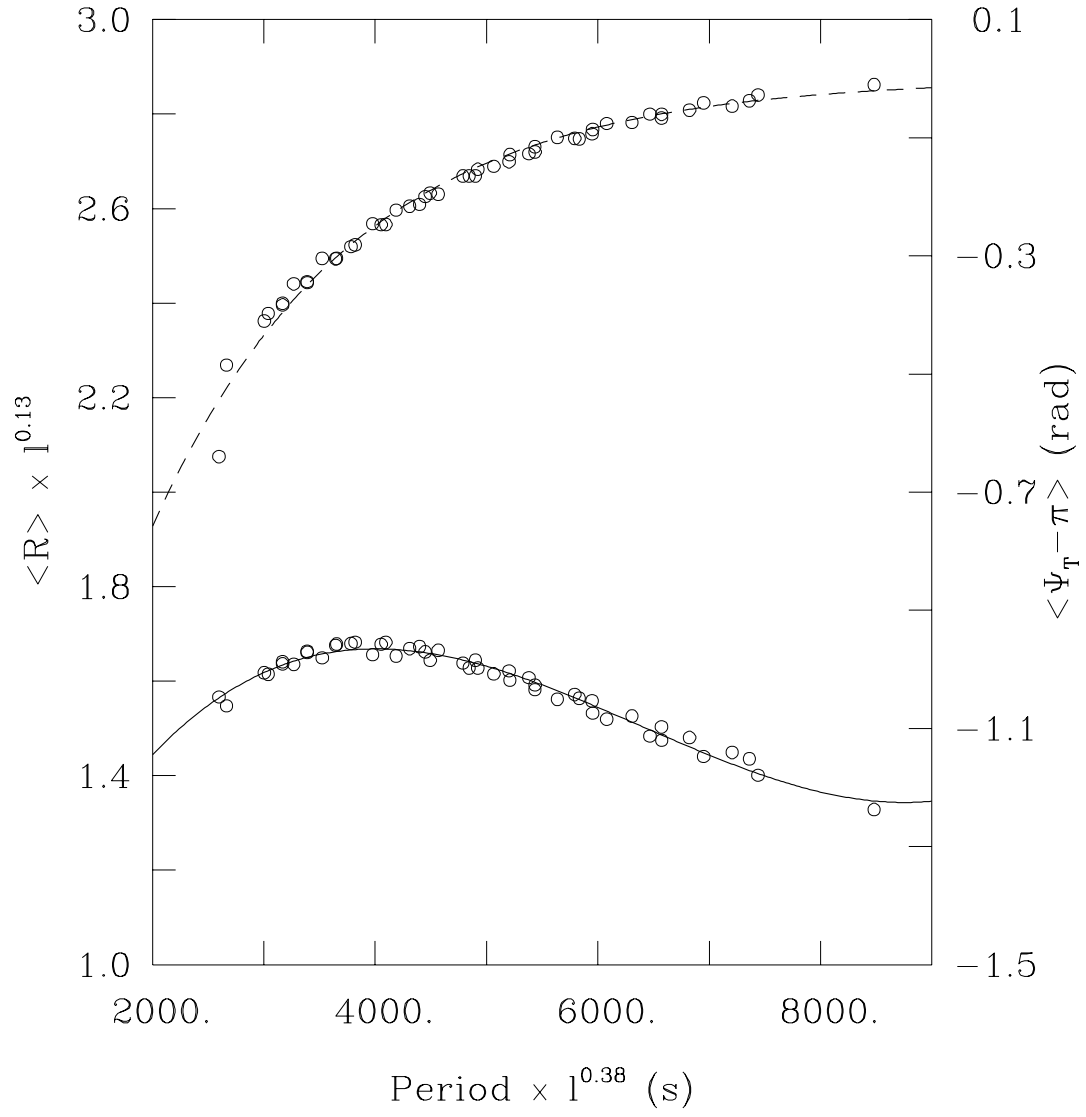


Figure 11

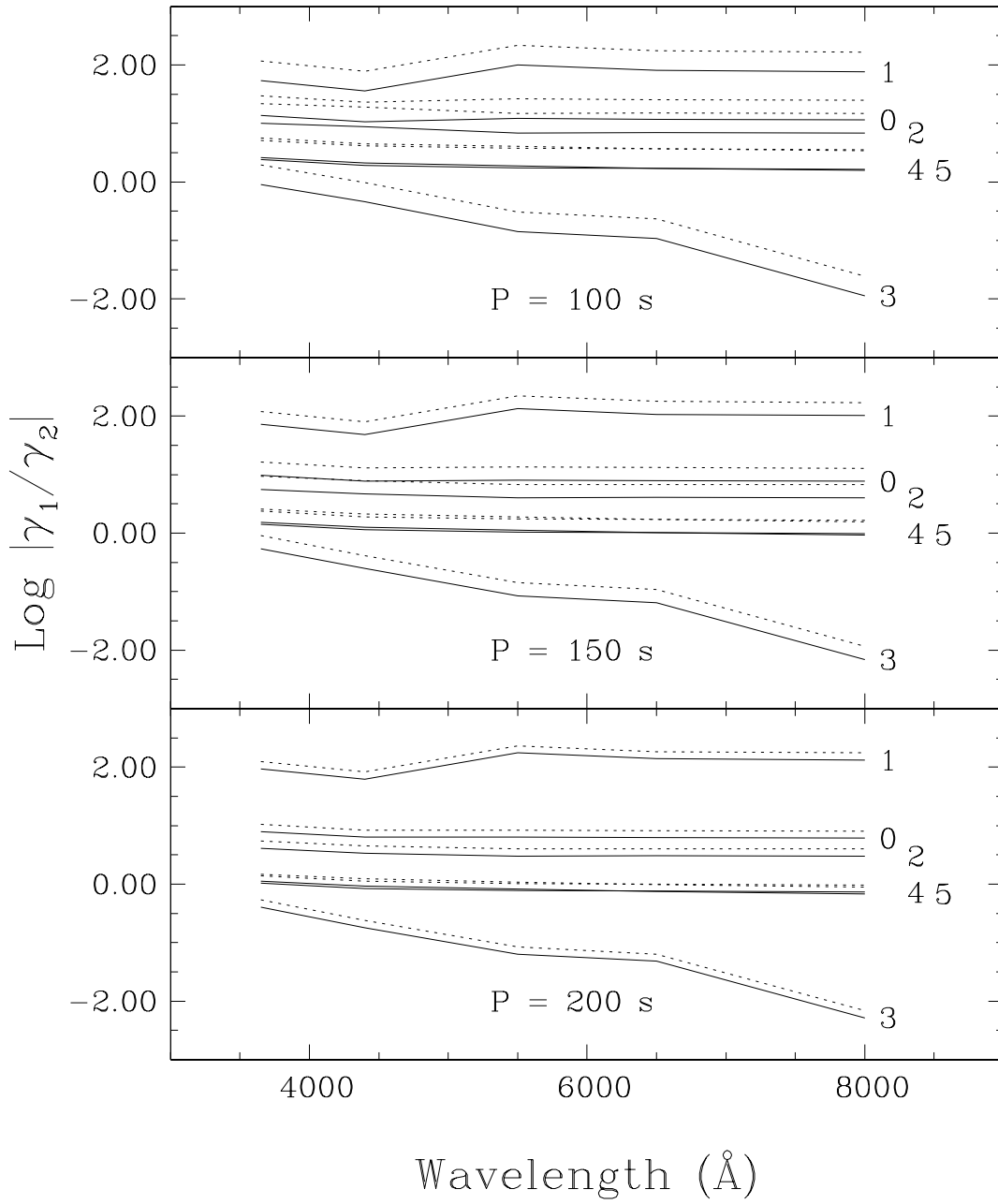


Figure 12

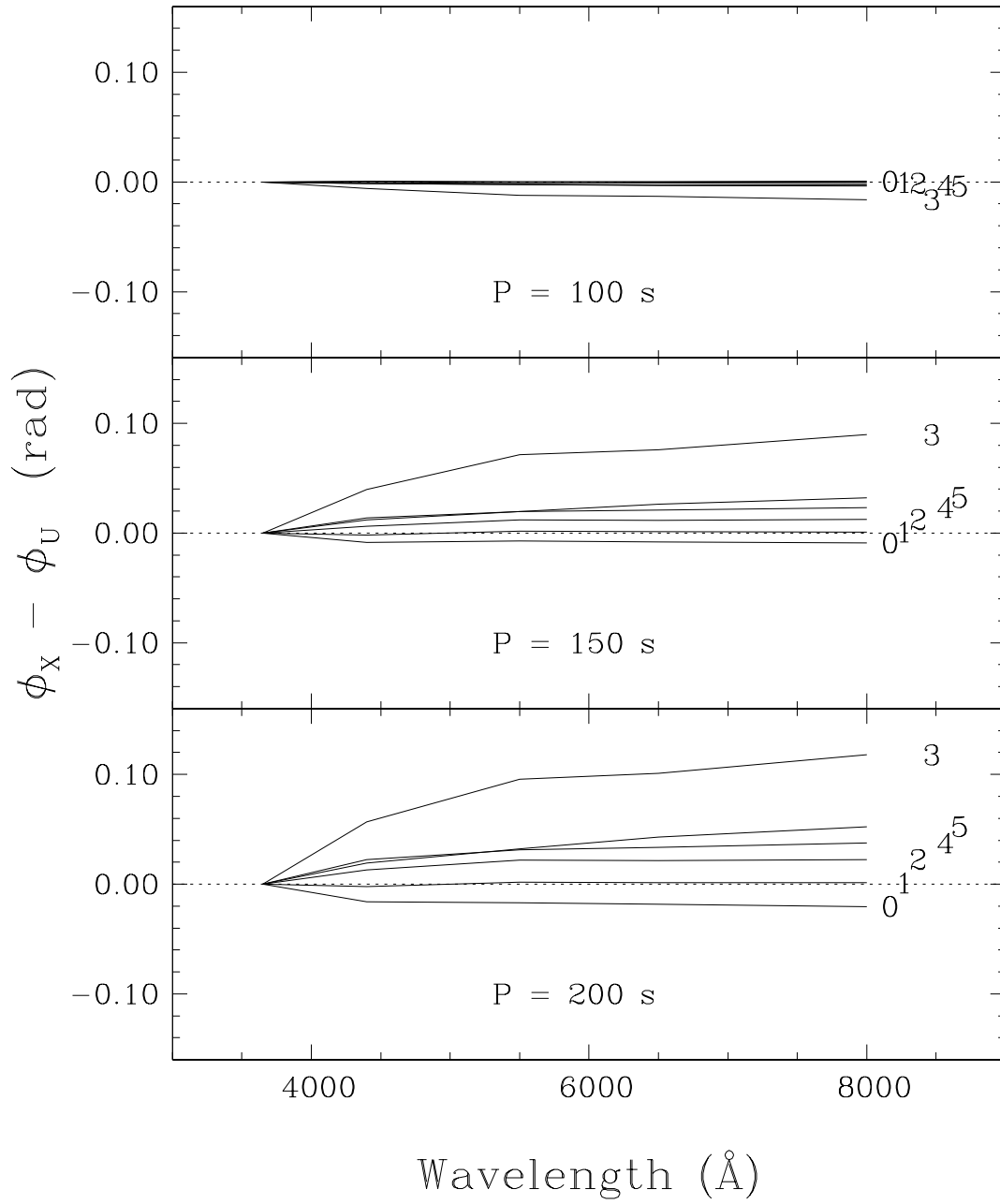


Figure 13

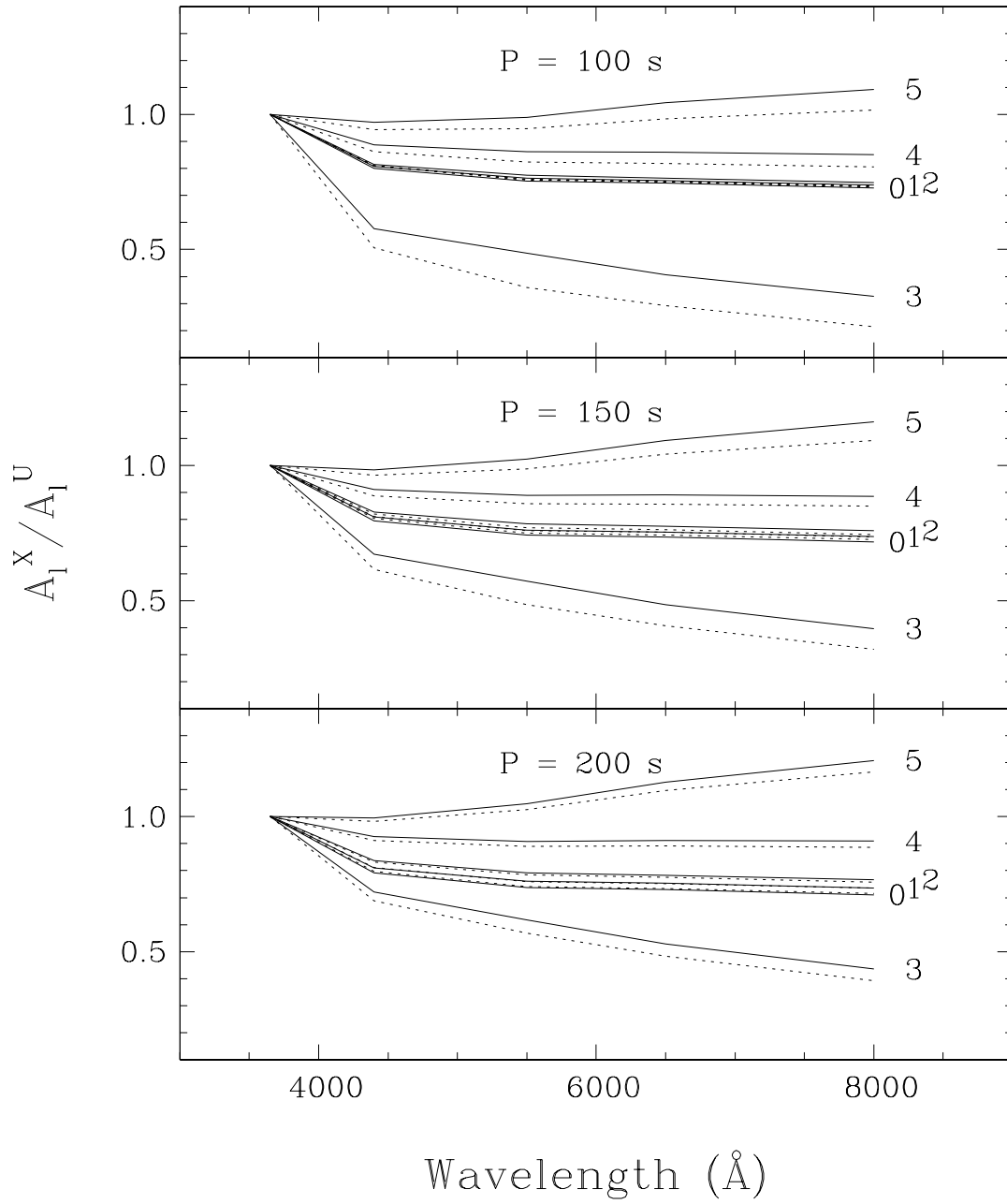


Figure 14

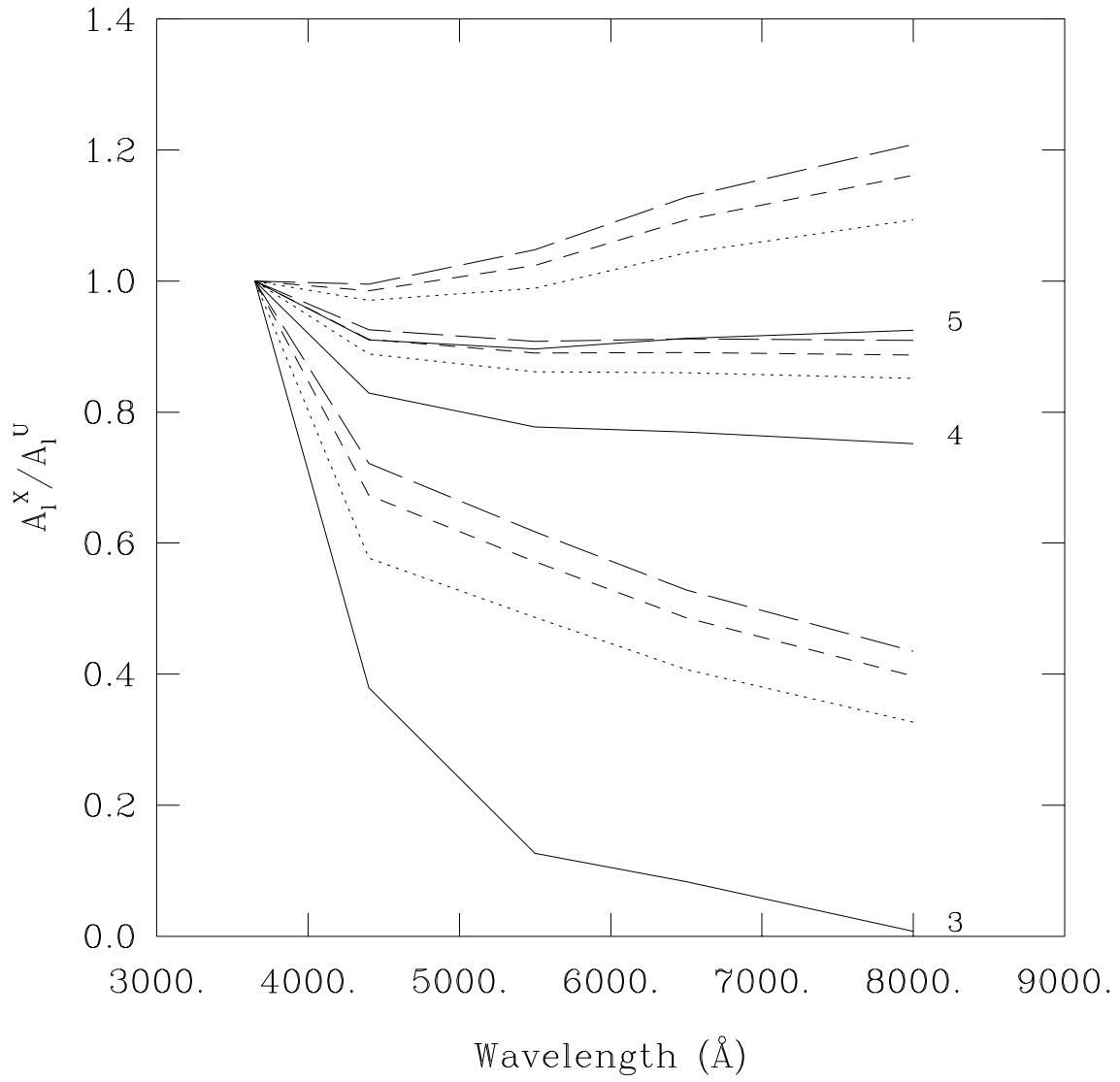


Figure 15a

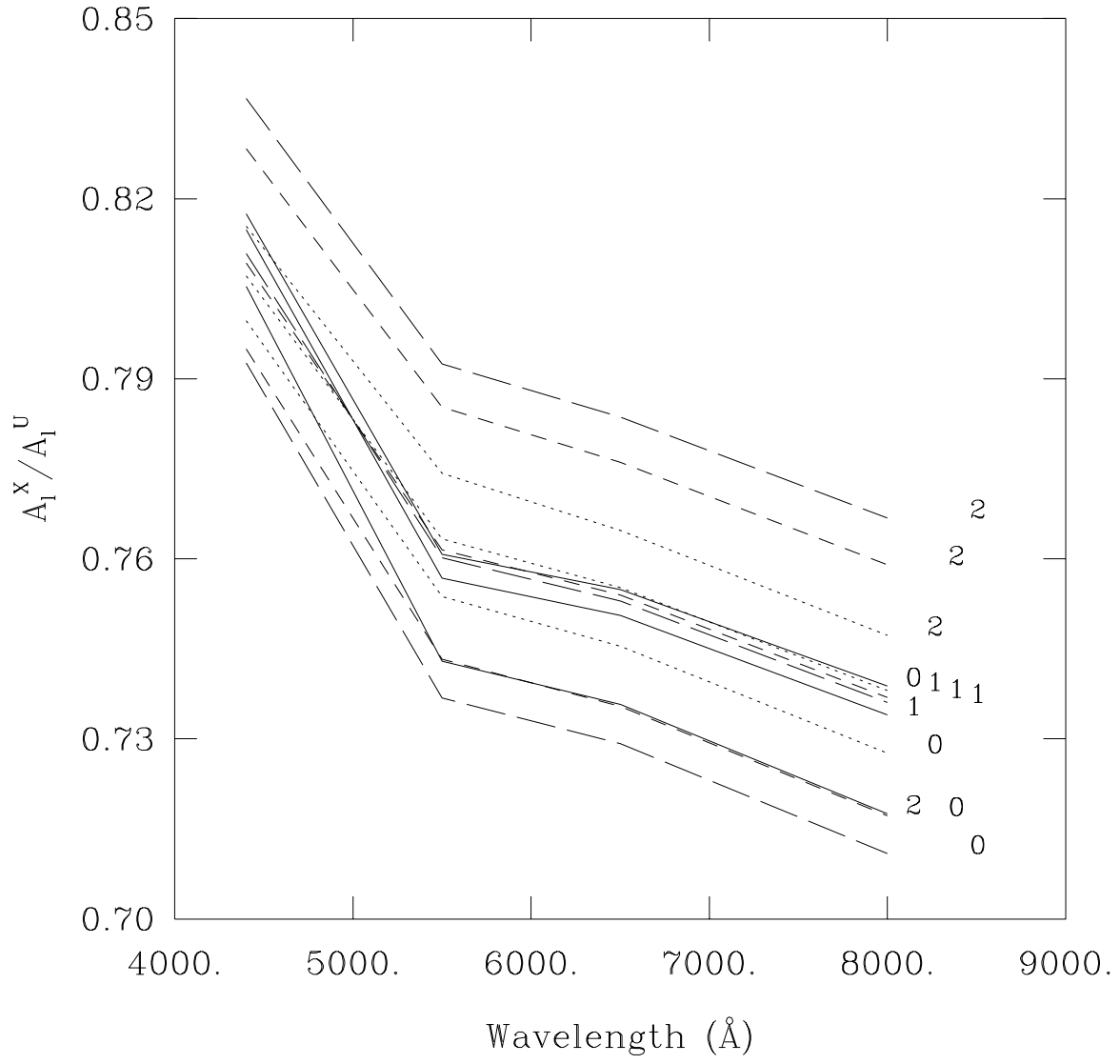


Figure 15b

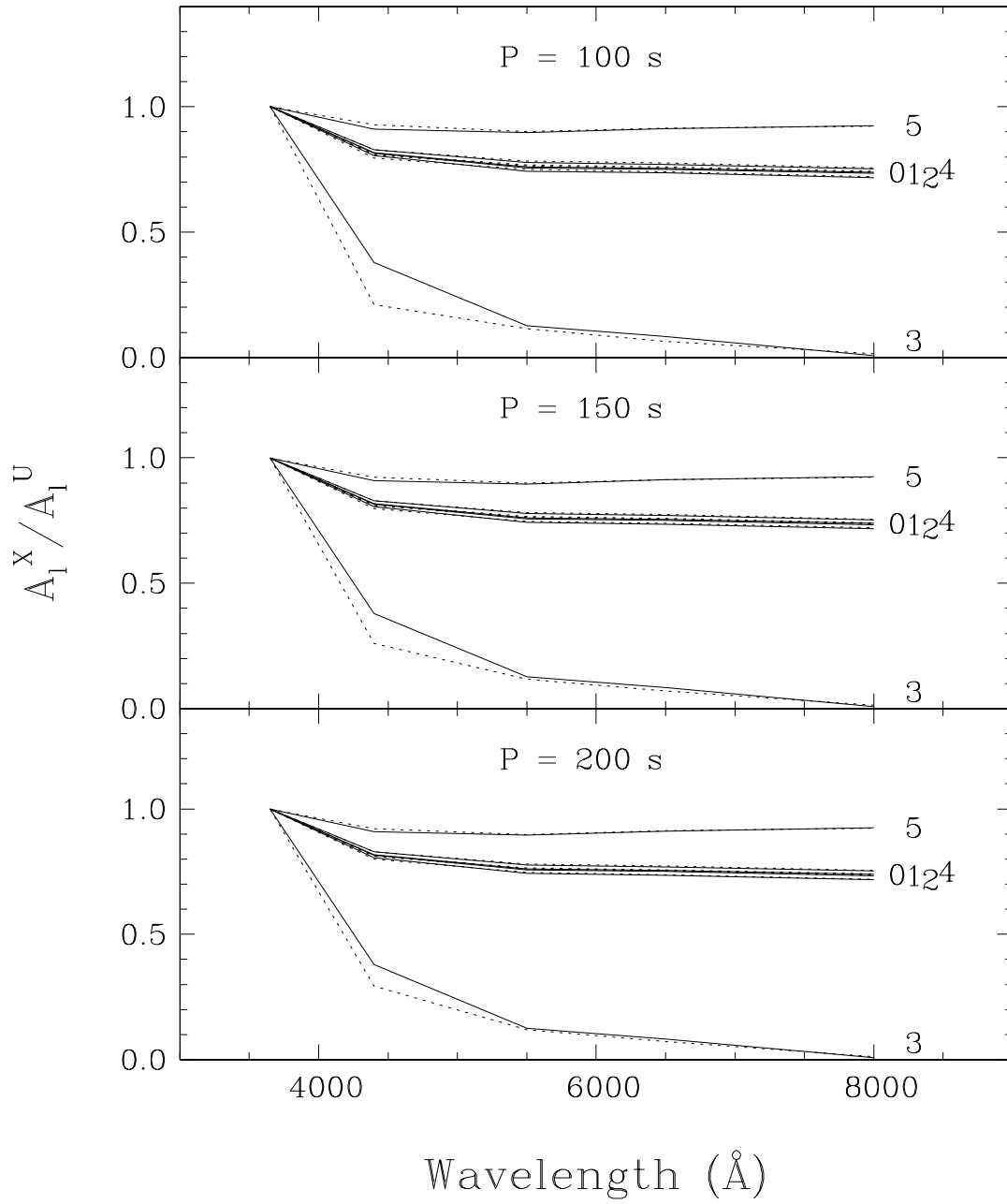


Figure 16

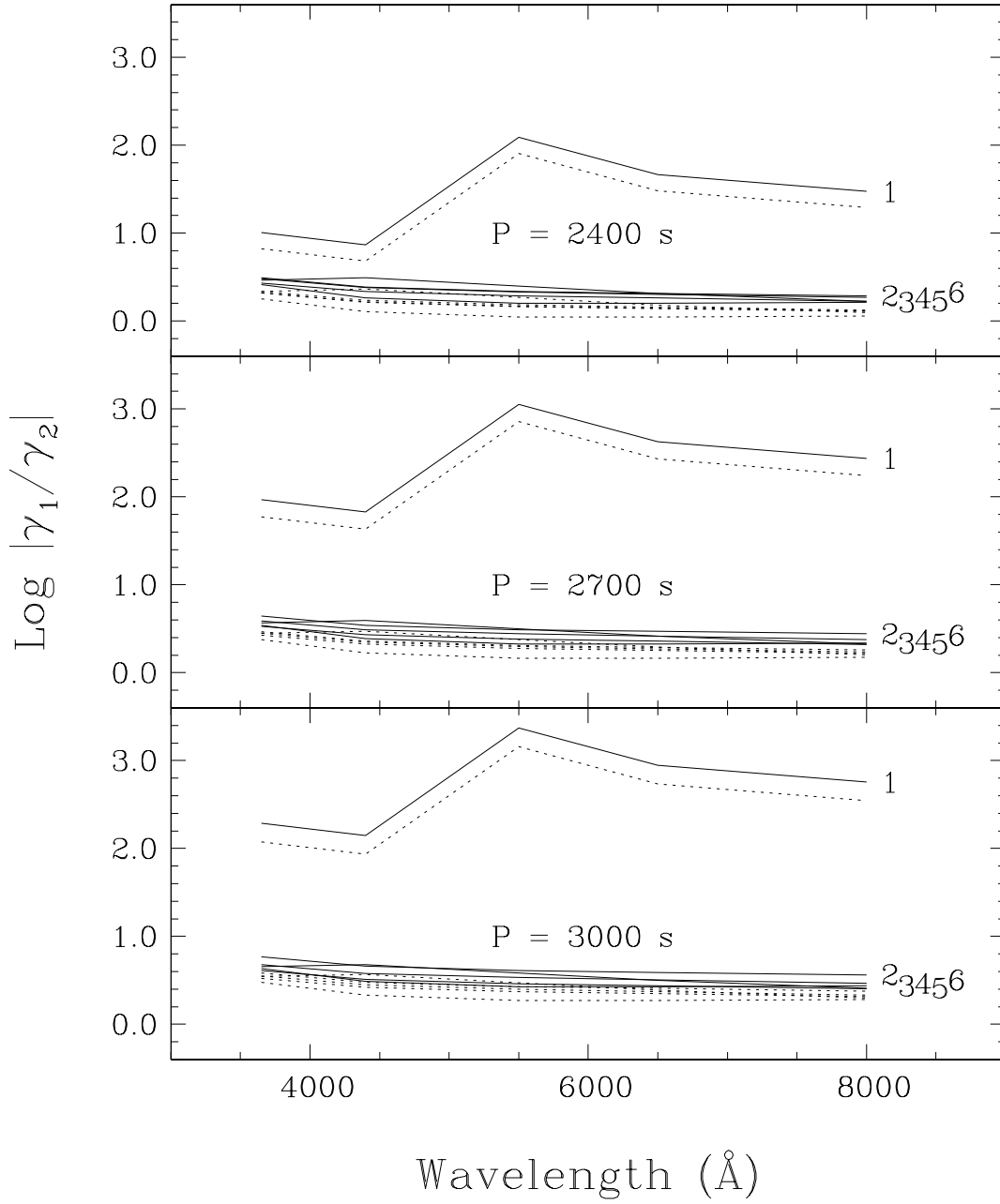


Figure 17a



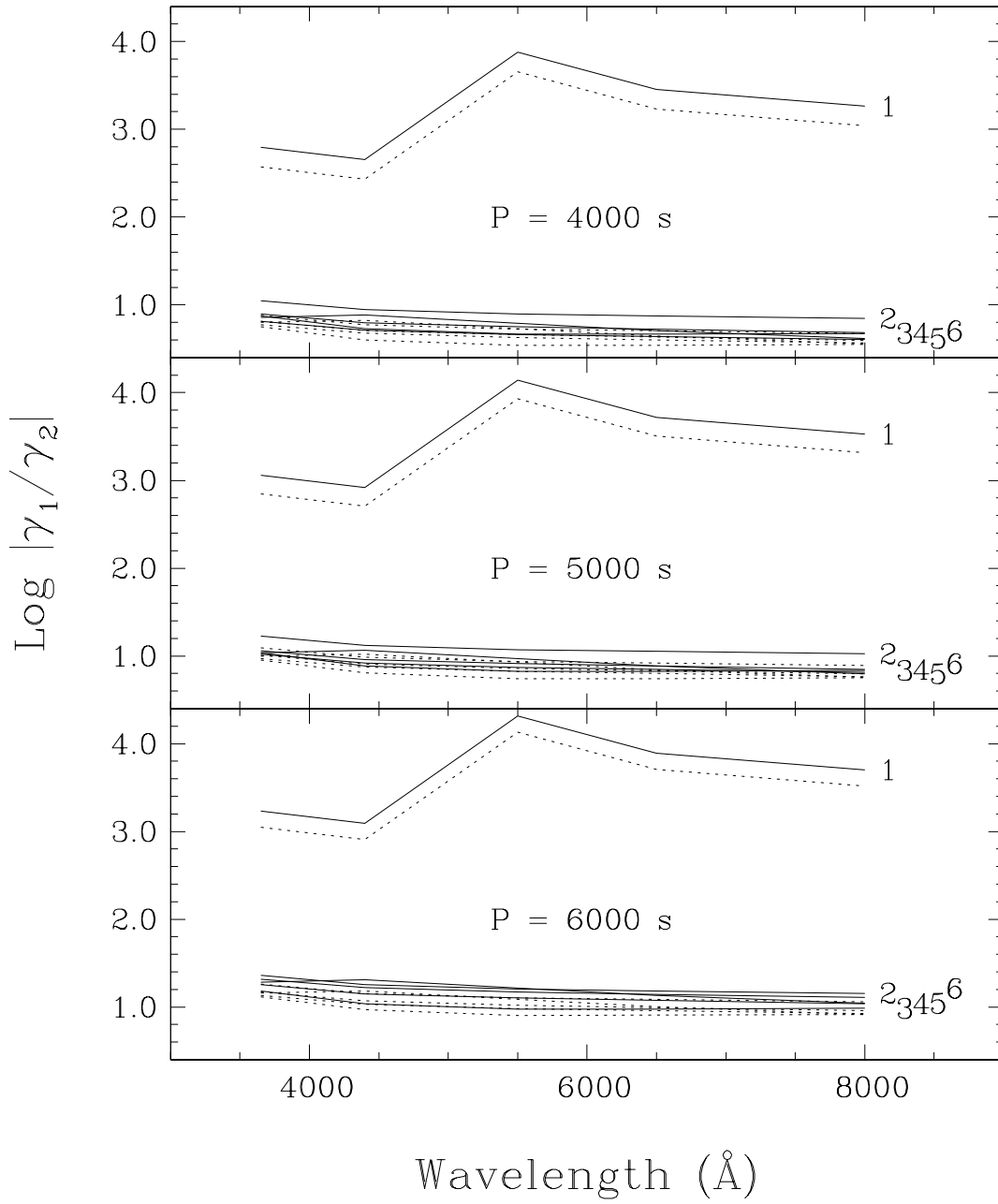


Figure 17b

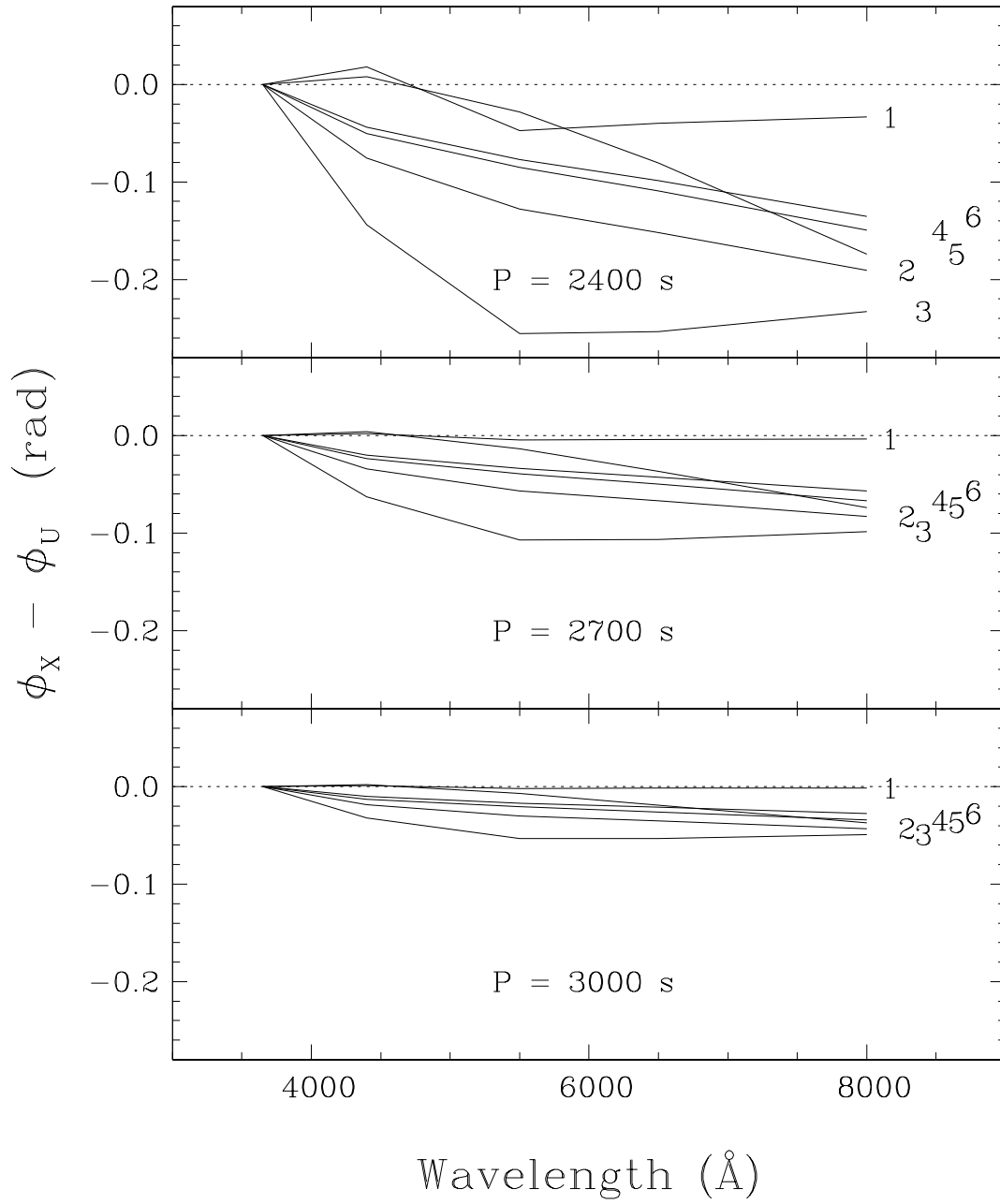


Figure 18a

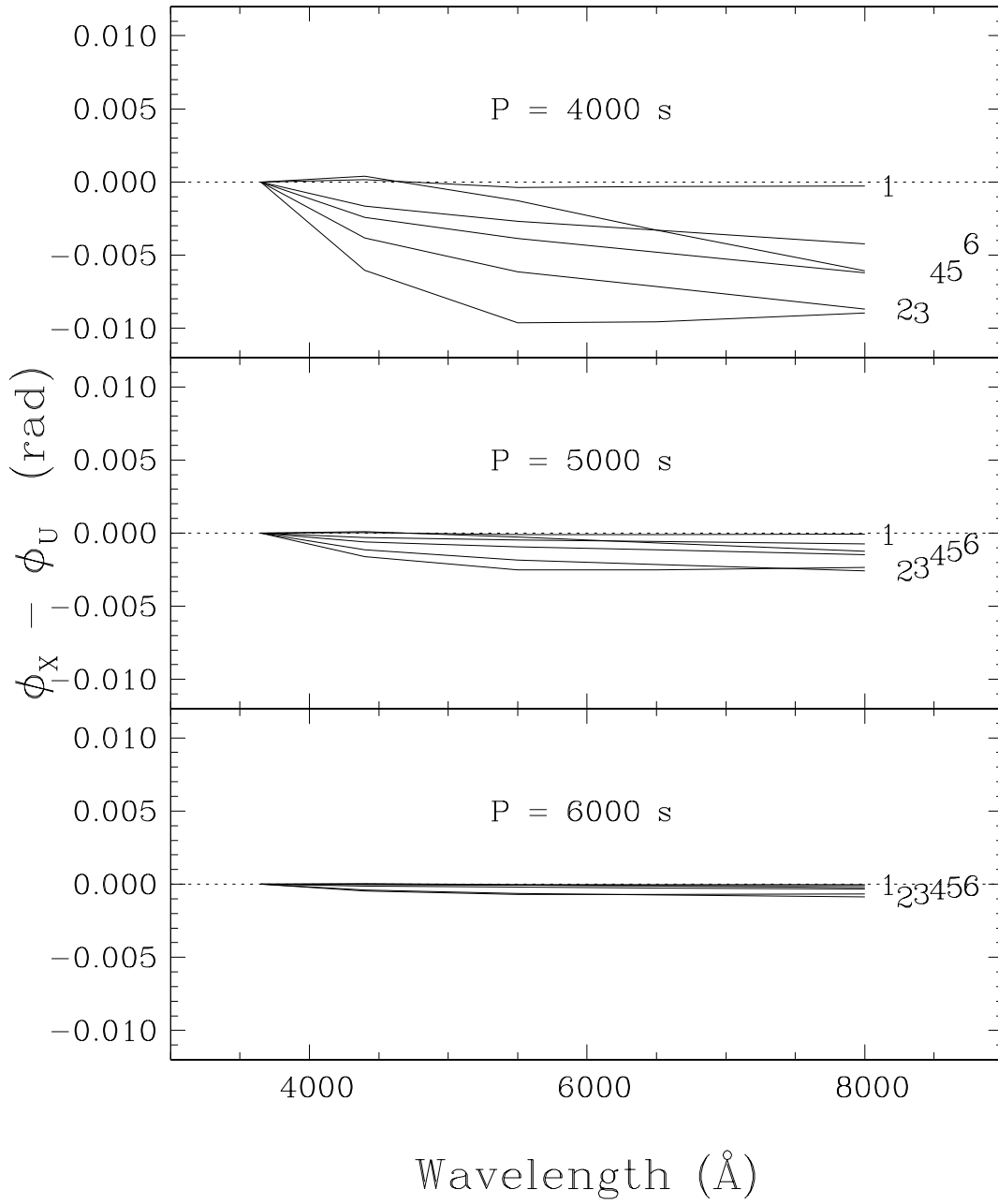


Figure 18b

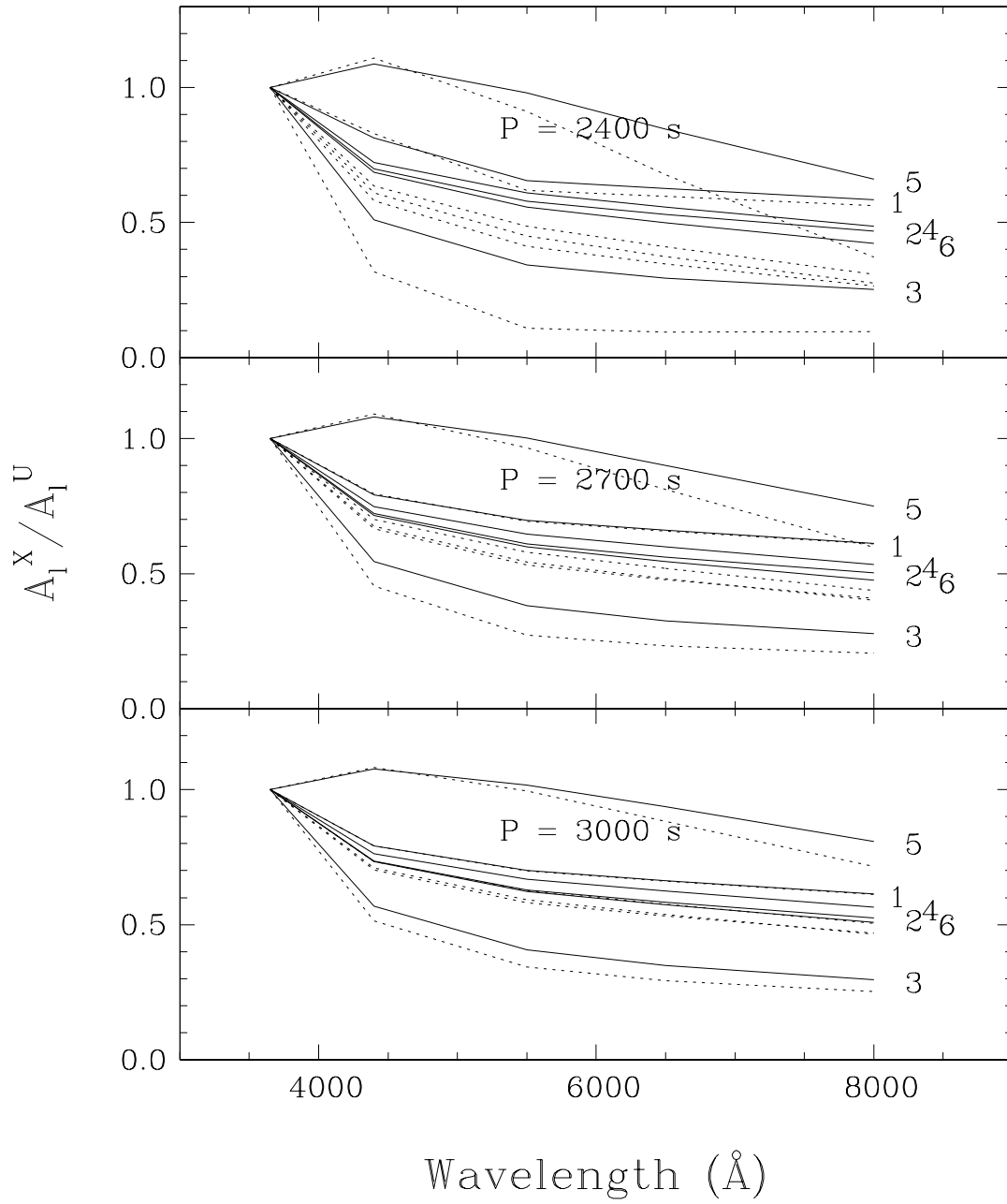


Figure 19a

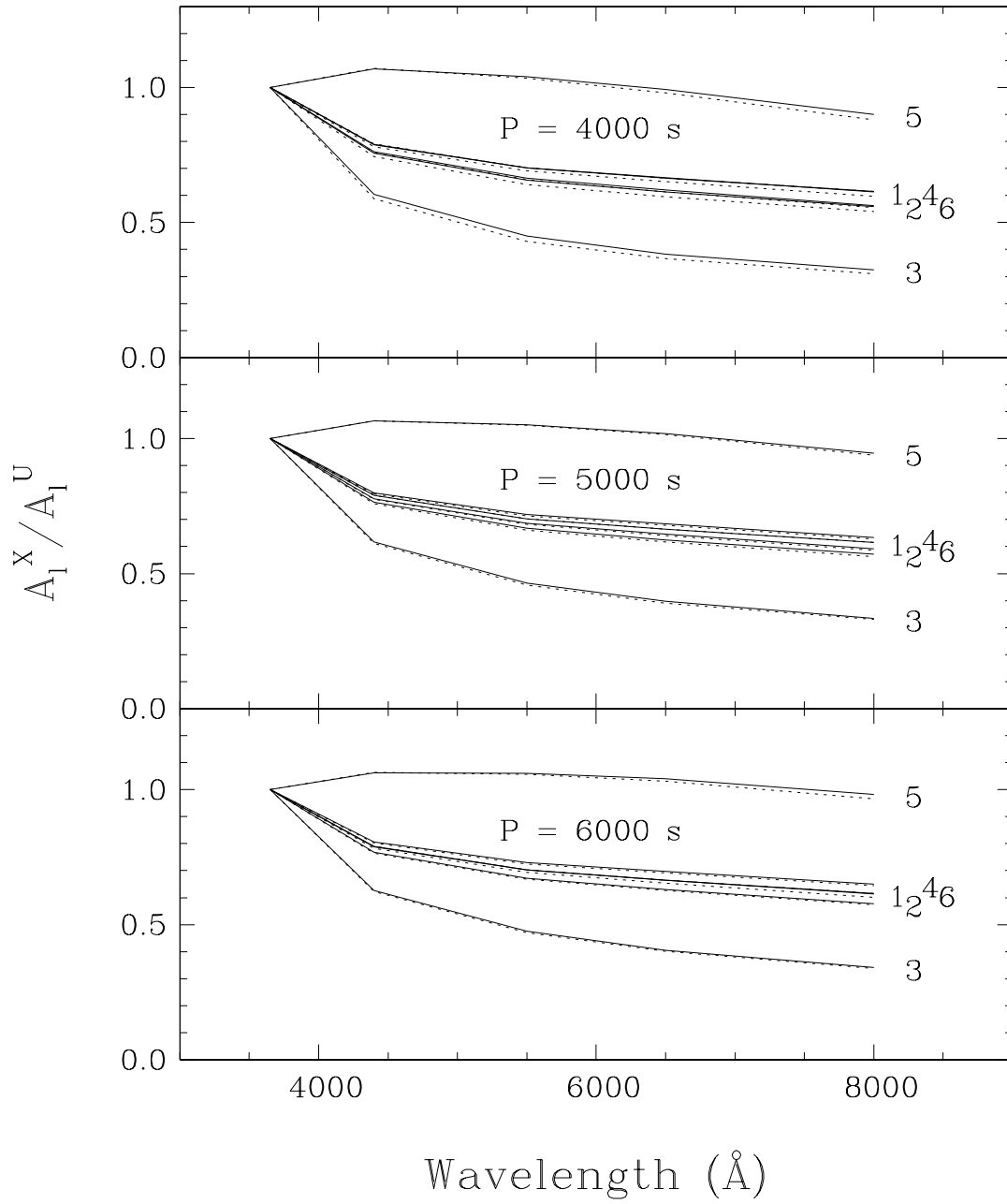


Figure 19b

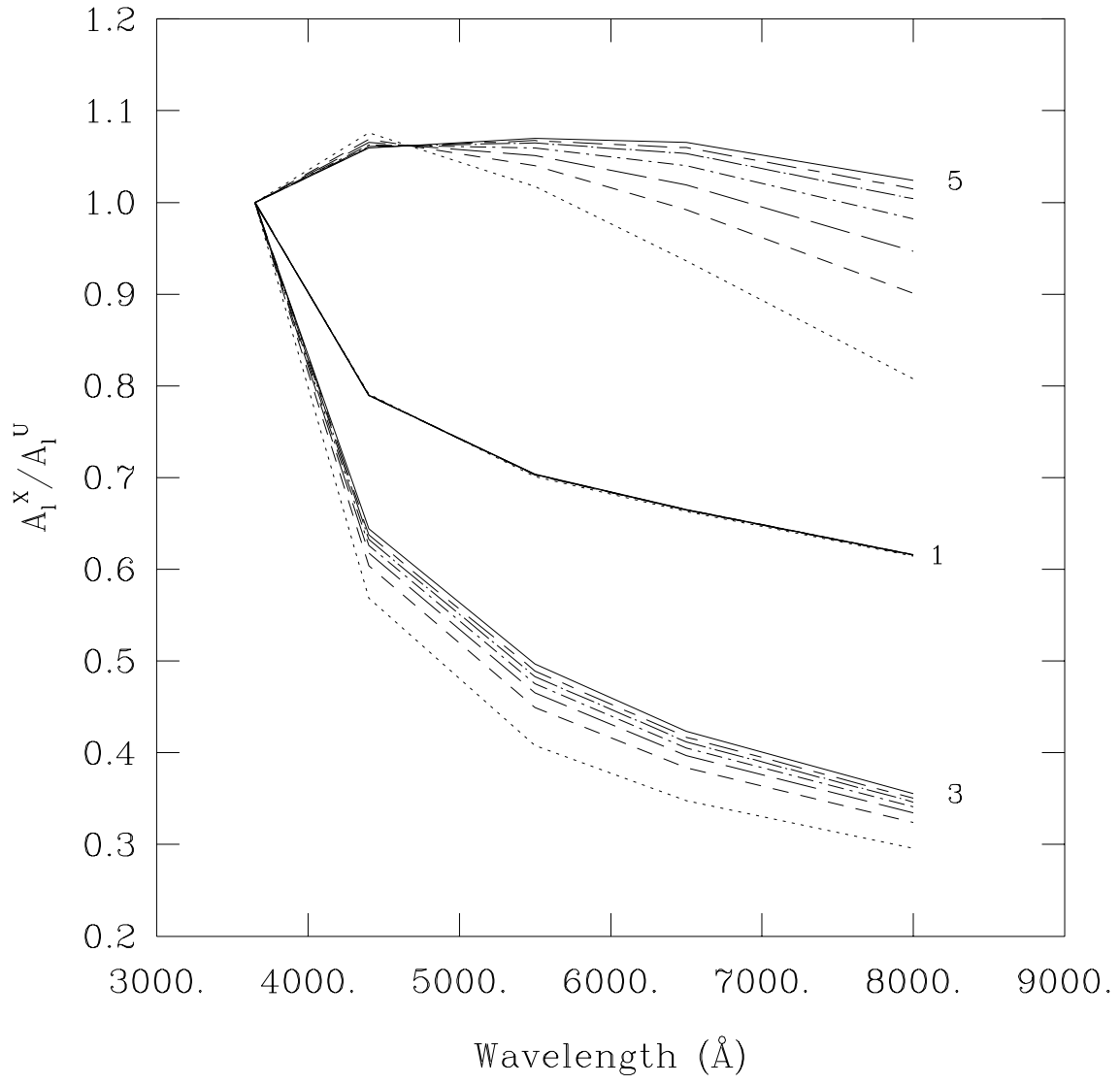


Figure 20a

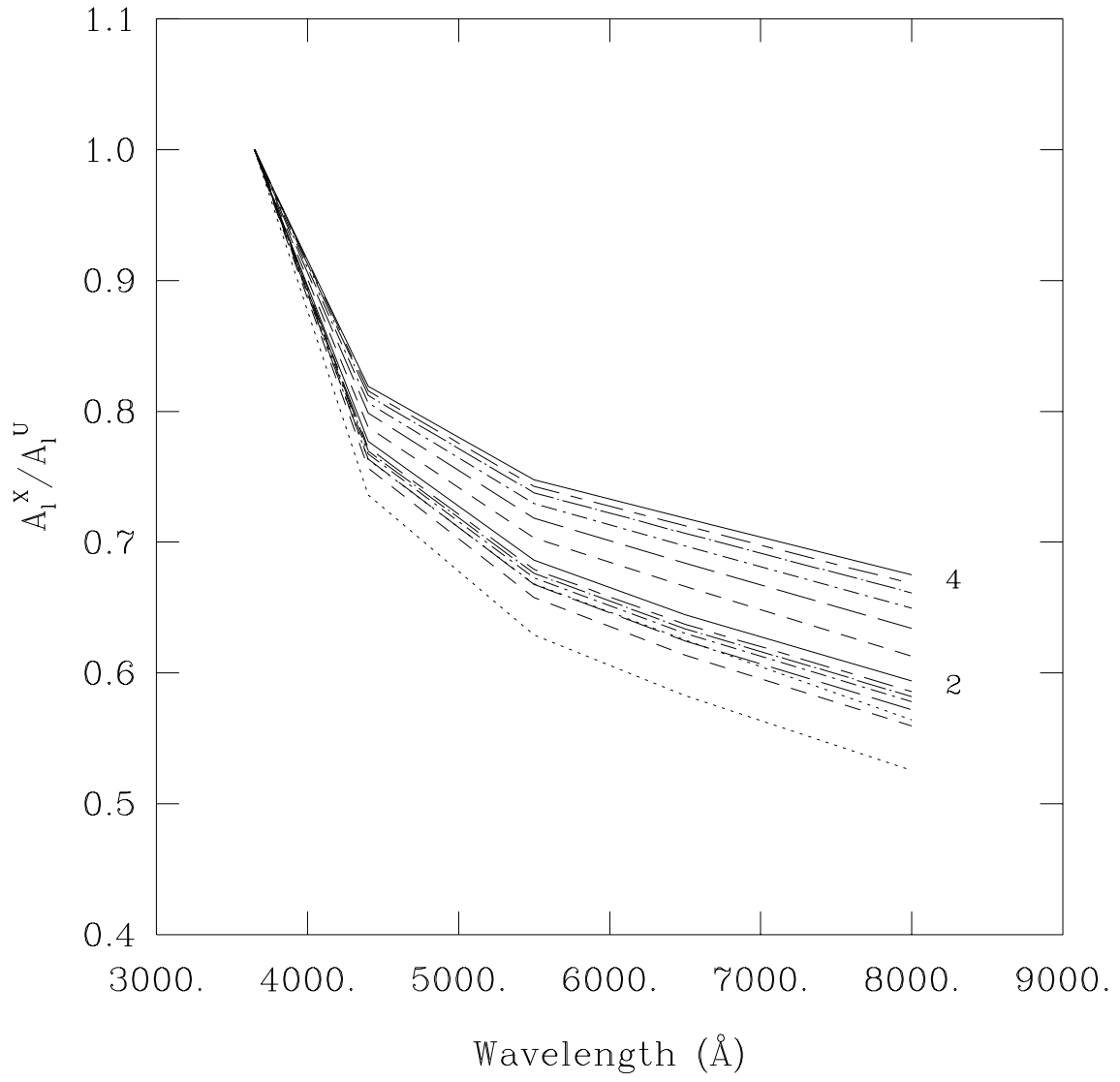


Figure 20b

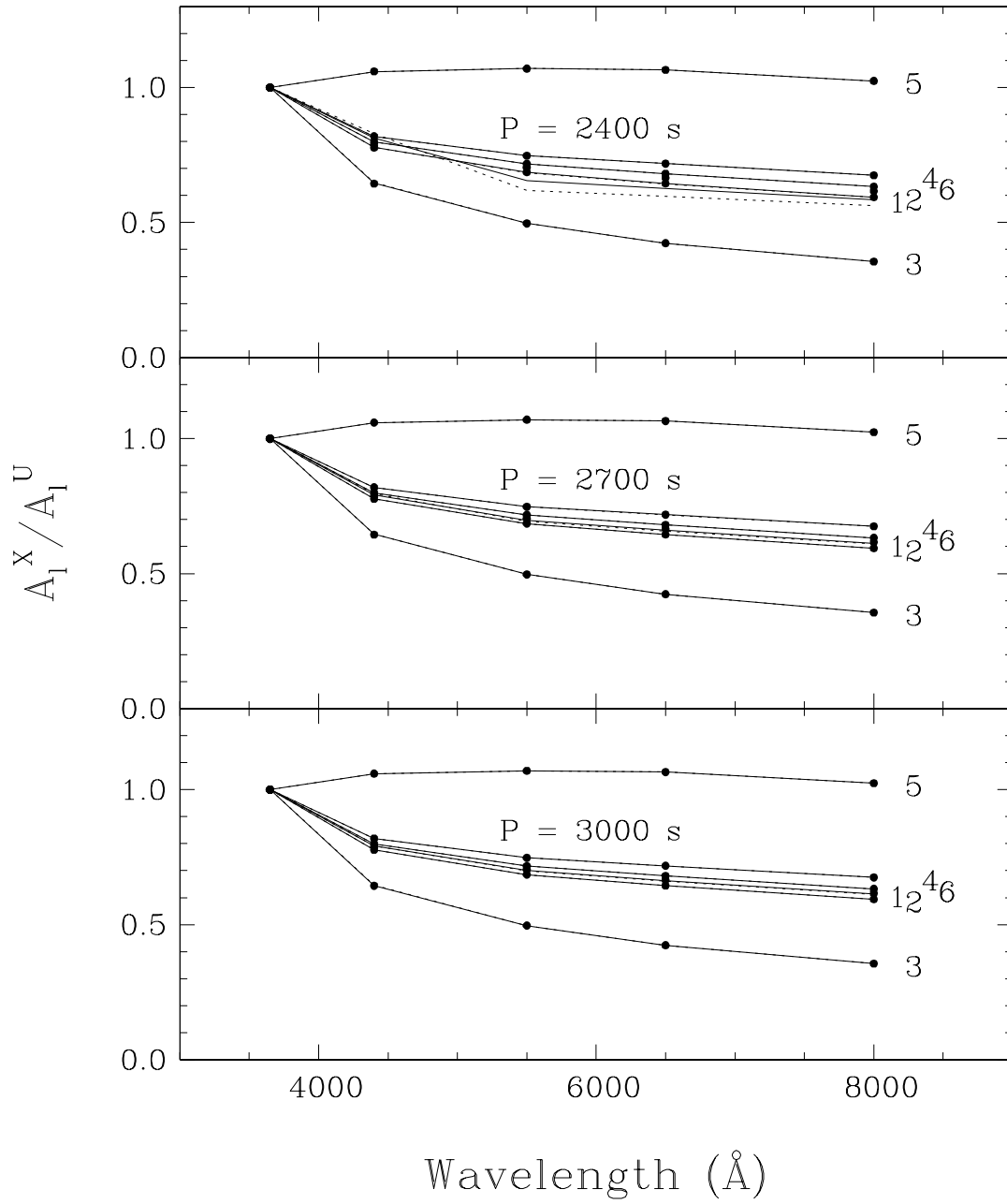


Figure 21



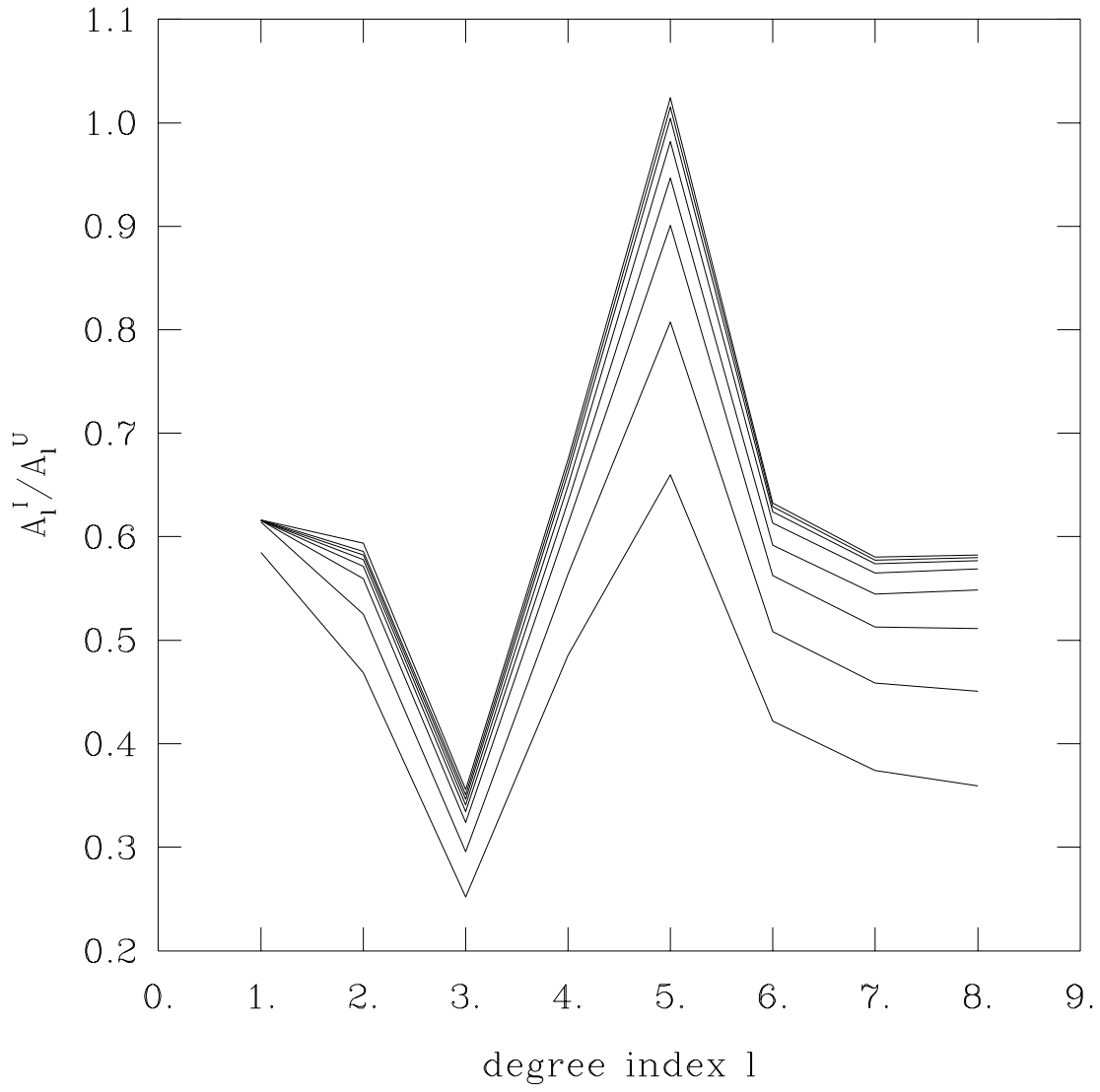


Figure 22

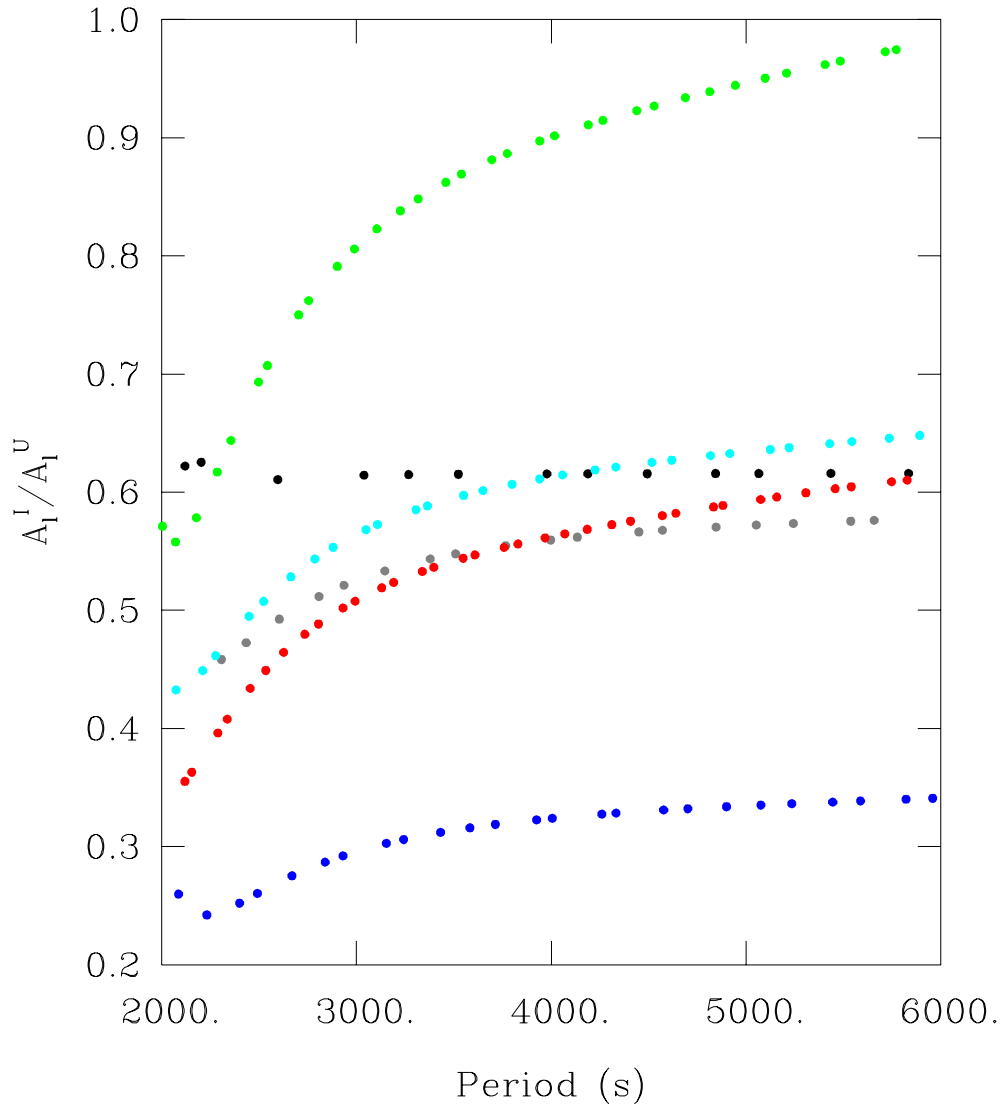


Figure 23

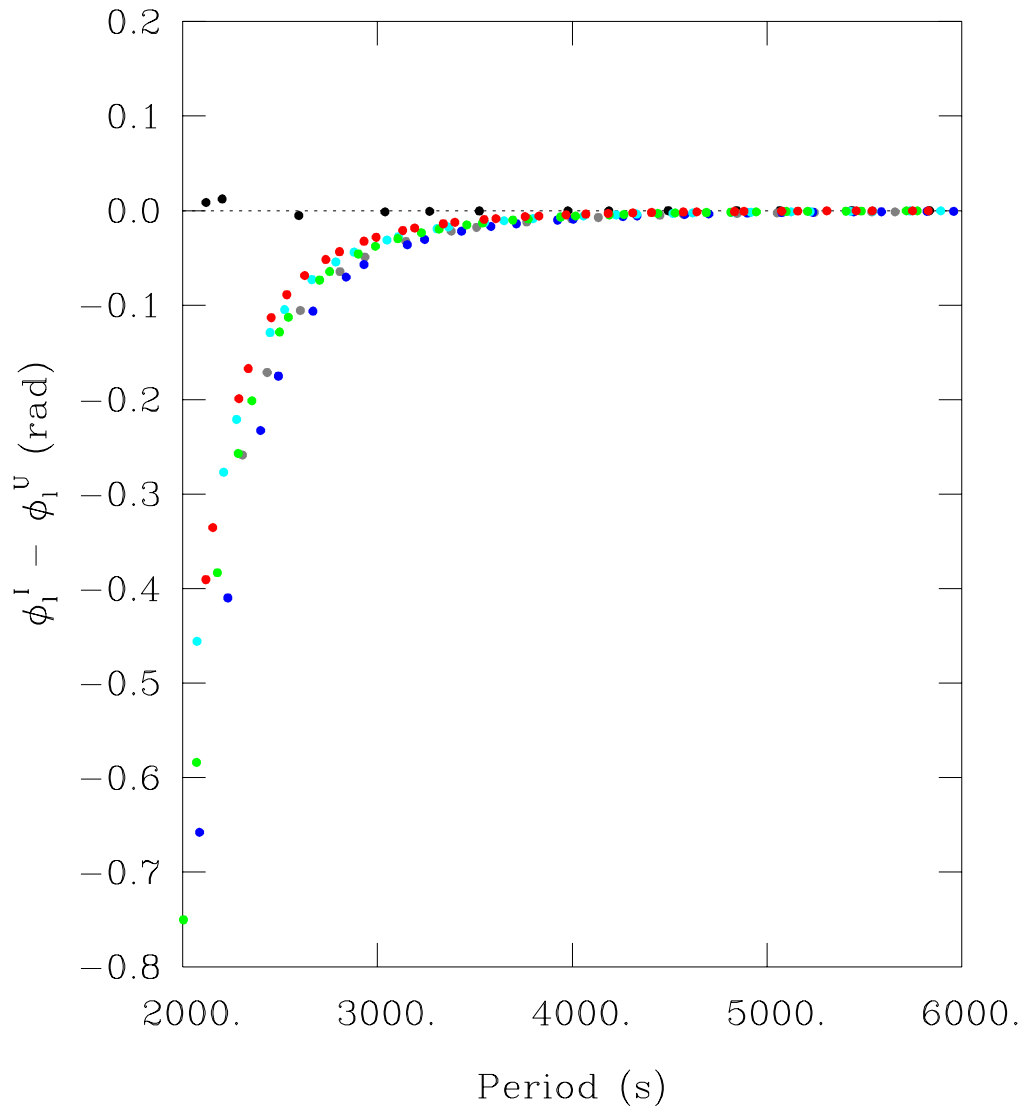


Figure 24

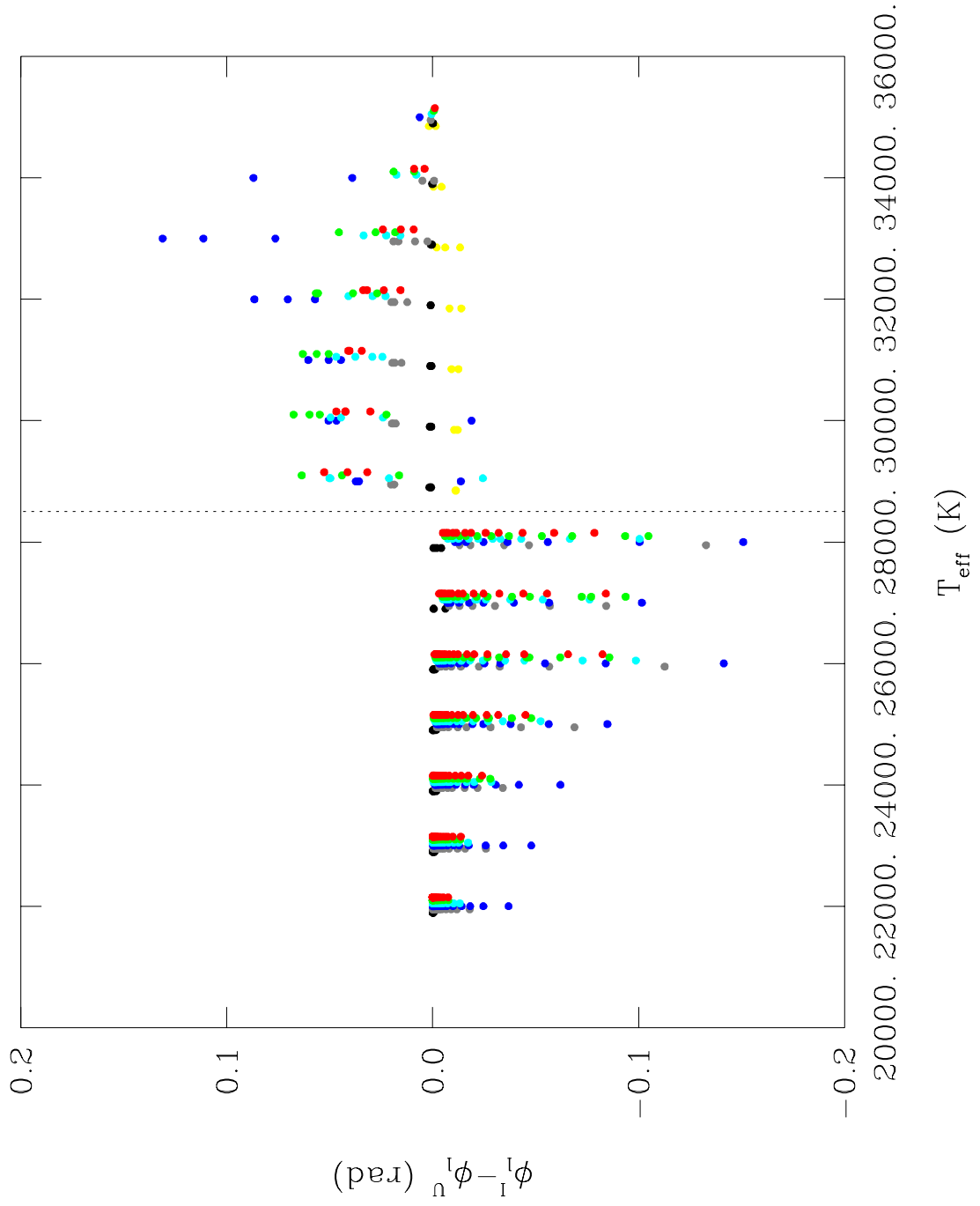


Figure 25

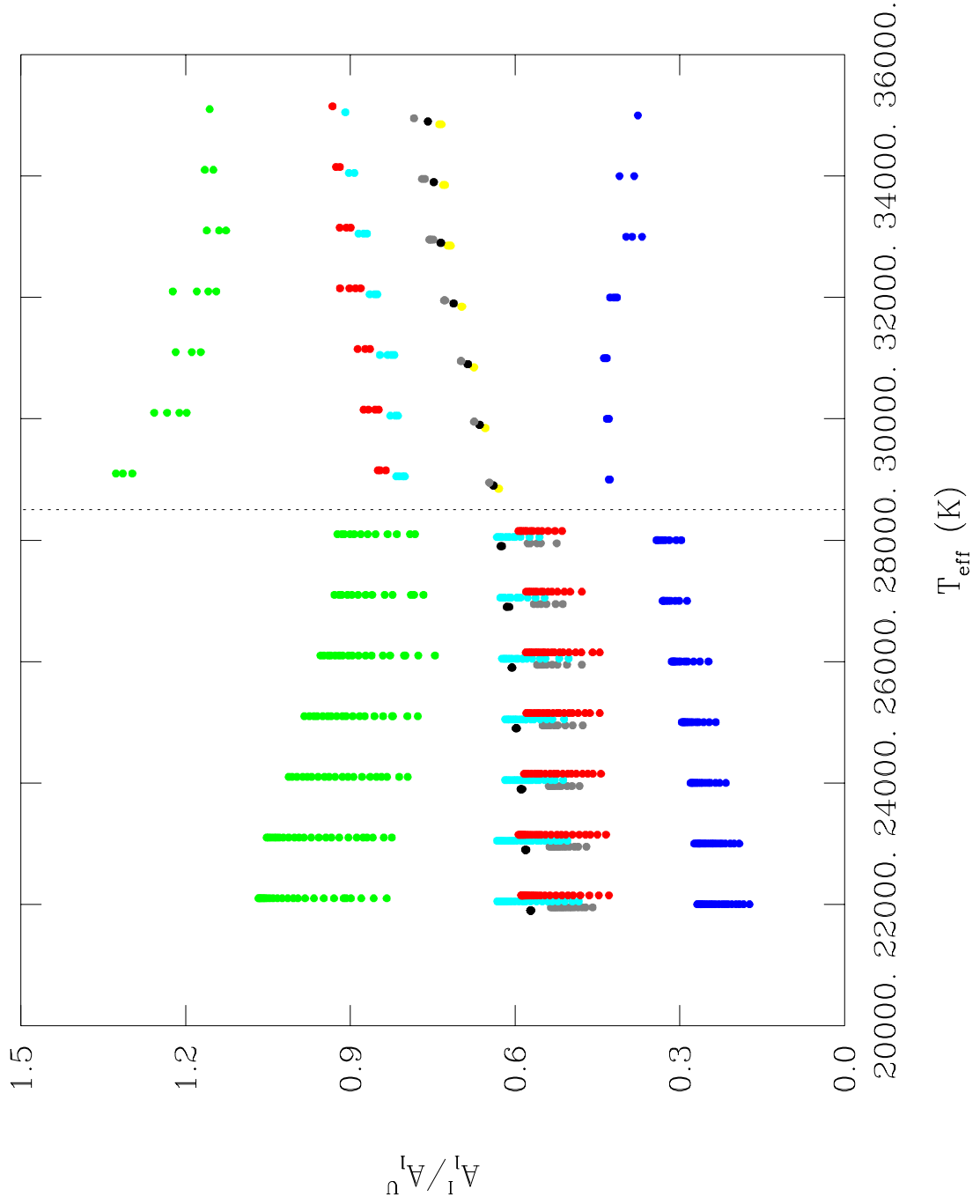


Figure 26

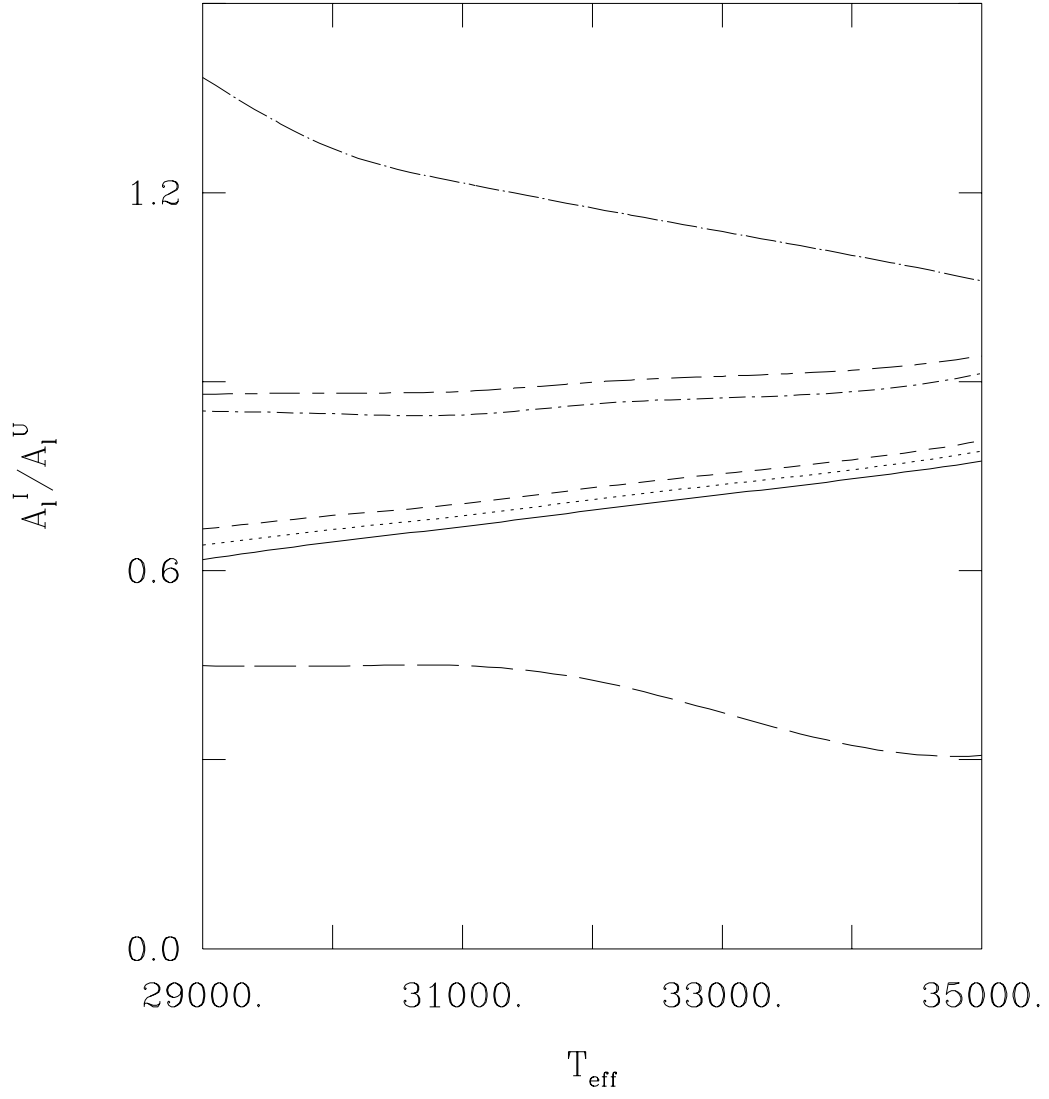


Figure 27a

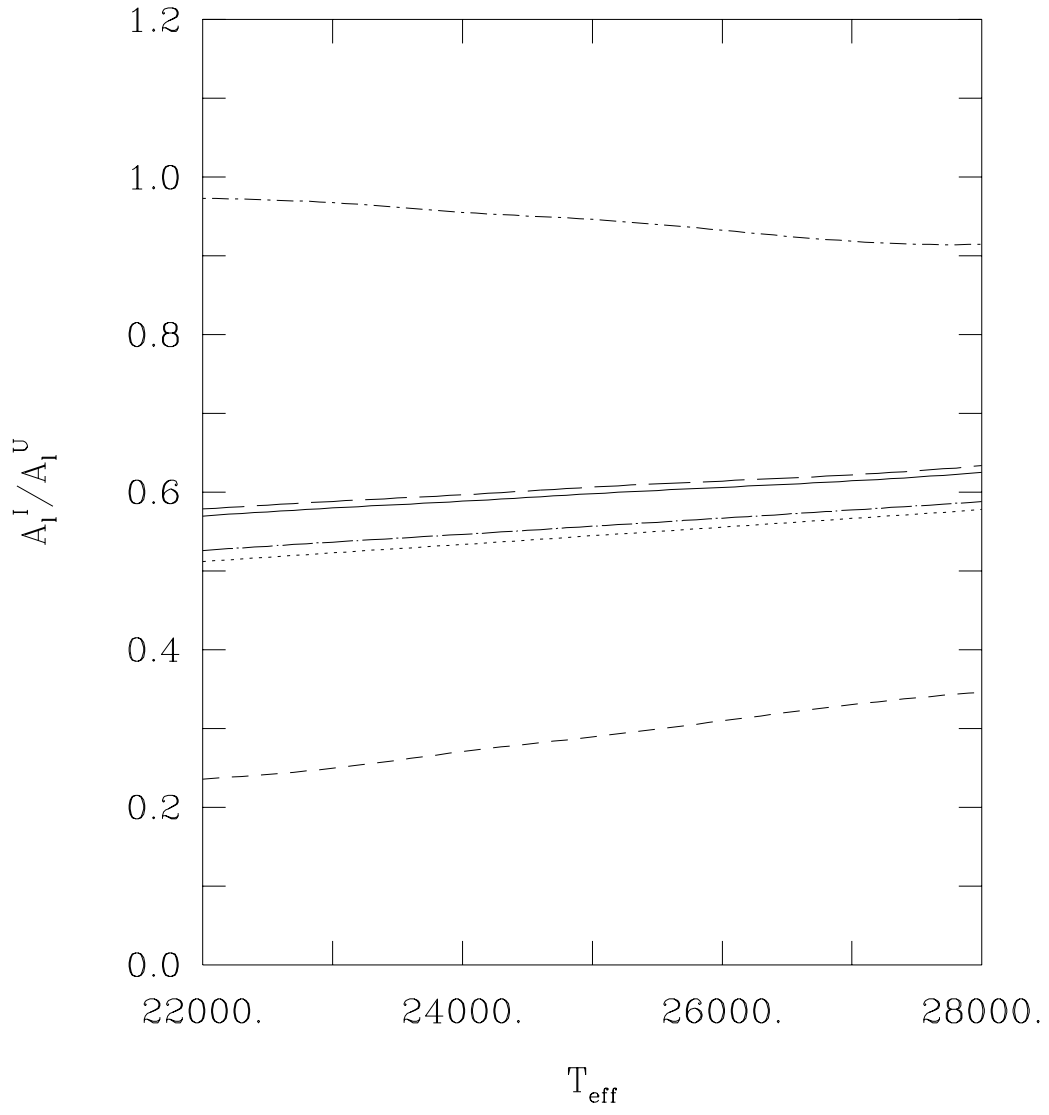


Figure 27b

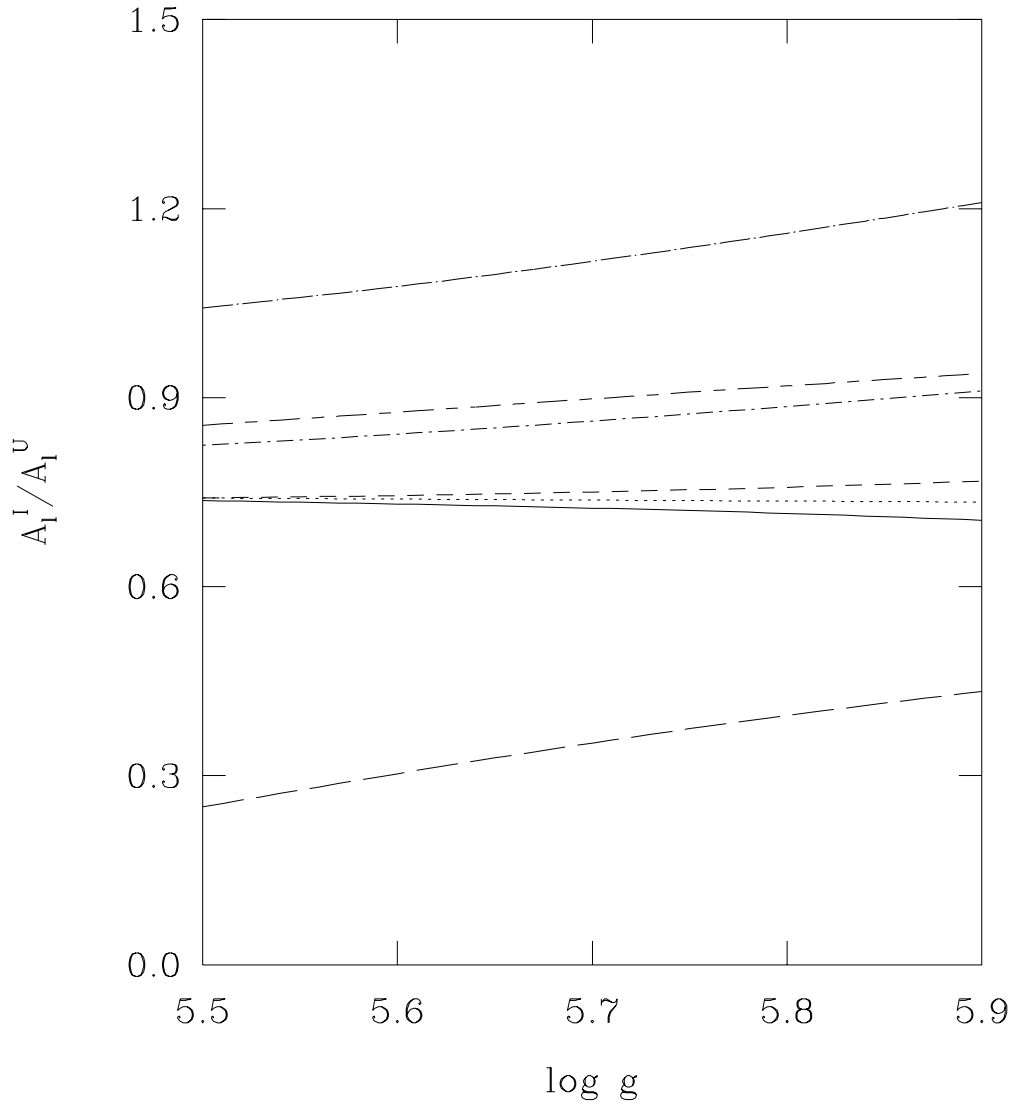


Figure 28a



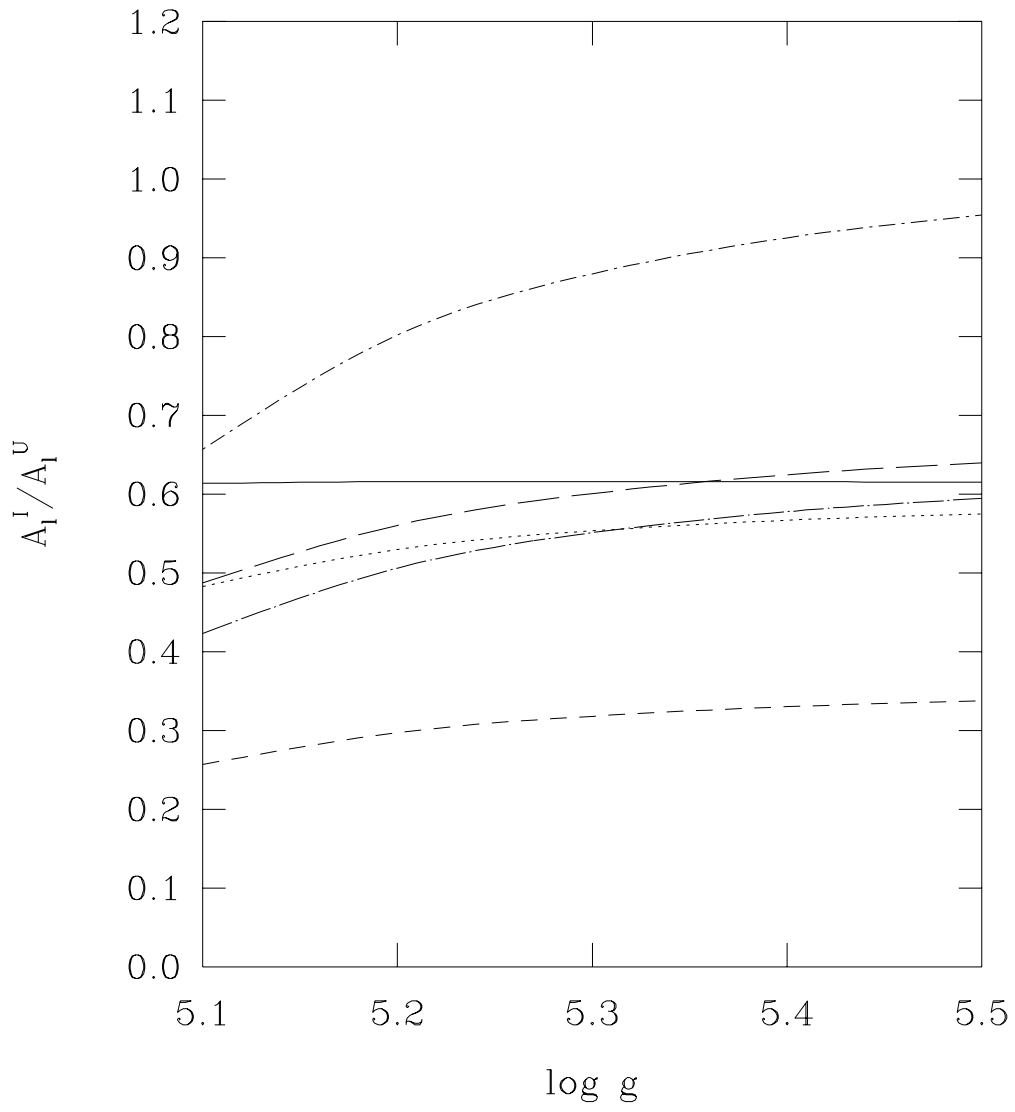


Figure 28b

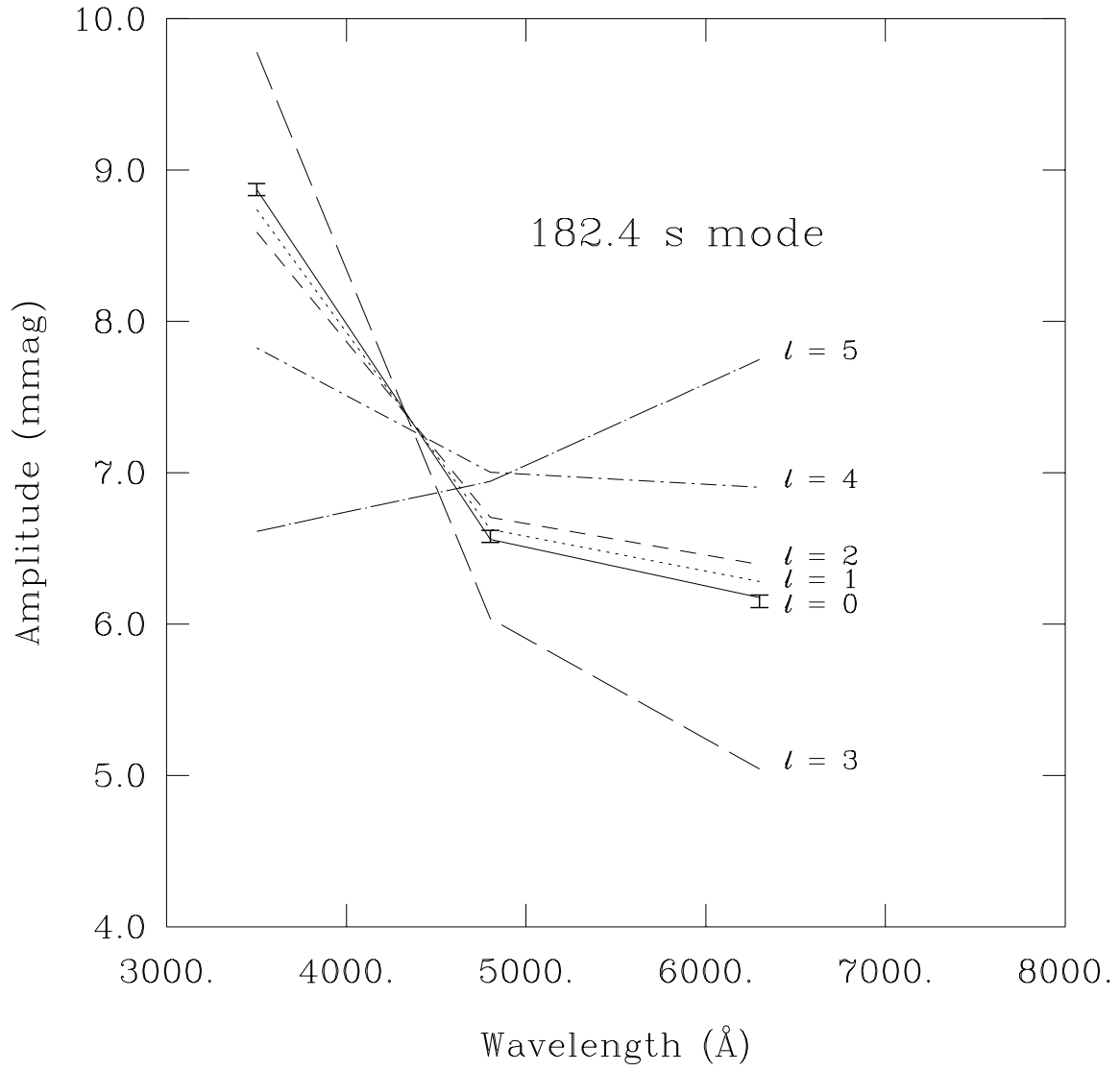


Figure 29